Enabling Increased Variable Renewable Energy Penetration via Thermal Energy Storage Coupled with Nuclear Power Plants

A Dissertation

SUBMITTED TO THE FACULTY OF
UNIVERSITY OF MINNESOTA
BY

Fletcher Carlson

IN PARTIAL FULFILLMENT OF THE REQUIREMENTS
FOR THE DEGREE OF DOCTOR OF PHILOSOPHY

Dr. Jane H. Davidson, Advisor

April, 2021

Copyright Page

Acknowledgements

I am grateful for funding from the Institute on the Environment and the Doctoral Dissertation Fellowship from the University of Minnesota, which allowed me to investigate the use of thermal energy storage with nuclear power plants.

I owe a great deal of thanks to my advisor, Prof. Jane Davidson, for her academic guidance, support and relentless quest for perfection. I am also grateful to my colleagues within the Solar Energy Laboratory. To Jesse Fosheim, Nate Lewin, Sam Kopping and Hyewon Lee: having spent the last year of this work at home I truly appreciated all of our discussions in the office, work related or otherwise.

Finally, I would like to acknowledge my friends and family for all of the encouragement and support that they provided throughout this process. To my parents who have always encouraged me to strive for higher education. And to my friends who provided a much-needed balance to my life. And finally, to my wife who provided the best support anyone could ask for.

Dedication

To my wife, Paola, who deserves as much credit for this work as I do. You encourage me and keep me grounded when I need it. This work is as much a testament to your support and hard work as much as it is mine.

A mi esposa, Paola, quien merece tanto crédito por este trabajo como yo. Me animas y me ayudas a tener los pies sobre la tierra cuando lo necesito. Este trabajo es tanto un testimonio de su apoyo y trabajo duro como el mío.

Abstract

Thermal energy storage (TES) used with baseload nuclear power plants to provide low-carbon flexible electricity and to support the expansion of variable renewable energy sources is analyzed. A thermodynamic model quantifies the impact of options for integration of TES into the Rankine power cycle on cycle behavior and capacity factor. The diurnal energy production ratio, equivalent to a relative capacity factor, is compared in a parametric study of operating conditions, including discharge power (up to 2 times the baseload power, charge duration (2-10 hours), discharge power, discharge duration and the round-trip efficiency of the TES (0.7 to 1), for three configurations. Configuration I charges the TES using high-pressure steam and discharges steam to the low-pressure turbine. Configuration II charges the TES in the same manner and discharges preheated condensate to the steam generator. Configuration III charges the TES using low-pressure steam and discharges the TES to a secondary cycle. Conceptual designs of sensible and latent heat storage devices are discussed with estimates of volume, mass and cost of the storage material.

Configuration III has the highest energy production ratio over the entire parameter range. Use of a secondary cycle eliminates any penalty on baseload operation and reduces the penalty on turbines compared to discharge to the primary cycle. At a discharge power of 1.2 times baseload power, charge and discharge durations of 4 and 3 hours, respectively and a TES round-trip efficiency of 0.9, the energy production ratio is 0.99. Discharge powers up to approximately 1.6 times baseload power are achievable for these parameters. Configuration I can also reach high discharge power but at a lower energy production ratio. Configuration II is restricted to a discharge power of 1.1 times the baseload. The energy production ratio of all configurations decreases with increasing discharge duration and

discharge power and increases with increasing TES round trip efficiency. Increased discharge power can be achieved through an increase in charging duration and TES round-trip efficiency and a decrease in discharge duration. Sensible heat storage is favorable with estimated costs of material from \$5-20 per kWh_e compared to \$20-40 kWh_e for latent heat storage. The narrow temperature range restricts latent heat storage materials to expensive hydroxide-based salts. Configuration II, although limited in discharge power and energy production ratio, requires the lowest thermal capacity, 950 MWh_{th} to provide a discharge power of 1.1 times baseload power with an estimated cost of \$4.87 per kWh_e for a discharge duration of 3 hours, and round-trip efficiency of 0.9. At the same operating parameters, configurations I and III require a storage capacity of approximately 1500 MWh_{th} at cost \$9 and \$21 per kWh_e.

The use of TES can be a transformative technology in the ability to convert baseload nuclear power plants to flexible generation sources for the support of renewable energy. All configuration of TES presented in this work allow for some degree of flexibility. This work demonstrates the importance of how the TES is integrated into the cycle on the energy production of the system, a key indicator of economic viability, the maximum discharge power and the required storage capacity.

Contents

List of Tables

List of Figures

Nomenclature

Latin Symbols		Units
C	Cost	$
c	Specific storage cost	$ kWh^{-1}
c_{om}	Operations and Maintenance Cost	$
c_p	Specific heat	kJ kg^{-1} K^{-1}
c_{mat}	Specific material cost	$ kg^{-1}
$\dot{E}x$	Exergy transfer rate	kW
f	Fractional value	-
F	Mass Fraction	
h	Specific enthalpy	kJ kg^{-1}
h_{fus}	Latent heat of fusion	kJ kg^{-1}
L	Non-dimensional TES length	-
l	Total TES length	m
$\dot{m}$	Mass flow rate	kg s^{-1}
m	Mass	kg
n	Year Number	year
N	Length of Operation	years
P	Pressure	Bar
Q	Thermal energy	kJ
$\dot{Q}$	Thermal power	kW_{th}
r	Revenue	$
R	Residual mass flow rate	kg s^{-1}
s	Specific entropy	
T	Temperature	°C and K
ΔT	Change in temperature	°C and K
t	Time/duration	hour
u	Specific energy density	kJ kg^{-1}
V	Volume	m^{-3}
W	Mechanical energy	kJ_e
$\dot{W}$	Mechanical power	kW_e
x	Molar fraction	-
y	TES position	m

Greek Symbols		
ε	Exergetic Efficiency	
η	Efficiency	
π	Electricity Price	$ MWh_e^{-1}
ρ	Density	kg m^{-3}
Φ	Void fraction	
χ	Steam quality	

Subscripts	
ABC	Multistage TES module
A, B, C	TES stage identifiers
1-26	Refers to state-point

BL	Baseload operation
C	Charge operation
D	Discharge operation
des	Destruction
DP	Design point of turbine
i	Mixture component index
I, II, III	TES configuration
in	Inlet
ise	Isentropic
j	Iteration index
k	TES stage index
m	Melt temperature
n	Turbine section index
net	Net
OD	Off-design
out	Outlet
RT	Refers to round trip efficiency
s	Sensible heat
ss	Single stage
S1-S7	Turbine sections
SCT	Secondary cycle turbine
SG	Steam generator
T	Turbine
X	Without TES integration

Abbreviations

DPR	Discharge power ratio
EPR	Energy production ratio
FWP	Feedwater pump
HPT	High-pressure turbine
IRR	Internal rate of return
LPT	Low-pressure turbine
SP	State-point
TES	Thermal energy storage
VRE	Variable renewable energy

1 Introduction

Capacity additions of variable renewable energy (VRE), such as wind and solar, have outpaced the addition of more traditional thermal energy sources such as coal, natural gas and nuclear since 2010 in the U.S. [1]. This trend shows no sign of abatement with a 1000% growth in VRE expected over the next 30 years [1]. The intermittent nature of VRE supply over both diurnal and seasonal time scales creates challenges to balance supply with fluctuating consumer demand. At modest levels of VRE generation, the temporal variation between supply and demand can be accommodated through simple or combined cycle natural gas fired power plants. At larger levels of VRE, natural gas power plants cannot provide the needed flexibility and there is risk of under or overgeneration. This problem is most commonly referred to as the 'Duck Curve' [2]. For example, high VRE output during midday hours driven by solar power poses the risk of over generation. One solution is to curtail VRE generation, but curtailment reduces the capacity factor and increases the cost of electricity from VRE. At 80% VRE penetration, curtailment could exceed 120 TWh per year [3]. Energy storage and increased flexibility of baseload power plants are seen as key solutions to maximizing VRE use on the power grid [4]. The present work considers the use of thermal energy storage with nuclear power plants as a means to provide this flexibility and help decarbonize energy production [5]–[8].

To support the advancement of VRE generation in the U.S. to 50% penetration, it is projected that 140 GW_e of energy storage will be needed [9]. A host of energy storage devices are available to provide a wide range of energy services from instantaneous grid stabilization to long term, diurnal and seasonal load shifting [10]–[13]. It is likely a combination of these technologies will be deployed in the future. Currently, the majority

of utility-scale energy storage deployed in the U.S. is pumped hydro storage (PHS). The implementation of PHS has stalled primarily due to geographical restrictions such as water and elevation limitations [14], low natural gas prices and public policy barriers [15]. Presently, batteries and the associated power electronics are relatively expensive [16]. Thermal energy storage (TES) can potentially provide energy storage at an order of magnitude lower cost than lithium ion batteries [11], [17]–[19]. Coupling TES with a thermal energy source such as nuclear has thermodynamic benefits over converting electricity to thermal energy, which has been suggested [17], [20]

Nuclear power plants is a dispatchable, carbon free thermal energy source [6], [21], [22]. Researchers at MIT [18], [19], [23]–[26] and the National Renewable Energy Laboratory [20] have suggested TES to improve the economics of nuclear power as well as to increase the use of VRE sources. Most existing nuclear power plants are intended for nearly constant power. The allowable rate of increase or decrease of power is approximately 0.5% of the rated capacity per minute [8], down to 50% of rated power [27]. Use of TES with a nuclear power plant would increase the flexibility of the system, limited only by the rate of change of the steam turbine which is about 7% of capacity per minute down to about 30% of rated power [27], [28]. Manufacturers of nuclear reactors plan on implementing thermal energy storage in next generation power plants, with charge and discharge power of the TES from 20-25% of the nominal power [29]–[31]. Next generation nuclear reactors may be cooled by liquid sodium or lead which could facilitate the use of TES [30], [32], [33]. However, implementation of these reactor designs has stalled due opposition to nuclear power by the public [34], [35] and poor economic conditions for new

reactors [36]. Therefore, this work focuses on retrofitting nuclear power plants with pressurized water reactors.

Figure 1 illustrates the operation of a nuclear power plant with TES when operated in a power grid with VRE sources. The power grid is a term used to describe the distribution network between electricity consumers and suppliers. Demand for power is variable, dependent on the time of day, season and geographical location. Supply to the power grid is provided by a variety of resources. During periods in which VRE generation is high, steam in the nuclear power plant can be diverted from the main power cycle and the heat can be stored in a TES system (red line). During periods of low VRE generation, heat stored in the TES can augment power plant generation (green line). These two processes are referred to as charging and discharging the TES. The work presented here quantifies the impact of different approaches to integrate TES in the system on the performance of the power cycle during TES charge, TES discharge and baseload operation. It is crucial to integrate the TES in a manner that maximizes capacity factor while providing the flexibility needed in a power grid.

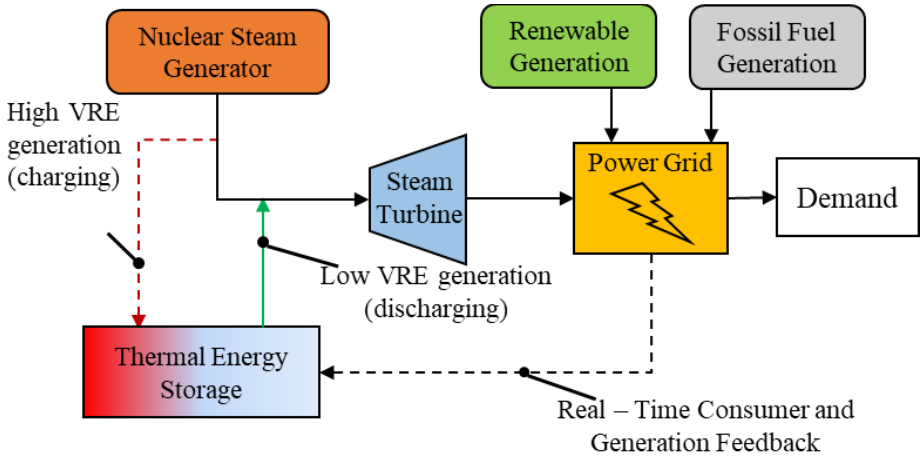

Fig. 1. TES integrated with nuclear power and renewables to meet peak demand and smooth transients created by the variability in demand and generation of renewable energy.

TES was used in industrial power applications as far back as 1929. In the Charlottenburg Power station in Berlin, Germany, a 67 MWh steam accumulator stored steam during periods of low demand and released steam during high demand [18]. Research and implementation stalled for over more than 40 years. In the 1970's, rising oil prices and a wave of new nuclear power plants provided renewed interest in TES to provide economical peaking power [37], [38]. More recent studies by Forsberg et al. and Denholm et al. have considered the potential benefits of nuclear power with TES to support renewable energy and decarbonize the electrical sector [17]–[20], [25], [26], [39], which is the leading source of direct carbon-dioxide emissions [40]. Forsberg et al. focus on the symbiotic benefits of TES with nuclear and VRE generation. The use of TES mitigates the impact of low-price electricity (during period of overgeneration) on the economic viability nuclear power plants [17]. The lower storage requirements of a baseload power plant require smaller storage capacities to support VRE. Denholm et al. [20] quantify this benefit by showing the potential improvement of capacity factor with TES compared to only load following (only load reduction) operation of a nuclear power plant.

Prior work on integration of TES within the nuclear Rankine cycle provides conceptual ideas for both charge and discharge from the power cycle. Curtis et al. [41] describe potential methods of integration but do not provide a technical assessment of the options. Integration options fall into two categories, either discharge to the primary (existing) Rankine cycle, or discharge to a secondary cycle. Curtis et al. list possible benefits and drawbacks for both options. Discharging to the primary cycle could provide faster response to grid fluctuations but as shown in the present work, peaking power is limited to modest values unless the turbines are replaced and modified extensively.

Discharging to a secondary cycle allows for high discharge powers and higher power plant efficiencies during baseload operation.

Prior technical modeling of nuclear power cycles with TES is limited to that by Gilli and Beckman [37]. They compared the cost of power to traditional peaking sources such as simple and combined cycle gas turbines to TES using steam accumulators that are discharged to a secondary cycle. Assuming a constant eight percent efficiency of conversion of heat to electricity, they estimate TES could produce lower cost power than other peaking sources. The benefit is highest for annual discharge durations >500 hours, or about 2 hours per day. Gilli and Beckman neglect the impact of the rate of charge and discharge on the design and performance of components of the primary and secondary Rankine cycles.

The present work is the first to model the impact of TES operation on thermodynamic performance of a nuclear plant. The thermodynamic model is developed to compare different approaches to integrating TES within the Rankine power cycle of the nuclear power. A component by component energy balance yields the effects of charging and discharging on the first law performance of the steam Rankine cycle over a range of operating conditions that might be encountered in the field and the second law efficiency of the TES. The first law performance is quantified by the capacity factor, discharge efficiency and Energy Production Ratio (EPR). The capacity factor used in Chapters 2 and 3 is the ratio of energy generated using TES over a cycle of charge and discharge. The discharge efficiency is the fraction of energy generated by the turbines from the stored thermal energy. The EPR is a capacity factor that includes baseload operation and is reported over a 24-hour period in Chapter 4. Options for storage material and conceptual

storage module designs are also described in Chapter 4. Estimates of storage material mass, volume and cost for the conceptual TES design are provided for two charge durations (four and eight hours) likely to be used in grid operation [42]–[44].

The model is based on use of TES with a pressurized water reactor, specifically the Westinghouse AP1000. Figure 2 is a simplified diagram of the steam Rankine cycle for the AP1000. This plant was selected because the temperatures and pressures are similar to the majority of nuclear power plants in the U.S. Steam exits the steam generator at constant temperature (271°C), pressure (55 Bar) and mass flow rate (1886 kg s^{-1}). The high-pressure steam is expanded in the high-pressure turbine (HPT) down to 10.5 Bar ($\chi = 0.88$). Using steam extracted from the HPT, steam is reheated to 251°C (9.5 Bar) before entering the low-pressure turbine (LPT). Steam enters the condenser at 0.1 Bar and $\chi = 0.88$, exiting at 44°C. A variety of approaches to charge and discharge the TES are modeled. To charge the TES, diverting steam before the HPT, moisture separator/reheater (MSR) and LPT to the TES are considered. For discharging, generating steam from the TES for either the LPT (primary cycle) or a dedicated secondary cycle are considered. Using the TES to heat condensate for the steam generator as suggested by Kluba and Field [45] is also considered in Chapter 4 and compared to two approaches to integrating the TES down selected from the results presented in Chapters 2 and 3.

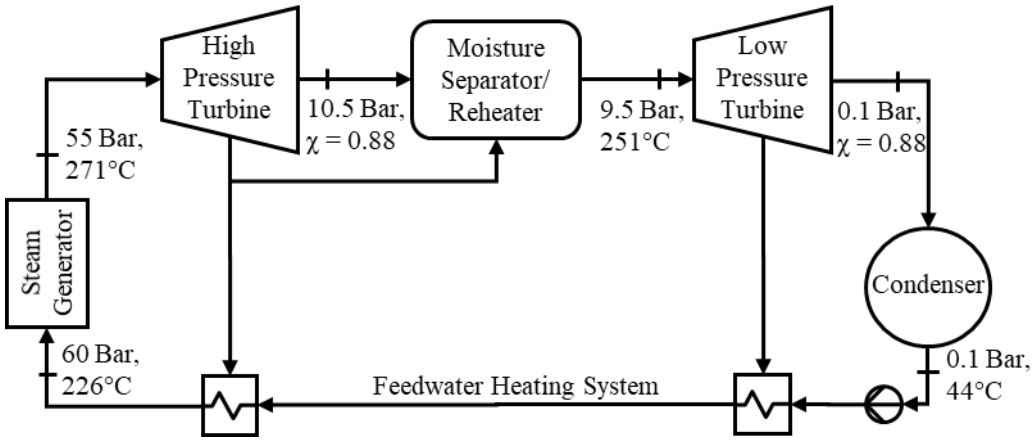

Fig. 2. Simplified diagram of the AP1000 showing key inlet and outlet state points of components.

Chapter 2 establishes the basis for the thermodynamic model and is published in the Journal of Energy Conversion and Management [46]. The chapter applies the model to a TES configuration with charge and discharge from/to the primary cycle as shown in Fig. 3 and compares the capacity factor for a charge/discharge cycle to steam bypass. Steam bypass is a non-storage option that would reduce the load of the power plant by diverting steam from the turbines to the condenser, potentially reducing VRE curtailment. Steam bypass cannot increase power at times of high demand. This chapter provides an analysis limited to a discharge power of 10% of the baseload power, which was selected to avoid significant changes to the primary cycle turbomachinery. The TES configuration provides up to a 9.8% increase in capacity factor compared to steam bypass for an operating scenario in which the TES in charged in an hour at varying rates and completely discharged at varying rates. The increase in relative capacity factors increases with increasing rate of charge and discharge. The co-authors Tran and Stein contributed to the section on selection of storage materials including a description of their independent work on the development of novel storage materials with tunable phase transition temperatures [47].

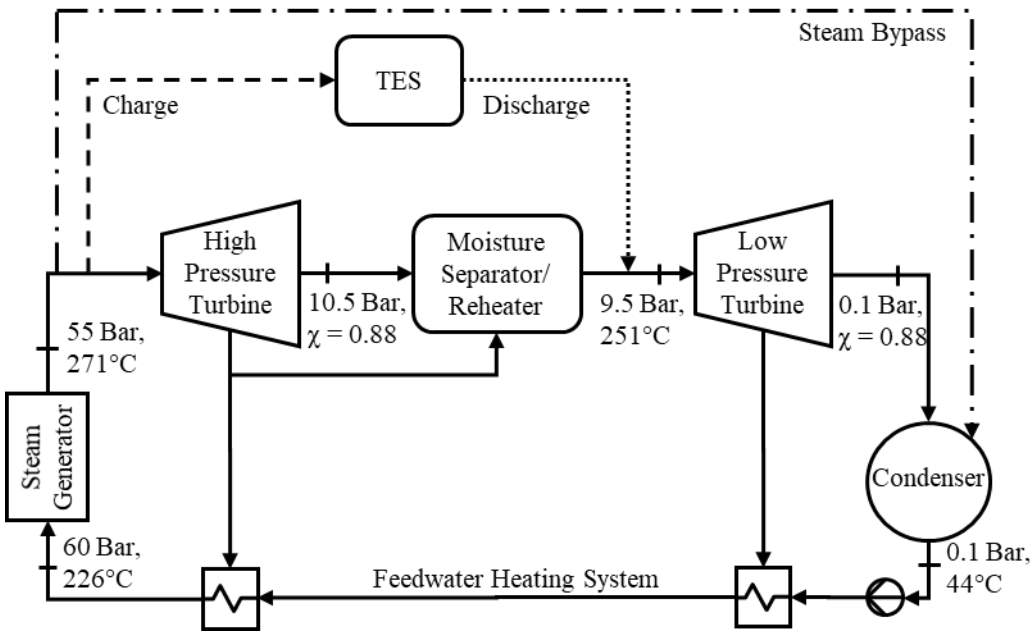

Fig. 3. TES configuration with charge and discharge from/to the primary cycle as analyzed in Chapter 2. TES charge is indicated by dashed lines. Discharge is indicated by dotted lines. Steam bypass is indicated by dash-dot lines.

The work in Chapter 3, published in the ASME Journal of Heat Transfer [48], considers a broader range of TES concepts with the aim of identifying approaches to improve capacity factor through the use of a secondary cycle. The configurations, shown in Fig. 4, include diverting steam prior to the (a) high-pressure turbine, (b) moisture separator/reheater and (c) low-pressure turbine for TES charging and discharge to a secondary cycle for all of the charging options. Discharge temperatures and pressures for the secondary cycle are selected to maximize discharge efficiency and TES exergetic efficiency. Capacity factor is calculated over a four-hour charge duration and three-hour charge duration. These durations are a likely scenario in grid operation [49]. Discharge power is set to 10% above the baseload, allowing direct comparison to the TES configuration exhibited in Chapter 2. Discharge of the TES to a secondary cycle with steam diverted from the LPT during charge has the highest relative capacity factor of all options considered. The relative capacity factor is 50% higher than that of the configuration

modeled in Chapter 2. Diverting steam after the HPT improved the efficiency of the cycle during charging. Discharging to the secondary cycle increased efficiency during charging and baseload because the steam turbines do not require modification as is the case for discharge to the primary cycle.

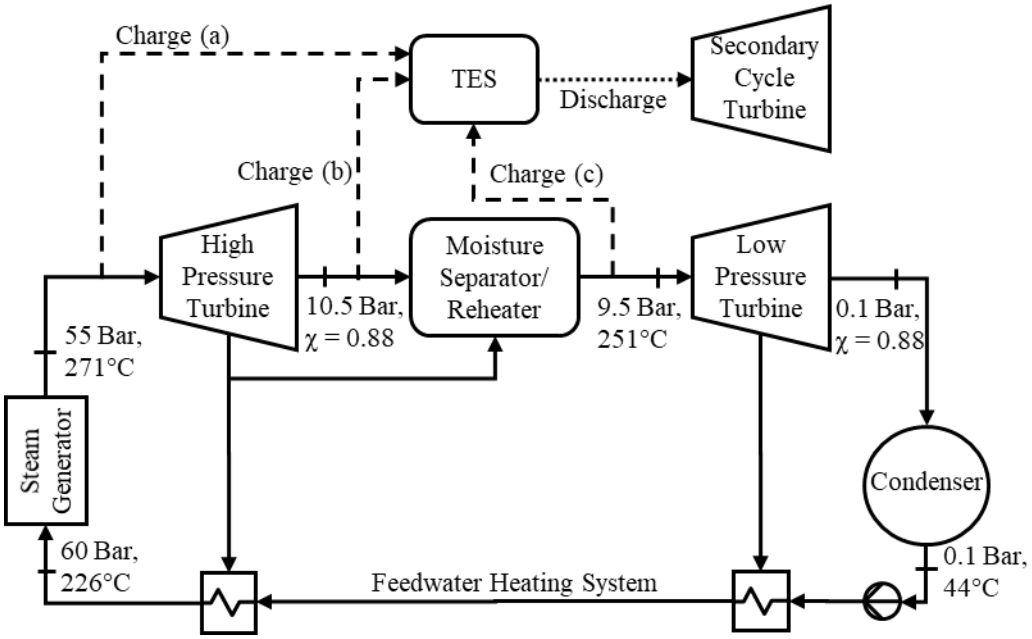

Fig. 4. TES configurations with discharge to a secondary cycle as analyzed in Chapter 3. Three configurations distinguished by the locations for charging are shown: (a) HPT inlet, (b) HPT outlet and (c) LPT inlet.

In Chapter 4, the thermodynamic model is applied to evaluate two configurations identified by the results of Chapters 2 and 3 and an option presented by Kluba and Field [45] over a range of operating parameters that might be encountered in grid operation of a TES system. The three configurations are: I) charge using high-pressure steam and discharge to the LPT, II) charge using high-pressure steam and condensate discharge to the steam generator and III) charge using low-pressure steam and discharge to a secondary cycle. Configuration II was suggested and optimized by Kluba and Field [45] in a study published concurrently with the work in Chapter 3. Parameters include charge duration, discharge duration, discharge power ratio (DPR) and round-trip efficiency of the TES. The

discharge power ratio is the ratio of power generated during TES discharge and the power generated in baseload without TES. The round-trip efficiency of the TES is the ratio of thermal energy able to be discharged from the TES and the thermal energy deposited in the TES during charge. Storage capacities of the TES and costs of storage material are estimated for case studies based on likely operating parameters. The results are interpreted to suggest favorable ranges of parameters and to compare the merits of the three configurations.

Chapter 5 provides concluding remarks and suggestions for future work.

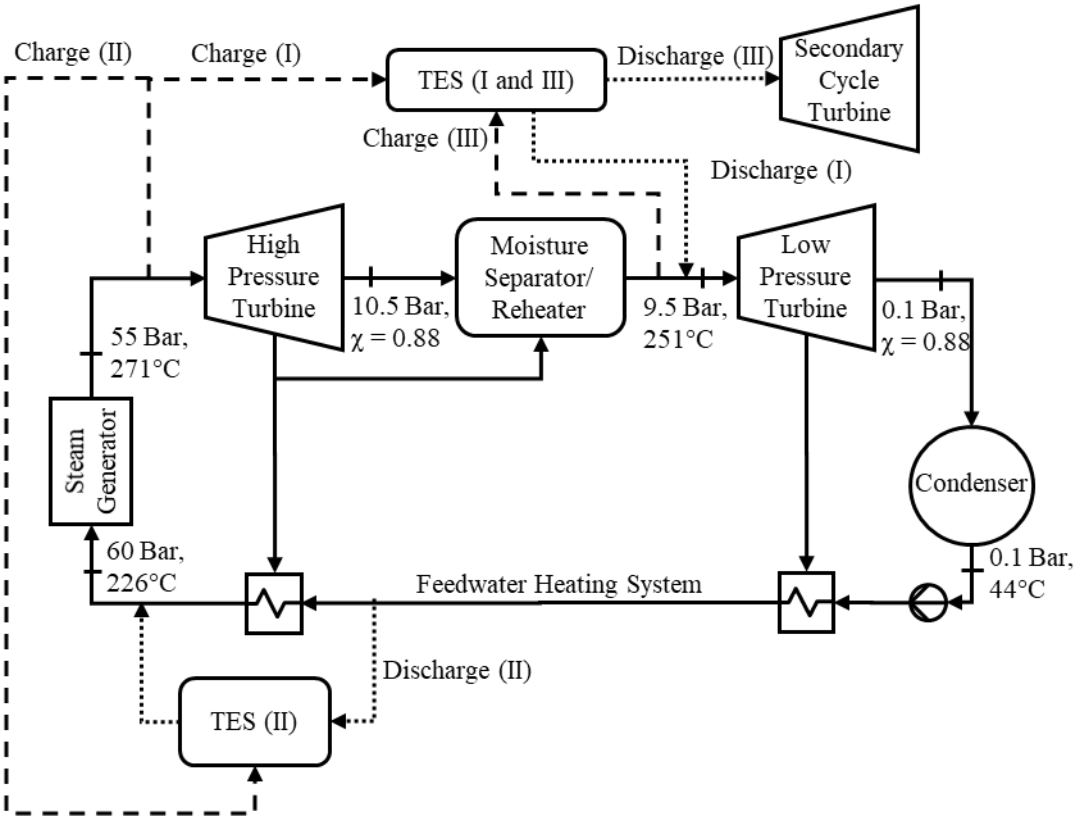

Fig. 5. Configurations of TES used in the parametric study of Chapter 4: (I) HPT inlet steam for charging and discharge to LPT, (II) HPT inlet steam for charging and discharge heated condensate for the steam generator and (III) LPT inlet steam for charging and discharge to a secondary cycle.

2 Model of the impact of use of thermal energy storage on operation of a nuclear power plant Rankine cycle[1]

Increasing electricity production by solar and wind energy is projected to impact the stability of electricity grids and consequently may limit the growth of renewable electricity generation. This issue can be ameliorated in part by increasing the flexibility of baseload power plants. A thermodynamic analysis of thermal energy storage (TES) coupled with a nuclear-powered Rankine cycle as one approach of increasing baseload flexibility is presented. During periods of excess capacity, the high-pressure steam supply is used to charge the TES. When electricity generation above the baseload capacity is required, the TES is discharged to generate steam for expansion in the low-pressure turbine. Pressure, temperature, and enthalpy state points within the cycle are presented over a range of charge and discharge rates. The capacity factor over a charge/discharge cycle is up to 9.8% higher than that of the same plant operated with steam bypass. This benefit increases with increasing charge and discharge power. With TES, the thermal-to-electrical efficiency is stable over a wide range of discharge rates. The results support future development of TES systems for baseload thermal power plants in a power grid in which renewable energy is prioritized.

2.1 Introduction

The U.S. Energy Information Administration projects a 1000% growth in variable renewable energy (VRE) generation, such as photovoltaic solar and wind energy, by 2050 [1]. With electrical demand predicted to stay at the current level, even with increased

[1] This chapter is based on the article …..

demand from electric vehicles [3], the implementation of additional VRE necessitates reductions in generation from baseload power plants and is projected to increase grid instability [50]. The California Independent System Operator currently procures 300-400 MW to account for differences between demand and generator output [51]. As more renewables are deployed, the need for storage to provide regulation and load following capability will increase [3]. A reduction in inertial response is observed when wind accounts for 10% of total generation [52]. Penetration above 20% requires curtailment of output to maintain necessary grid services [53]. Greater power plant flexibility and energy storage are viewed as key solutions to maintaining grid stability [3], [50], [54].

Current baseload thermal power plants have limited ability to modulate power output. The inflexibility is due largely to thermal cycling which can lead to component failure and increasing operations and maintenance costs [27]. The focus of the present study is use of thermal energy storage (TES) to provide increased flexibility of thermal power plants. TES is one of several storage options, including pumped hydro storage, compressed air energy storage and battery storage [12]. TES is unique because it can be integrated directly into the steam power cycle. Thermal power plants used with TES could provide a portion of the 140 GW storage output capacity predicted to be required to meet 50% VRE penetration [3].

Utility scale TES has unique requirements. To compensate for off-peak wind generation, a minimum of 500 MWh_e is required with power rates of change similar to conventional power plants [55]. The first installation of TES with a conventional power plant was a 67 MWh pressurized water storage system installed in 1929 at the Charlottenburg thermal power station in Berlin [56]. In the 1970's, both an economic

analysis of TES as a peaking power source [37] and reviews of storage options for pre-1985 coal and nuclear power plants [57] were published. Over the past decade there has been a resurgence of interest in TES for modern power plants operating in electrical markets with high penetration of wind and solar. Denholm et al. [20] estimate storage would increase the capacity factor of a nuclear power plant by about 2.5% compared to load following operation with the assumptions of a renewable penetration of 60% and discharge of the TES equal to 110% of baseload power during periods of peak demand. Further increases in discharge power would increase the overall capacity factor, but based on commercial specifications for steam turbines, a 10% increase in power is the maximum possible without increasing the size of the turbine [58]. Denholm et al. assume heat from the nuclear reactor is stored directly as opposed to storing the heat of steam produced in the steam generator. Forsberg [39] puts forth a compelling case for TES with nuclear energy based on the current and emerging electrical market. In California's market, he estimates storage requirements for nuclear energy would be 4% of daily nuclear generation compared to 36% and 21% for wind and solar, respectively [39]. In addition to lower storage requirements, the cost per kilowatt hour of TES is considerably less than other electrical energy storage options [11]. Despite the positive attributes of TES, prior studies have not fully considered how TES impacts operation of a thermal power plant, particularly for the case considered in the present work in which TES is integrated into an existing, as opposed to redesigned, Rankine power cycle. Incorporating storage into existing baseload thermal plants is an important consideration because it is projected that new generation capacity from now to 2050 will be dominated by solar energy [1].

Figure 6 motivates an analysis of TES integrated with thermal baseload power plants. The top portion of the figure illustrates three Rankine power block configurations for (a) a conventional baseload power plant, (b) a plant in which flexibility in power generation is provided by bypassing a portion of the steam from the steam generator from the turbines to the condenser (referred to as steam bypass) and (c) a plant in which TES is charged with steam during periods of high VRE and discharged during periods of low VRE. For each configuration, an illustrative plot of power versus time in a grid with high penetration of VRE is shown (bottom). In a conventional baseload plant (Fig. 6(a)), the steam generator operates at full output and all the steam is expanded in the steam turbine. Baseload and renewables meet consumer demand for $t_0 \leq t \leq t_1$. For $t_1 \leq t \leq t_2$, baseload plus renewable generation exceeds demand and curtailment of renewable generation is required as indicated by the shaded region. For $t_2 \leq t \leq t_3$, baseload plus renewable generation briefly meet consumer demand. As renewables decline for $t_3 \leq t \leq t_4$, peaking generation is required. Figure 6(b) shows the same power plant operated with steam bypass directly from the steam generator to the condenser. This approach provides greater flexibility without redesign of the plant, but the energy of the steam that bypasses the turbines is lost. For $t_1 \leq t \leq t_2$, baseload power is reduced as a fraction of generated steam bypasses the turbine (dashed line) and renewable generation is used to full capacity. For $t_2 \leq t \leq t_3$, renewable generation decreases and steam bypass is no longer used. For $t_3 \leq t \leq t_4$, peaking generation is required, identical to the baseload plant. Steam bypass to the condenser can reduce steam mass flow rate to the turbine by 70% [59]. The capacity factor is reduced, and consequently, the levelized cost of energy is increased [20]. The same power plant with steam diverted to charge TES when excess power is available is shown in Fig. 6(c). When renewable

generation peaks for $t_1 \leq t \leq t_2$, a fraction of the steam from the steam generator bypasses the turbine and charges the TES.

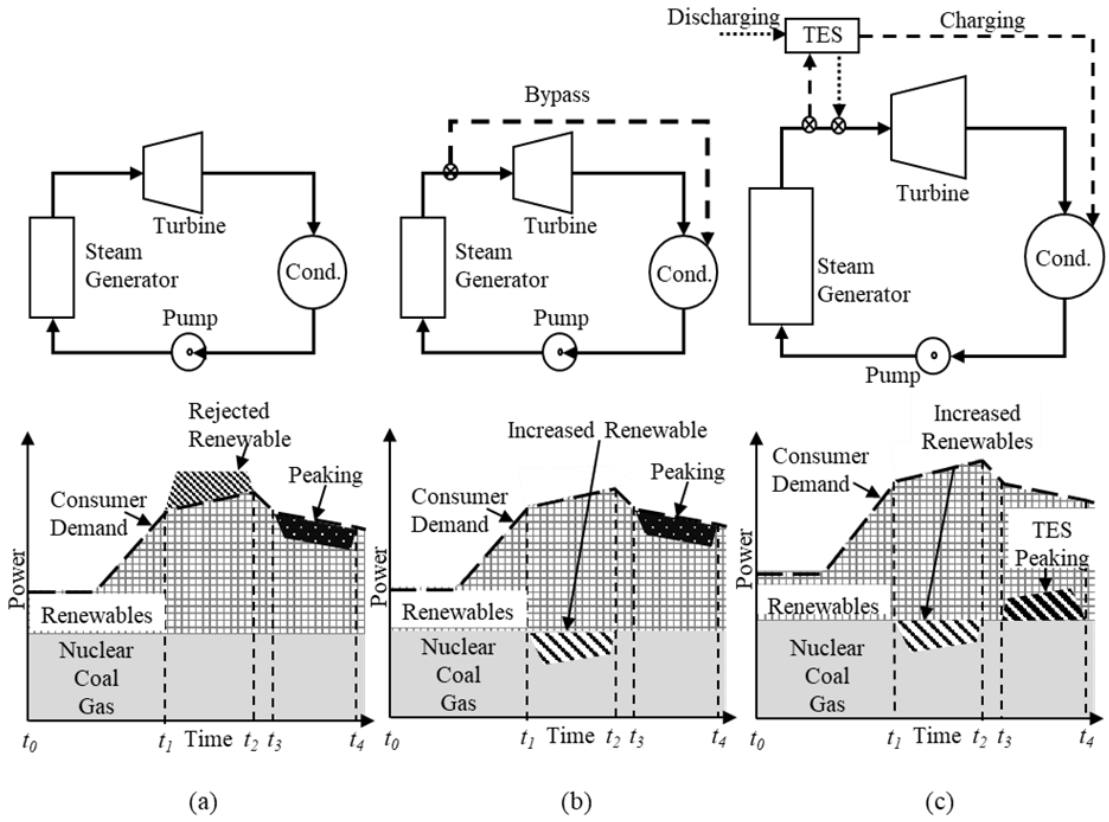

Fig. 6. Simple power block configurations and illustrative power grids for (a) conventional baseload power plants, (b) flexible operation using steam bypass to the condenser, and (c) flexible operation using TES.

The steam exiting the TES during charging is combined in the condenser with the fraction of steam expanded in the turbines (dashed line). At t_2 the power plant returns to full output. For $t_3 \leq t \leq t_4$, the TES is discharged and the generated steam passes through the turbine providing peaking power (dotted line). The charge and discharge of the TES are indicated by the shaded areas. Operating with TES improves the capacity factor compared to steam bypass to the condenser.

This chapter presents a thermodynamic analysis of the three plant configurations in Fig. 6 using a nuclear power plant as an illustrative example. The model yields operating

state points for a range of anticipated operating conditions. The results demonstrate the advantages of TES over bypass of steam to the condenser and elucidate the impact of operation of the TES on turbine and overall plant operation.

2.2 Nuclear Power Plant

Nuclear energy has been impacted by increased renewable energy production with a significant reduction in profitability over the last 10 years [36]. While economics [36] and public opinion [35], [60] are affecting future installations of nuclear power plants, nuclear energy is one means of reducing greenhouse gas emissions [35]. The Westinghouse AP1000 reactor and power cycle provides a convenient starting point for evaluation of TES in a baseload nuclear plant; operating conditions such as pressures, temperatures and mass flowrates are known [29], [61]. The AP1000 is a relatively new design with modular construction and safety improvements [62] over current power plants and the power cycle temperatures and pressures are similar to other nuclear power cycles operating in North America [63].

2.2.1 Baseload Operation

A simplified flow diagram of the dual pressure power cycle system is shown in Fig. 7. Baseload operation is indicated by solid lines. Steam bypass is indicated by dashed lines. In baseload operation, water enters the steam generator at 226.7°C and 60 Bar (State Point (SP) 8). Steam exits the generator at 271°C and 55 Bar at 1886 kg/s (SP 1). Of the total mass flow rate, 5% (SP 1a) provides thermal energy for moisture separation/reheating (MSR). The remainder (SP 2) enters the high-pressure turbine (HPT). At an intermediate stage, steam is extracted from the turbine to the two high pressure feedwater heaters (SPs 15 and 16). Steam exits the HPT turbine (SP 3) at 10.5 Bar with a quality of 0.88. Moisture separation/reheating to 251°C (SP 4) prevents damage to downstream components.

Moisture separation/reheating results in a pressure drop of 1 Bar. The superheated steam enters the low-pressure steam turbine (LPT) (SP 4) at 251°C and 9.5 Bar. The four extraction points (SPs 9–12) provide energy to heat the feedwater. Steam enters the condenser (SP 5) at 0.1 Bar and a quality of 0.89. The pressure of the subcooled liquid exiting the condenser (SP 6a) is elevated to 30 Bar (SP 7). Extractions from the LPT heat the condensate, increasing the overall thermal efficiency of the power plant. After exiting a deaerator, additional feedwater heating and an additional pump increase the condensate temperature and pressure to the steam generator inlet conditions (SP 8). Pressures at the inlet, extraction points and outlets are listed in Table 1.

Net power output of the power plant is 1051 MW in baseload operation. Net power ($\dot{W}_{\mathrm{out,PP}}$) is the sum of the work of the high pressure ($\dot{W}_{\mathrm{HPT}}$) and low pressure ($\dot{W}_{\mathrm{PP}}$) turbines minus the work of the feedwater pumps ($\dot{W}_{\mathrm{FWP}}$).

$$\dot{W}_{PP} = \dot{W}_{HPT} + \dot{W}_{LPT} - \sum \dot{W}_{FWP} \tag{1}$$

Overall power plant efficiency η_{PP} is 0.31, where

$$\eta_{PP} = \frac{\dot{W}_{PP}}{\dot{Q}_{in,SG}}, \tag{2}$$

and $\dot{Q}_{\mathrm{in,SG}}$ is the heat input to the steam generator.

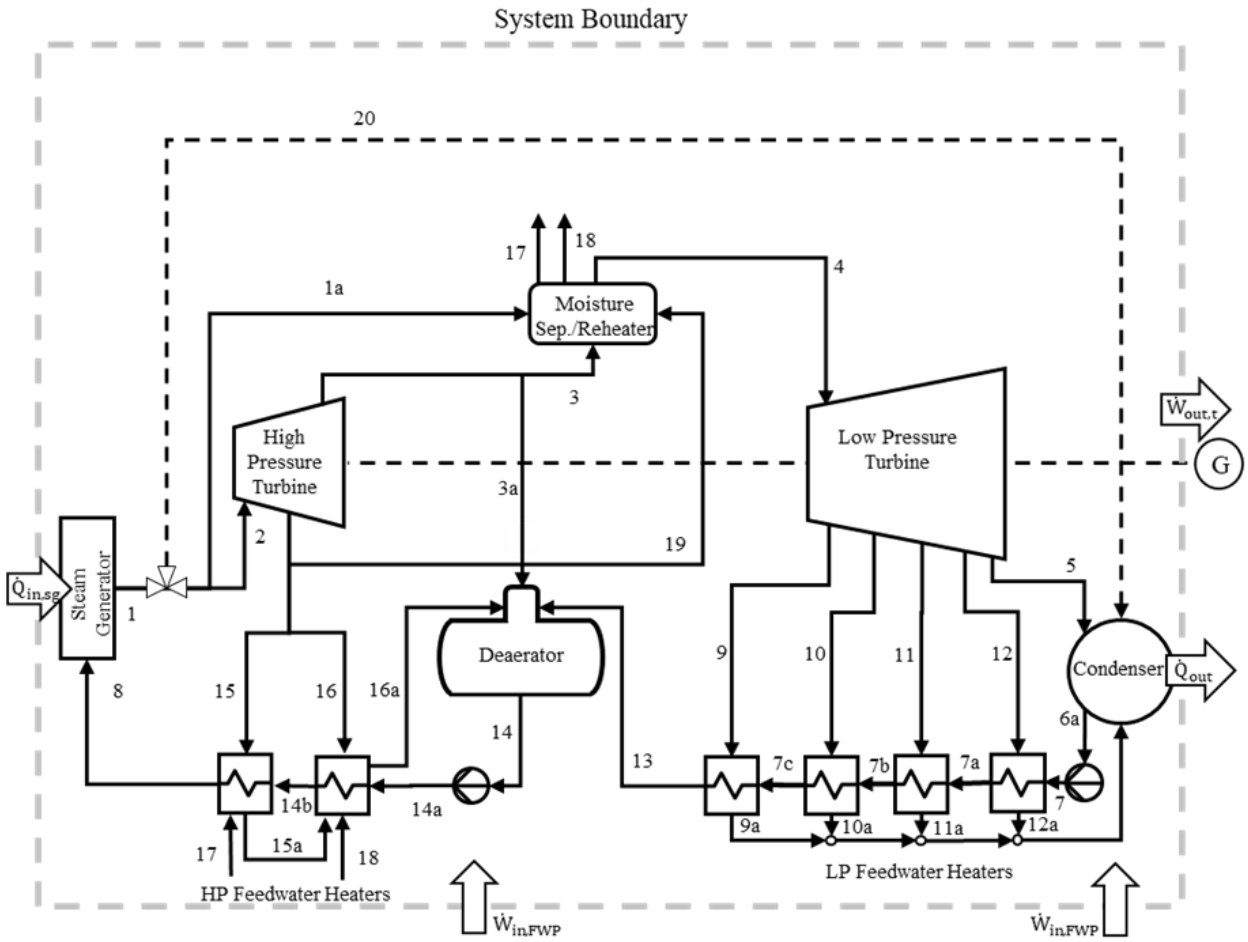

Fig. 7. Simplified diagram of baseload (solid lines) and steam bypass (dashed lines) for the AP1000 Rankine steam cycle [29], [61]

Table 1. AP1000 baseload state points [29], [61]

State Point	ṁ [kg/s]	P [Bar]	T [°C]	χ [-]	h [kJ kg^{-1}]	s [kJ kg^{-1} K^{-1}]
1	1886	55	271	1	2791	5.93
1a	86	55	271	1	2791	5.93
2	1800	55	271	1	2791	5.93
3	1200	10.5	182.02	0.88	2541	6.05
4	1200	9.5	251	1	2947.3	6.96
5	1000	0.1	45.81	0.89	2322.7	7.33
6a	1200	0.1	44	0	184.3	0.63
7	1200	30	44.28	0	188	0.63
7a	1200	30	67.82	0	286.3	0.93
7b	1200	30	91.48	0	385.5	1.21
7c	1200	30	116.81	0	492.2	1.49
8	1886	60	226.7	0	975.5	2.57
9	50	3.5	157	1	2772.4	7.04
10	50	3	144	1	2748.7	7.05
11	50	1.5	111.35	0.98	2647.9	7.11
12	50	0.5	81.32	0.94	2504.2	7.2
13	1200	30	138.26	0	583.4	1.49
14	1886	30	192.02	0	817.3	2.25
14a	1886	60	192.64	0	821.4	2.25
14b	1886	60	209.85	0	898.5	2.42
15	90	30	233.86	0.94	2696.9	5.98
16	90	30	233.86	0.94	2696.9	5.98
16a	500	30	233.86	0.64	2158.9	2.65
17	86	30	233.86	0.35	1629.6	3.87
18	360	30	233.86	0.49	1885.4	2.65
19	360	30	233.86	0.94	2696.9	5.98

2.2.2 Steam Bypass

One method for reducing the power in thermal power plants without a reduction in baseload steam generation is to divert a fraction of the steam from the turbines to the condenser [59]. The steam generator, condenser and pump operate at baseload levels. The fraction of steam generator mass flow rate, ṁ, sent to the condenser (F_{BP}) is

$$F_{BP} = \frac{\dot{m}_{20}}{\dot{m}_1}, \tag{3}$$

where the subscripts represent state points in reference to Fig. 7. Bypassing a fraction of the steam reduces the mass flow rate to the HPT and LPT. In the present study, the fraction of steam mass flow rate that is bypassed is varied from 0 to 0.52. The upper limit for F_{BP} is set to 70% of the maximum mass flow rate of the LPT, consistent with current turbine bypass limits [59] and published correlations of isentropic efficiency and fractional mass flow rate [64]. Details of the model of the turbines during bypass operation are described in section 2.3.2. Varied and fixed parameters for bypass are listed in Table 2.

Table 2. Parameter values for bypass and charging operation.

Parameter	Symbol	Value
Bypass mass fraction	F_{BP}	0 – 0.52
Charging mass fraction	F_C	0 – 0.52
HPT inlet temperature	T_2	271°C
HPT inlet pressure	P_2	55 Bar
LPT inlet temperature	T_4	251°C
Condenser pressure	P_5	0.1 Bar
Moisture separation/reheating Pressure drop	ΔP_{MSR}	1 Bar
Condensate pump work	$\dot{W}_{FWP}$	12.75 MW_e
Steam generator heat input	$\dot{Q}_{SG}$	3431 MW_{th}

2.2.3 Integrated TES

The scientific literature provides limited guidance for integration of TES in a conventional power plant. Gilli and Beckman [37] suggest diverting steam from the high-pressure steam supply for charging the TES. At discharge, the stored thermal energy drives a second set of turbines. The secondary power conversion system works for preplanned peaking generation, but short-term fluctuations in energy could be better met by discharging the TES back into the main power cycle as described by Curtis et al. [41]. Discharge to the main power cycle increases flexibility. Any secondary power conversion system will have a required minimum start up time and power output [41].

Figure 8 shows the modelled configuration of the AP1000 power cycle with integrated TES. In baseload, the cycle operates in the same manner as the cycle indicated by solid lines in Fig. 7. At times where power reduction is required, the TES is charged. A fraction of steam at 271°C and 55 Bar (SP 21) bypasses the HPT and LPT turbines and flows to the TES (dotted dashed line). The charging mass fraction (F_C) is the fraction of generated steam diverted to charge the TES:

$$F_C = \frac{\dot{m}_{21}}{\dot{m}_1}. \tag{4}$$

The charging mass fraction is varied from 0 to 0.52. In the TES, the steam is cooled isobarically. Water exits the TES at 46°C (SP 22) and is combined in the condenser with the steam exiting the turbine (SP 5) and the water exiting the feedwater heaters (SP 12a). Subcooled water exits the condenser (SP 6a).

When peaking power is required, the TES is discharged by flowing water stored at ambient through the TES. The stored water is pressurized to P_4 and enters the TES (ideally counter flow to the direction of steam flowing through the TES during charging) at 25°C (SP 23). The discharge mass flow rate is defined as a fraction of the mass flow from the steam generator during baseload operation, F_D.

$$F_D = \frac{\dot{m}_{23a}}{\dot{m}_1} \tag{5}$$

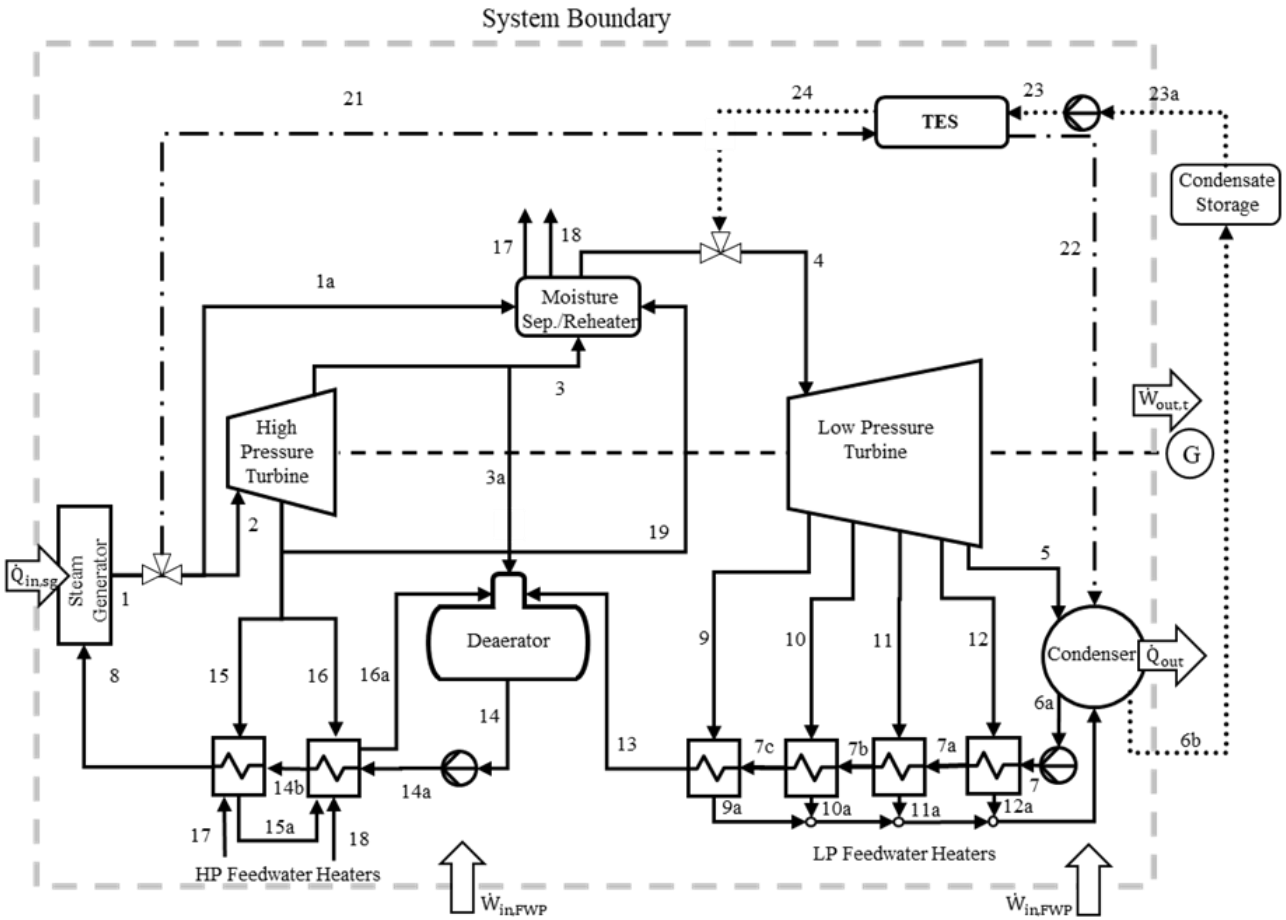

Fig. 8. Simplified diagram of AP1000 with TES bypass of the HPT and LPT during charging and reintegration in the LPT during discharging.

In the TES, the stored water is preheated to saturation (at P_4), evaporated and then superheated to 251°C (SP 24). The superheated steam flows to the LPT. The steam mass flow rate through the LPT is the sum of that from the TES and from the moisture separator/reheater. In the model, the discharging mass fraction, F_D, is varied from 0 to 0.1. The upper limit of $F_D = 0.1$ is selected with the assumption that this fraction represents the highest increase in mass flow rate that can be accommodated by the LPT without replacement. A modification of the steam flow path might be required [58]. The flow exiting the LPT enters the condenser at 0.1 Bar (SP 5). At the condenser exit, a fraction of the total mass flow rate equal to the flow rate to the TES ($\dot{m}_{24}$) is returned to storage (SP 6b) for recirculation (SP 23a).

A detailed design of a TES module for this application is beyond the scope of the present work, but we consider conceptual designs in order to discuss storage materials. Assuming a steam inlet temperature of 271°C and water exit temperature of 46°C and discharging from a pressurized liquid at 25°C to a superheated steam at 251°C a single stage (Fig. 9(a)) and multistage (Fig. 9(b)) TES can be envisioned. In a single stage TES module, the required working temperature of the storage material would be 25 – 271°C. A two stage module would facilitate use of two materials and reduce entropy generation [65]. During charging, steam would enter Stage A at 271 °C at a quality $\chi = 1$ and exit at 271 °C at $\chi = 0$. In Stage B, the saturated steam would be cooled to 46 °C. During discharge, the flow direction through the two stages would be reversed. In Stage B, water at 25 °C and P_4, which is approximately 10 Bar over the range of discharging mass fractions consider, would be heated to saturation at P_4, i.e. approximately 180 °C. In Stage A, the saturated steam would be superheated to 251 °C and would then flow to the LPT.

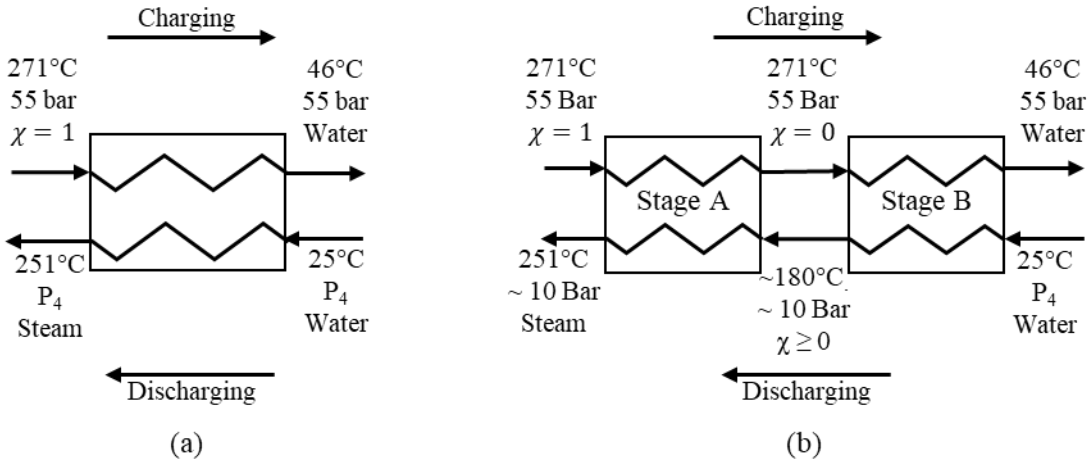

Fig. 9. Conceptual TES systems for (a) single stage and (b) multistage concepts operating between 25 and 271°C.

Characteristics that define desirable materials are high specific energy density (kJ kg^{-1}), energy density (MJ m^{-3}), chemical stability, durability, specifically the ability to undergo thousands of cycles for phase change materials (PCMs), and compatibility with materials of construction. A non-exhaustive list of storage materials for the TES concepts shown in Fig. 9 are provided in Tables 3 and 4. The tables include key material properties and estimated material costs. The specific energy density (u), energy density (e) and heat storage cost (c) are calculated by Eqs. (6), (7) and (8), respectively. The specific heat (c_P) and density (ρ) are evaluated as averages over the relevant temperature range (ΔT), when temperature dependent data are available.

$$u = c_p \Delta T + h_{fus} \tag{6}$$

$$e = \rho u \tag{7}$$

The heat storage cost (\$ kWh_{th}^{-1}) is based on the specific energy density and the per unit mass material cost, c.

$$c = u^{-1} c_{mat} \left[3600 \frac{\text{kJ}}{\text{kWh}}\right] \tag{8}$$

Table 3. Potential sensible heat storage materials for single stage TES for 25 to 271 °C.

Material	ρ [kg m^{-3}]	c_P [kJ kg^{-1} $°K^{-1}$]	u^1 [kJ kg^{-1}]	e^1 [MJ m^{-3}]	c_{mat} [\$ kg^{-1}]	c [\$ kWh_{th}^{-1}]
Concrete [66]	2200 at 300°C	0.85 at 300°C	209	460	0.05	0.86
Silica [66]	1820 at 450°C	0.8 at 450°C	247	448	1.00	15
Therminol VP-1 [67]	960[2]	1.9[2]	474	445	3.96	30

[1] Evaluated over the temperature range of 25 – 271°C
[2] Average values over 25 – 271°C

Table 4. Potential materials for latent heat storage in stage A of a two stage TES.

Material	T_m [°C]	ρ [kg m^{-3}]	h_{fus} [kJ kg^{-1}]	e^1 [kJ kg^{-1}]	u^1 [MJ m^{-3}]	c_{mat} [\$ kg^{-1}]	c [\$ kWh_{th}^{-1}]
$NaNO_3$:NaOH (41:59 mol %) [68]	266	2183	292	292	637	0.5 [69]	6
$NaNO_2$ [70]	270	2170	201	201	436	0.51 [71]	9
LiCl:LiOH (37:63 mol %) [72]	262	1550	485	485	752	17–22 [73]	148
Bismuth [74]	271	9780	271	271	2650	40 [75]	531

[1] Energy densities are based on h_{fus} and listed density.

Table 3 lists three potential sensible heat storage materials for the single stage module illustrated in Fig. 9(a) for 25 – 271°C. Concrete, silica, and Therminol VP-1 heat transfer fluid have appropriate working temperatures. Energy densities are equivalent, but concrete has the lowest material cost per unit mass.

In a two-stage module, we envision Stage A would be latent heat storage, which is well suited for condensing and evaporating steam. Stage B would likely be sensible heat storage due to the large temperature difference. For Stage A, we assume the TES material operates isothermally at T_m when calculating the energy densities. Table 4 lists PCMs with $251 \leq T_m \leq 271$°C. Energy densities represent the latent heat of fusion. Eutectic mixtures of hydroxide, nitrate, nitrite or chloride salts have acceptable melt temperatures from 251

- 271°C. For example, eutectic mixtures of $NaNO_3$ and NaOH provide specific energy densities of approximately 290 kJ kg^{-1} and energy densities of approximately 640 MJ m^{-3}. Variations in molar compositions of $NaNO_3$:NaOH affect T_m but result in similar energy densities [68]. Sodium nitrate has lower energy densities (201 kJ kg^{-1} and 436 MJ m^{-3}), and provides another low-cost option. A eutectic mixture of lithium chloride and lithium hydroxide has high storage density (485 kJ kg^{-1} and 752 MJ m^{-3}) but there is a tradeoff between the higher density and material cost. The difference in volume between solid and liquid states of salts requires special consideration for storage vessel design. For example, the volume of liquid $NaNO_3$ is 10.7% higher than the solid phase [76].

Bismuth is the only non-radioactive single metal latent heat storage candidate with an appropriate melt temperature (271 ˚C). Although bismuth has a low specific energy density (271 kJ kg^{-1}) compared to other latent heat storage materials, it provides a comparable volumetric energy density (2650 MJ m^{-3}). Tran et al. and Liu et al. showed that the melting temperature of bismuth is tunable between 236 and 271 ˚C by synthesizing matrix-confined bismuth nanoparticles [47], [77], [78], so that optimization of the phase transition temperature for a particular system of interest is possible. The tunable phase change temperature method provides an additional tool for making suitable TES material.

2.3 Model

2.3.1 TES

The TES is characterized by the round-trip efficiency (η_{RT}) equal to the ratio of energy discharged (Q_D) to energy charged (Q_C).

$$\eta_{RT} = \frac{Q_D}{Q_C} \tag{9}$$

In the present work, we first consider an idealized TES with η_{RT} assumed to be unity. Inherent to this assumption are adiabatic boundaries and no limitation to heat transfer. The model is run for $0 \leq F_C \leq 0.52$ in increments of 0.01 and $0 \leq F_D \leq 0.1$ in increments of 0.005. In practice, η_{RT} will depend on storage material, size and physical configuration of the TES module. To illustrate the impact of η_{RT} on the overall cycle performance, we present results for $0.5 \leq \eta_{RT} \leq 1$ with $F_C = 0.52$ and $F_D = 0.1$.

The duration of charging is arbitrarily selected as 1 hour and outlet conditions are assumed constant over this duration. The energy stored is determined by Eqn. (10).

$$Q_C = \dot{m}_1 F_C (h_{21} - h_{22}) \Delta t_C \tag{10}$$

The duration of the discharge (Δt_D) is determined by Eqn. (11).

$$\Delta t_D = \frac{\eta_{RT} Q_C}{\dot{m}_1 F_D (h_{24} - h_{23})} \tag{11}$$

The outlet condition is assumed constant over the duration of discharging (P_4 and 251°C). At the inlet, water stored at ambient conditions (25°C, 1 Bar) is pressurized to the LPT inlet pressure (P_4). The pump work is calculated via Eqn. (12).

$$\dot{W}_{FWP} = \dot{m}_1 F_D \eta_{FWP} (h_{23}(P_4, s_{23a}) - h_{23a}) \tag{12}$$

The pump isentropic efficiency (η_{FWP}) is assumed equal to 0.82. The pressurized water is heated isobarically in the TES to 251 °C.

2.3.2 Turbine Performance

The work output from a steam turbine with a single inlet, and multiple exit points is given by Eq. (13).

$$\dot{W}_T = (\dot{m}h)_{in} - \sum (\dot{m}h)_{out} \tag{13}$$

Outlet points include the extraction flows (SP 15, 16, 19 for the HPT and 9–12 for the LPT in Fig. 8) for feedwater heating and the turbine outlet. In baseload operation, power generated by the HPT and LPT is calculated using the enthalpies listed in Table 1. In partial loading of the turbines during steam bypass or charge or discharge of the TES, Stodola's ellipse [79], often referred to the Ellipse Law or Law of the Cone given in Eq. (14), is used to predict the non-linear effect of modified mass flow rate on pressure drop.

$$\left(\frac{\dot{m}}{\dot{m}_{ref}}\right)^2 = \frac{P_{in}^2 - P_{out}^2}{P_{in,ref}^2 - P_{out,ref}^2} \tag{14}$$

The reference condition is at the maximum flow rate. The maximum flow rate for the HPT and LPT is the baseload mass flow rate plus the maximum discharging mass flow rate at $F_D = 0.1$[2]. During baseload operation, the LPT operates at partial load because during discharge the turbine must handle the baseload plus the discharge mass flow rate. The mass flow rate and reference pressures for the LPT during baseload and discharge are listed in Table 5. The pressure at the exit of HPT is adjusted to match the LP pressure during charge (or steam bypass). During baseload, no change in pressure is needed. During bypass or charge, the pressure is reduced via throttling. During discharge, the exit pressure is increased by increasing the HPT inlet pressure. For example, at $F_D = 0.1$ the HPT inlet pressure is increased by 0.12 Bar over baseload operation. The very small increases in specific enthalpy and temperature are expected to be within the operating window of the steam generator.

[2] Change from publication to include highest mass flow rate for HPT and LPT

Table 5. Low Pressure Turbine reference mass flow rates and pressures

Value	Baseload	TES
$\dot{m}_{4,ref}$	1200 kg s^{-1}	1380 kg s^{-1}
$P_{12,ref}$	0.50 Bar	0.56 Bar
$P_{11,ref}$	1.5 Bar	1.68 Bar
$P_{10,ref}$	3.00 Bar	3.35 Bar
$P_{9,ref}$	3.50 Bar	3.90 Bar
$P_{4,ref}$	9.50 Bar	10.50 Bar

The turbines are modeled as sections based on the number of extraction points. For the HPT, one extraction divides the turbine into two sections. For the LPT, four extractions divide the turbine into five sections. Using Eqn. (14), calculation of the pressures in the turbine is sequential. In the HPT, the inlet pressure and temperature are fixed, and the extraction pressure is based on charge/discharge mass fraction. For the LPT, the inlet temperature and outlet pressure are fixed, requiring calculation of pressures starting with the last section of turbine. Specific enthalpies are calculated based on the section isentropic efficiency (η_T).

The isentropic efficiency of the turbine is the ratio of the work output ($h_{in} - h_{out}$) to the ideal turbine work output ($h_{in} - h_{out,ise}$).

$$\eta_T = \frac{h_{in} - h_{out}}{h_{in} - h_{out,ise}} \tag{15}$$

$$h_{out,ise} = h(P_{out}, s_{in}) \tag{16}$$

Modern steam turbine designs have isentropic efficiencies between 0.88 and 0.93. Efficiencies are reduced about 1% for every 1% moisture in the latter stages of the turbine [80]. Bartlett [64] provides a correlation for the reduction in isentropic efficiency with reduced mass flow rate. Curve fitting results in the off design isentropic efficiency (η_T) given by Eq. (17).

$$\eta_T = 0.84 - \left[-0.22\left(\frac{\dot{m}}{\dot{m}_{ref}}\right)^3 + 0.62\left(\frac{\dot{m}}{\dot{m}_{ref}}\right)^2 - 0.62\left(\frac{\dot{m}}{\dot{m}_{ref}}\right) + 0.22\right] \quad (17)$$

The maximum isentropic efficiency, 0.84 [29], is at the maximum flow rate of the turbine. The specific enthalpies at the extraction points vary with changing F_C and F_D. The mass flow rates of the extraction are adjusted to maintain a constant feedwater temperature increase in the feedwater heaters.

2.3.3 Power Plant Performance

In the analysis of the TES, we define a capacity factor equal to the ratio of work produced during a single charge/discharge cycle ($\dot{W}_{TES}$) to the maximum amount of work produced ($\dot{W}_{X,BL}$) over the same period in baseload operation:

$$CF_{TES} = \frac{\dot{W}_{TES}\Delta t_C + \dot{W}_{TES}\Delta t_D}{\dot{W}_{X,BL}(\Delta t_C + \Delta t_D)} \quad (18)$$

The impact of using TES as a means to control power with minimum modification to the plant is characterized by the relative capacity factor (CF_{TES}/CF_{BP}), which is the ratio of capacity factor with TES and the capacity factor with steam bypass.

$$CF_{TES}/CF_B = \frac{\dot{W}_{TES}\Delta t_C + \dot{W}_{TES}\Delta t_D}{\dot{W}_B\Delta t_C + \dot{W}_{X,BL}\Delta t_D} \quad (19)$$

The stored thermal to electrical efficiency (η_D) is the ratio of turbine work and stored heat during discharge given by

$$\eta_D = \frac{(\dot{W}_{TES} - \dot{W}_{X,BL})\Delta t_D}{Q_D}. \quad (20)$$

It is a key metric in consideration of the TES as a means to provide peaking power.

In addition to the performance of the turbines discussed in section 2.3.2, cycle performance depends on the behavior of the moisture separator/reheater, condensate pumps and TES. The change in total pump work changes less than 1% for all operating modes.

The moisture separator/reheater increases the temperature of the steam exiting the HPT using the flow from extraction SP 1a (Fig. 8). For both charging and discharging, it is assumed that the pressure drop in the moisture separator/reheater is 1 Bar, and the final superheat temperature is 251°C. In charging, the mass flow rate through the HPT is reduced, and the mass flow rate required by MSR is reduced accordingly as shown in Eq. (21).

$$\dot{m}_{1a,C} = (1 - F_C)\dot{m}_{1a,X,BL} \tag{21}$$

2.4 Results

The detailed behavior of the nuclear Rankine power cycle with TES is described in sections 2.4.1 and 2.4.2 with emphasis on the impacts of charging and discharging fractional mass flow rates on state points of the cycle for $\eta_{RT} = 1$. A comparison of operation of the cycle with TES to the same plant with steam bypass is presented in terms of the relative capacity factor and thermal to electrical efficiency in section 2.4.3. Section 2.4.3 includes the impact of η_{RT} on the relative capacity factor over the range $0.5 \leq \eta_{RT} \leq 1$ for $F_C = 0.52$ and $F_D = 0.1$.

2.4.1 Charging

The impact of varying charging mass fraction (F_C) on the mass flow rates, pressures, and enthalpies of the HPT and LPT is presented in Figs. 10 – 13 for $\eta_{RT} = 1$. First consider the HPT. Figure 5 shows the steam mass flow rates (a), pressures (b) and enthalpies (c) corresponding to the states points (indicated on Fig. 8) for $0 \leq F_C \leq 0.52$. At baseload conditions, represented by $F_C = 0$, the mass flow rate to the HPT ($\dot{m}_2$) is 1800 kg/s. It decreases with increasing charging mass fraction as steam is diverted to the TES. The pressure and specific enthalpy at the inlet of the HPT (P_2, h_2) remain constant with varying F_C because the steam generator is always operated at baseload conditions to avoid

physical changes to the power plant. The intermediate mass flow rates ($\dot{m}_{15}, \dot{m}_{16}, \dot{m}_{19}$), which provide thermal energy for the HP feedwater heaters (SPs 15, 16 and 19) and reheating, remain nearly constant with increasing F_C, even though the extraction enthalpies ($h_{15,16,19}$) increase to maintain an 88.4 °C increase in temperature across the deaerator and HP feedwater heaters. The outlet mass flow rate ($\dot{m}_3$) decreases with increasing F_C. The constant pressure at the inlet of the HPT results in an increase in the pressure (P_3) and enthalpy (h_3) at the outlet.

Figure 11 shows the effect of varying F_C on the power (solid line on left ordinate) and isentropic efficiency (dashed line on right ordinate). At the baseload condition, power is 374 MW and isentropic efficiency is 0.84. As F_C is increased, power and efficiency of the HPT decrease. At $F_C = 0.1$, $\dot{W} = 161$ MW and $\eta_T = 0.836$. At $F_C = 0.52$, $\dot{W} = 11$ MW and $\eta_T = 0.801$. The decrease in power is consistent with faster charging of the TES.

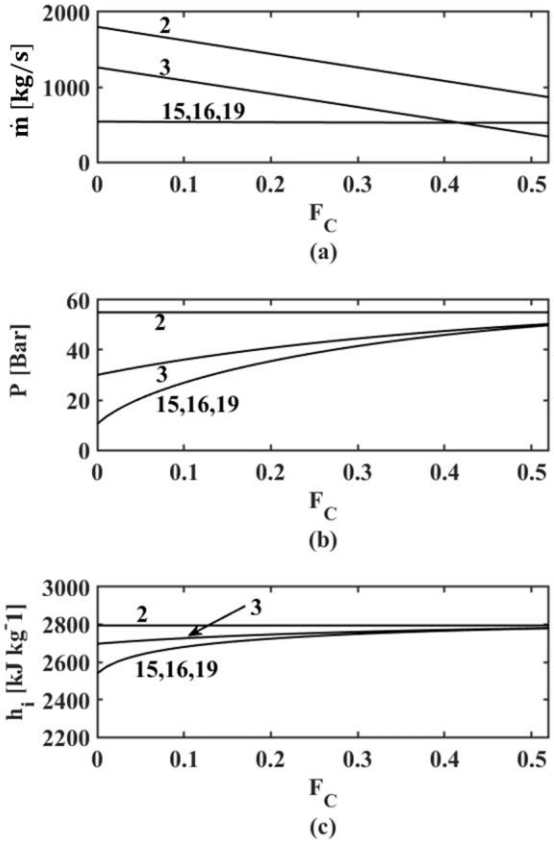

Fig. 10. State point values for the inlet, extraction point and outlet of the HPT during charging for $0 \leq F_C \leq 0.52$ and $\eta_{RT} = 1$: (a) mass flow rate, (b) pressure and (c) enthalpy. State points are indicated by the numerical values shown on Fig. 3.

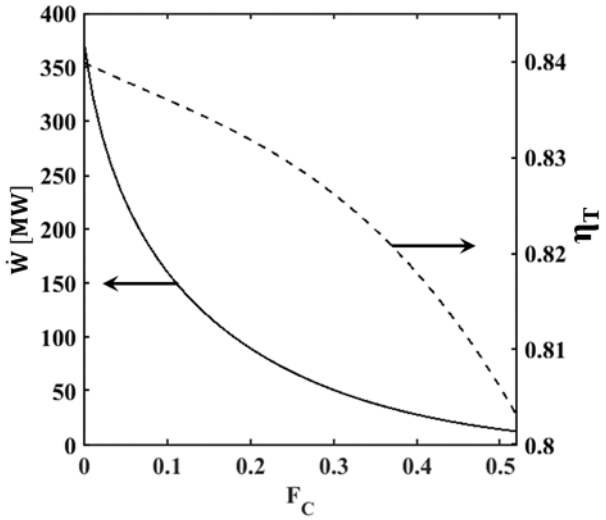

Fig. 11. Power output (solid line of left ordinate) and isentropic efficiency (dashed line on right ordinate) of the HPT during charging for $0 \leq F_C \leq 0.52$ and $\eta_{RT} = 1$.

Next consider the impact of varying charging mass fraction on the LP turbine shown in Fig. 12. Flow rates (a), pressures (b) and enthalpies (c) are plotted versus F_C in Fig. 12. The LPT inlet mass flow rate ($\dot{m}_4$) is 1200 kg/s at baseload condition $F_C = 0$. As more steam is diverted to the TES, the mass flow rate ($\dot{m}_4$) and pressure (P_4) decrease. The inlet enthalpy (h_4) increases because T_4 is held constant. A decrease in pressure at the inlet is required to maintain a constant pressure at the outlet of the LPT (P_5). The intermediate extraction mass flow rates ($\dot{m}_9$ - $\dot{m}_{12}$), which provide thermal energy for the LP feedwater heaters, increase slightly (<4%) with increasing F_C. The increase in extraction mass flow rates is necessitated by the decrease in specific enthalpies at the extraction points and the need to maintain a 94 °C increase in feedwater temperature. Consistent with the changes in inlet and extraction mass flow rates, the outlet mass flow rate ($\dot{m}_5$) decreases with increasing F_C. The enthalpy at the outlet (h_5) increases, consistent with an increased inlet enthalpy and reduced pressure drop across the turbine. Figure 13 shows power and isentropic efficiency versus F_C. At the baseload condition, power is 690 MW and isentropic efficiency is 0.835. At the maximum charging rate at $F_C = 0.52$ $\dot{W} = 80$ MW and $\eta_T = 0.73$. Over the range of charging mass flow rates considered, the decrease in power from the LPT (88%) is less than that of the HPT (97%). This difference is due to the requirement to hold the HPT inlet pressure constant to avoid changes in the steam generator with TES use.

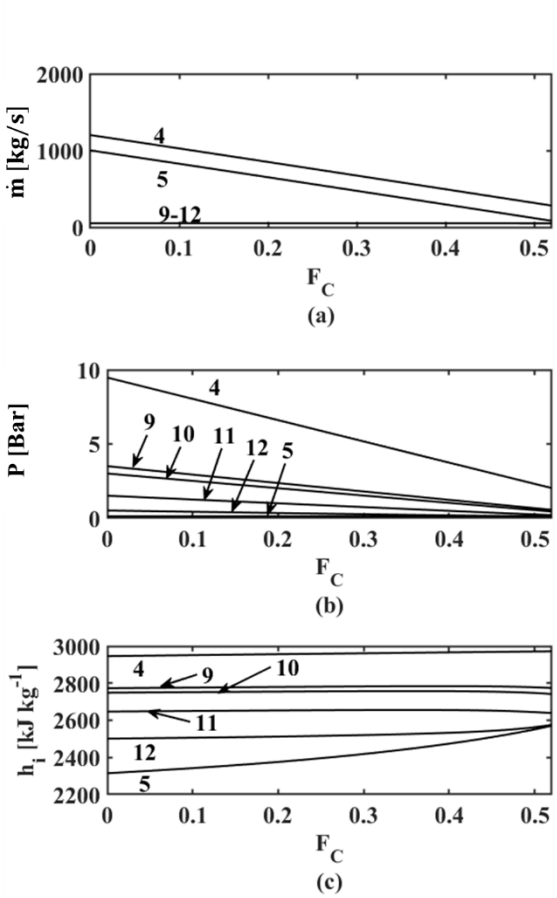

Fig. 12. State point values for the inlet, extraction point and outlet of the LPT during charging for $0 \leq F_C \leq 0.52$ and $\eta_{RT} = 1$: (a) mass flow rate, (b) pressure and (c) enthalpy.

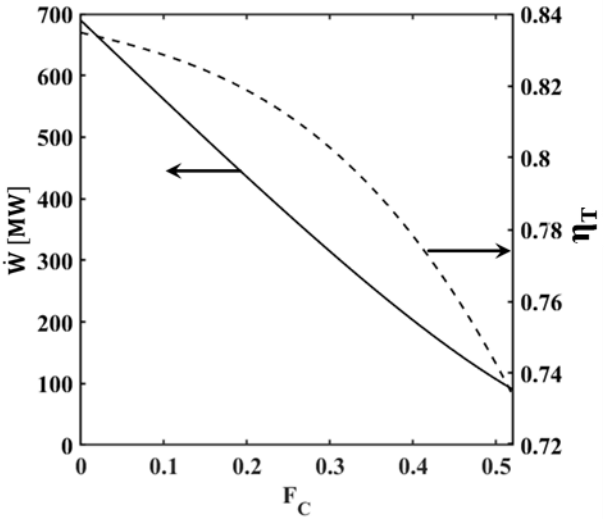

Fig. 13. Power output (solid line on left ordinate) and isentropic efficiency (dashed line on right ordinate) of the HPT during charging for $0 \leq F_C \leq 0.52$ and $\eta_{RT} = 1$.

2.4.2 Discharging

During discharge, the steam generated in the TES (SP 24) is combined with the mass flow rate from the moisture separator/reheater ($\dot{m}_4$) to increase power of the LPT. Figure 8 shows the mass flow rates (a), pressures (b), and enthalpies (c) for the LPT for $0 \leq F_D \leq 0.1$ and $\eta_{RT} = 1$. The mass flow rate ($\dot{m}_4$) and pressure (P_4) are 1200 kg/s and 9.5 Bar at baseload conditions, i.e. $F_D = 0$, and increase as the discharging mass fraction is increased. At $F_D = 0.1$, $\dot{m}_4 = 1380$ kg/s and $P_4 = 10.93$ Bar. For $0 \leq F_D \leq 0.1$, h_4 is reduced from 2974 kJ kg^{-1} to 2940 kJ kg^{-1}. The extraction specific enthalpies ($h_9 – h_{12}$) decrease with increasing F_D. The extraction mass flow rates ($\dot{m}_9 - \dot{m}_{12}$) are increased to maintain a 94 °C increase in water temperature across the low-pressure feedwater heaters. Consistent with the changes in the inlet, the outlet mass flow rate ($\dot{m}_5$) increases and the outlet enthalpy (h_5) decreases with increasing F_D.

Figure 15 shows the impact of varying turbine state points on the power and the isentropic efficiency. Power and efficiency increase from 690 MW and 0.835 at baseload conditions to 829 MW and 0.840 at $F_D = 0.1$. Isentropic efficiency of the LPT is highest at $F_D = 0.1$, which is the largest discharge mass fraction considered.

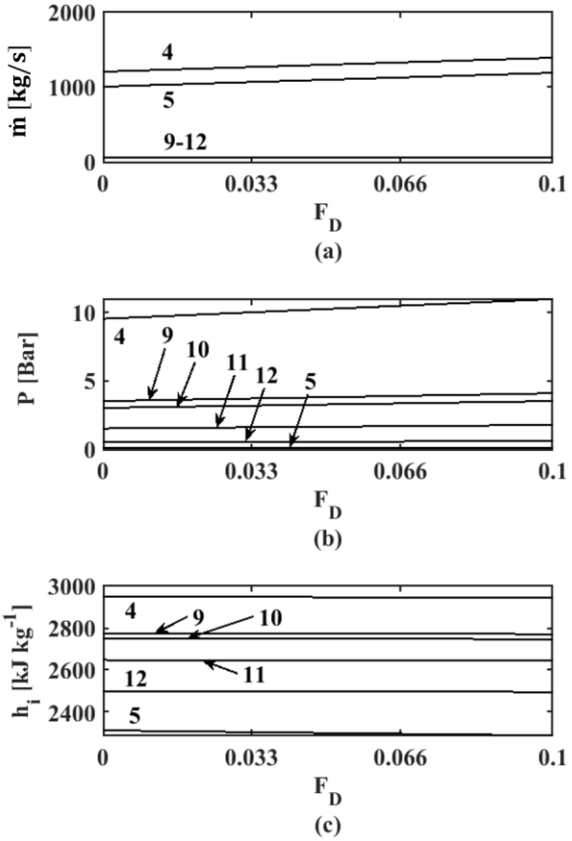

Fig. 14. State point values for the LPT during discharging for $0 \leq F_D \leq 0.1$ and $\eta_{RT} = 1$: (a) mass flow rates, (b) pressures and (c) enthalpies.

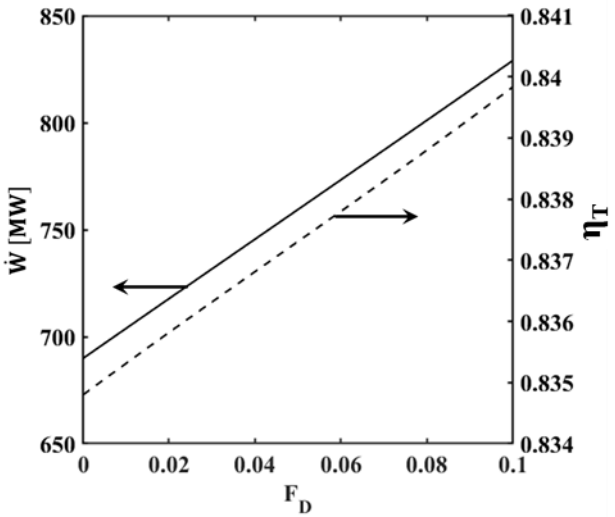

Fig. 15. Power output (solid line on left ordinate) and isentropic efficiency (dashed line on right ordinate) of the LPT during discharging for $0 \leq F_D \leq 0.1$ and $\eta_{RT} = 1$.

Variable operation of the LPT impacts the HPT. Figure 11 shows the mass flow rates (a), pressures (b) and enthalpies (c) of the HPT versus $F_{D.}$ These values are relatively level over the range of discharge flow rates considered. At F_D = 0.1, P_2 = 55.12 Bar, changing h_1 less than 0.1 kJ kg^{-1} compared to F_D= 0. The slight increases in pressure and enthalpy have negligible impact on steam generator and pump operation. Power and isentropic efficiency are plotted in Fig. 17 versus F_D. The decrease in HPT power from 374 MW at F_D = 0 to 351 MW at F_D = 0.1 is a result of the increased flow rate to the LPT and the resulting increased HPT exit pressure and enthalpy. Isentropic efficiency is constant at 0.84. During discharge, the decrease in HPT power during discharge is compensated for by the increase in LPT power. Discharging to the LPT is preferable to discharging to a secondary cycle.

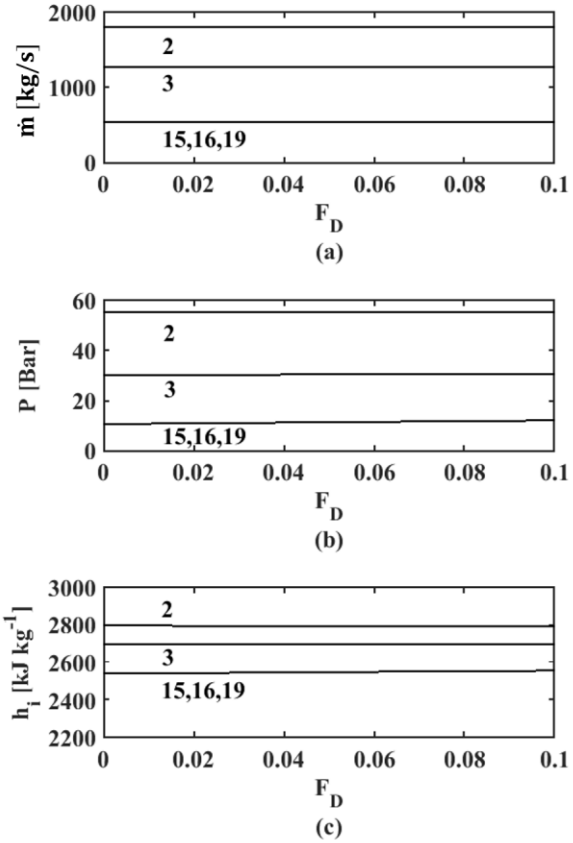

Fig. 16. State point values for the HPT during discharging for $0 \leq F_D \leq 0.1$ and $\eta_{RT} = 1$: (a) mass flow rates, (b) pressures and (c) enthalpies.

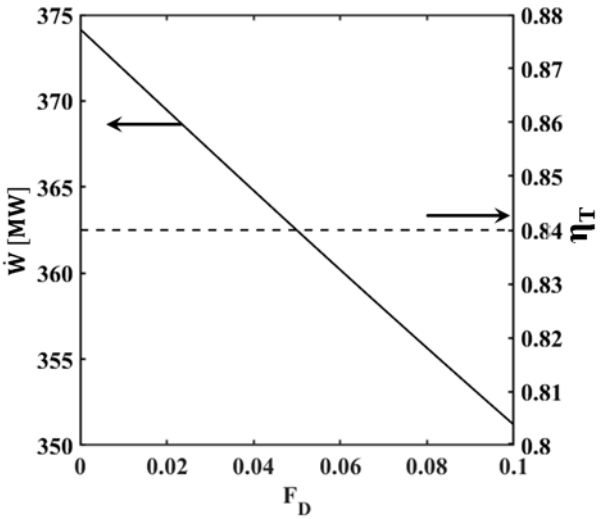

Fig. 17. Power output (solid line on left ordinate) and isentropic efficiency (dashed line on right ordinate) of the HPT during discharging for $0 \leq F_D \leq 0.1$ and $\eta_{RT} = 1$.

2.4.3 TES Cycle Performance

The use of TES increases the capacity factor of the plant over a charge/discharge cycle compared to the alternative of bypassing steam to the condenser. Figure 13 shows the capacity factor of the power plant during a charge/discharge cycle operated with TES (solid lines on left ordinate) versus F_C. At $F_C = 0$, there is no change from the baseload condition. The capacity factor decreases with increasing F_C, due to a decrease in power output from the HPT and LPT in partial loading. The capacity factor increases with increasing F_D. The impact of discharging mass fraction does not appear significant to the eye on this plot due to the large power plant capacity. To aid visualization of the results, the ratio of capacity factor with TES and that with steam bypass (CF_{TES}/CF_{BP}) is plotted on the right ordinate (dashed lines) for $F_D = 0.05$ and $F_D = 0.1$. For both $F_D = 0.1$ and $F_D = 0.05$, CF_{TES}/CF_{BP} increases with increasing charging fraction. At the maximum charge and discharge rates, TES improves the relative capacity factor by 9.8% compared to steam bypass. We note that the CF_{TES}/CF_{BP} in the present work is over a charge/discharge cycle. To evaluate an annual capacity factor, such as that presented by Denholm et al. [20], the cycle model would need to be considered within the context of a specific generation mix within an electrical grid. The annual capacity factor will depend on the frequency of charge/discharge cycles.

Figure 19 shows the relative capacity factor versus η_{RT} at $F_C = 0.52$ and $F_D = 0.1$ for $0.5 \leq \eta_{RT} \leq 1$. The relative capacity factor decreases nonlinearly with decreasing η_{RT}. At $\eta_{RT} = 0.75$, CF_{TES}/CF_{BP} is 1.095, a reduction of about 10% from $\eta_{RT} = 1$. At $\eta_{RT} = 0.5$, CF_{TES}/CF_{BP} is 1.088. In practice, η_{RT} has been shown to exceed 0.95 in commercial solar power plants [81].

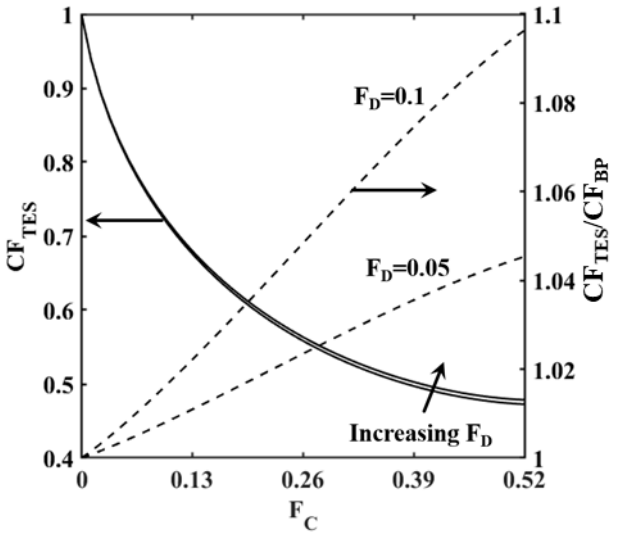

Fig. 18. Capacity factor for the AP1000 power plant with TES for $0 \leq F_C \leq 0.52$ and $\eta_{RT} = 1$ (solid lines on left ordinate) and relative improvement in capacity factor compared to bypass operation for $F_D = 0.05$ and $F_D = 0.1$ (dashed lines on right ordinate).

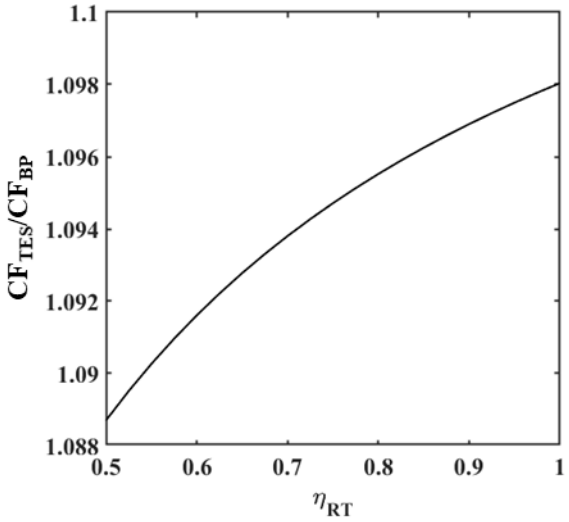

Fig. 19. CF_{TES}/CF_{BP} versus η_{RT} for $0.5 \leq \eta_{RT} \leq 1$ at $F_C = 0.52$ and $F_D = 0.1$.

Figure 20 shows the efficiency of conversion of stored thermal energy to electricity as a function of the discharging mass fraction for $\eta_{RT} = 1$. Approaching $F_D = 0$, $\eta_D = 0.223$ and $\eta_D = 0.230$ at $F_D = 0.1$. The value of η_D changes less than 3% with the 15% change in total mass flow rate though the LPT. Simple cycle combustion turbines operate at a higher thermal efficiency ($0.35 \leq \eta_{GT} \leq 0.45$) but generally have a larger variation in thermal

efficiency with change in power. Because the TES is discharged to the main LPT, loads below 30% (F_D=0.03) are possible, unlike stand-alone peaking cycles.

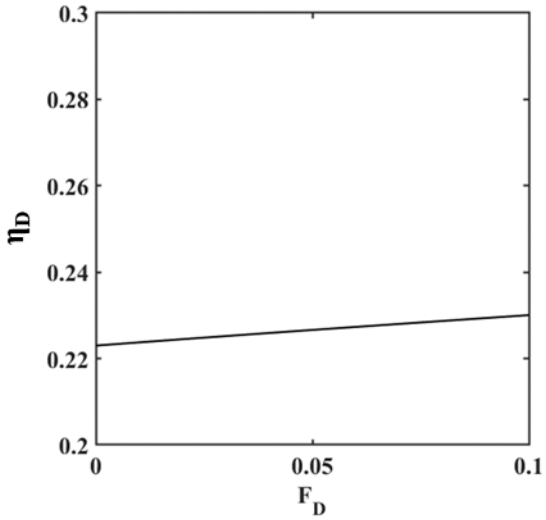

Fig. 20. Thermal to electrical efficiency of TES in a nuclear Rankine power cycle for η_{RT} = 1.

2.5 Conclusion

The use of TES in baseload power plants is one approach to achieve grid stability as variable renewable electrical generation becomes an increasingly larger fraction of total electrical capacity. In this study, the impact of using TES in the primary Rankine power cycle is characterized by a thermodynamic model based on a modern nuclear power plant. Comparison of the capacity factor over a charge/discharge cycle is compared to the capacity factor of the same plant using steam bypass (without storage). The capacity factor is as much as 9.8% higher with TES for operating conditions that only require modifications to the steam flow path and replacement of cycle components[3]. This benefit increases with increasing charge and discharge power and is based on an idealized TES with η_{RT} = 1. As shown, the relative capacity factor will be lower in actual systems with non-ideal behavior. The study provides the motivation to develop detailed designs and

[3] Change to publication

models of TES modules and storage materials for this application and to model their performance during real time operation within electrical grid systems. Moreover, it will be valuable to consider TES with other baseload power plants, such as coal and natural gas combined cycle. Higher operating temperatures in these power cycles may result in greater relative increases in capacity factor

3 On the Use of Thermal Energy Storage for Flexible Baseload Power Plants: Thermodynamic Analysis of Options for a Nuclear Rankine Cycle[4]

The intermittency of wind and solar electric generation can disrupt the dynamic balance utilities must maintain to meet fluctuating demand. The present work examines the use of thermal energy storage (TES) to increase the operational flexibility of a baseload power plant and thus incentivize renewable energy and decarbonize the grid. A first and second law thermodynamic model of a nuclear power plant establishes the impacts of TES on the capacity factor and thermal efficiency of the plant. Four storage options distinguished by the location within the cycle where steam is diverted for charging and whether discharge of the TES is via the primary or a secondary Rankine cycle are considered. TES is compared to steam bypass, which is an alternative to provide baseload flexibility. TES is significantly better than steam bypass. The storage option with the greatest thermodynamic benefit is charged by diverting superheated steam at the outlet of the moisture separator/reheater to the TES. The TES is discharged for peaking power through an optimized secondary cycle. TES increases the capacity factor as much as 15% compared to steam bypass at representative charging mass flow rates. The storage option that diverts steam from the steam generator to charge the TES and discharges the TES to the primary cycle extends the discharge power to a lower range and does not require a

[4] This chapter is based on the article F. Carlson and J. H. Davidson, "On the Use of Thermal Energy Storage for Flexible Baseload Power Plants: Thermodynamic Analysis of Options for a Nuclear Rankine Cycle," *J. Heat Transfer*, vol. 142, no. 5, May 2020, doi: 10.1115/1.4045230.

secondary cycle. In this case, the capacity factor and efficiency are as much as 8% greater than that of steam bypass.

3.1 Introduction

Deployment of variable renewable energy (VRE) sources, such as wind and solar, introduces temporal mismatches between the supply of electricity and consumer demand. Increasing the operational flexibility of conventional baseload power plants and energy storage are viewed as necessary to accommodate the growing use of VRE while maintaining reliable energy distribution [14], [18], [50], [54], [82]–[84]. There are a variety of energy storage options; the two most prevalent in reference to the expansion of VRE are batteries [10], [11], [13], [85] and thermal energy storage (TES) [76], [81], [86]–[88]. The cost of TES per kilowatt hour is projected to be an order of magnitude less than batteries [11]. Thermal energy storage has also been compared favorably to other methods for increasing grid flexibility including combustion turbines and pumped hydro energy storage [37], [38]. In the present work, we explore the use of TES to increase the flexibility of baseload nuclear power plants. We view this concept as one, but not the only, approach of increasing grid flexibility to accommodate VRE. Use of TES with nuclear power yields higher capacity factors than bypassing steam from turbines to the condenser (referred to as steam bypass), which is the only other proposed method of modulating power from existing steam power plants that are designed for fixed power.

The early work by Gilli et al. considered the economic benefits of TES to replace pumped hydro and combustion turbine peaking plants [37], [38]. They proposed using high pressure, superheated steam generated from a pressurized water nuclear reactor to charge steam accumulators that could be discharged to a secondary power cycle. More recently, TES has been proposed to modulate power from fixed output baseload power plants with

the intent to allow the expanded use of VRE and decarbonization of the grid [17], [20], [24], [25], [39], [41], [46], [89]. Forsberg and co-authors [17], [19], [24], [25], [39], [41] discuss the need for changing energy markets to enable integration of TES with nuclear power. They outline and discuss the impacts on energy storage of three market strategies: 1) a wholesale market in which the price of electricity fluctuates with supply and demand (the market that is used currently in the U.S.), 2) a capacity market in which value is placed on the capacity of the power plant, and 3) an ancillary services market in which secondary energy generation services are incentivized. Wholesale markets require high capacity factors for nuclear power plants to remain competitive [36]. Capacity and ancillary service markets benefit systems with storage; TES can provide additional capacity and would be implemented with the objective of providing frequency control and rapid response [19].

The high capital and low operating costs of nuclear power plants favor operating a plant at a high capacity factor [36]. Denholm et al. [20] studied the effects of TES storage capacity and power on the capacity factor of a nuclear power plant fleet supplying up to 30% of energy in a grid in which 60% of the energy is provided by VRE. Integration of the TES into the plants was assumed to have no impact on the efficiency of the baseload power plant. As shown by Carlson et al. [46], this assumption is a simplification. The predicted cost of electricity was as much as 45% lower with TES than with an unspecified load following capability in a wholesale market. Methods of load following for nuclear power plants include storage, steam bypass or building new, more flexible nuclear power plants [31], [90]. In steam bypass, steam is generated at a constant rate, temperature and pressure. To reduce load, steam is diverted from the turbines and the energy of the diverted steam is lost [59].

Carlson et al. [46] provide the first component-level thermodynamic model of a nuclear power plant with TES. In the prior study, the impact of TES on the operating state points and efficiency of a 1052 MW_e nuclear Rankine power cycle with TES integrated into the primary Rankine cycle is evaluated. Use of TES is compared to operation with steam bypass. In the storage option considered, a fraction of high-pressure steam from the steam generator bypasses the high-pressure turbine (HPT) and low-pressure turbine (LPT) to charge the TES. During discharge, steam generated in the TES is combined with the steam mass flow rate from the moisture separator/reheater (MSR) to increase power of the LPT by 119 MW. The most significant change to the plant efficiency is during charging; the isentropic efficiency, pressure drop and power of the turbines decrease with increasing diversion of steam. TES is always preferable to operating the same plant with steam bypass, which also reduces the efficiency of the power plant during charging without the benefit of energy storage for peaking power. The capacity factor of a plant with TES over a single charge/discharge cycle is predicted to increase by as much as 10% over steam bypass operation. Charging and discharging the TES within the primary cycle avoids procurement of a secondary power cycle for discharge.

The present study considers a secondary cycle for discharging the TES. Discharge to a secondary cycle rather than to the primary cycle has a number of potential benefits. It provides more flexibility for the location where steam is diverted to charge the TES. It has the potential for higher thermal efficiency during discharge. It eliminates the need to redesign the LPT to handle higher mass flow rates of steam during discharge. Three potential storage options are evaluated: I) steam diversion at the outlet of the steam generator, II) steam diversion at the outlet of the HPT, and III) steam diversion at the outlet

of the MSR. First and second law thermodynamic models yield an optimum discharge temperature and pressure for each option and state points for the primary and secondary power cycles for a range of charging and discharging mass flow rates. The capacity factor and efficiency for the three options with discharge to a secondary cycle are compared to the storage option explored in the prior work and to steam bypass without TES. The results are interpreted to recommend a preferred configuration for operating a nuclear power plant with TES.

3.2 Power Plant Operation

The Westinghouse AP1000 was selected for analysis because it is representative of a modern nuclear power plant and operating characteristics are available [29], [61]. A flow diagram of the AP1000 power plant is shown in Fig. 21. Operation of the baseload power plant is indicated by solid lines. Bypass operation is indicated by dot-dash lines. The four options compared in the present study are denoted by Roman numeral and dashed lines. The secondary power cycle is indicated by dotted lines. Detailed operation of baseload, steam bypass, and the option of charging and discharging within the primary cycle (referred to as option IV) are provided in our prior work [46]. Here we summarize this option to aid understanding of the four options we compare.

3.2.1 Baseload Operation

Baseload operation of the primary power plant is described in detail in references [29], [46]. Steam exits the steam generator at 271°C and 55 Bar at 1886 kg s^{-1} (indicated by state point, SP 1). Ninety five percent of the steam mass flow rate (SP 2) is to the HPT and the remainder (SP 1a) is diverted to reheat the steam exiting the HPT. Steam entering the HPT (SP 2) is expanded to 10.5 Bar and a quality of 0.88 (SP 3). Intermediate steam extractions (SPs 15 and 16) from the HPT provide thermal energy for the high-pressure

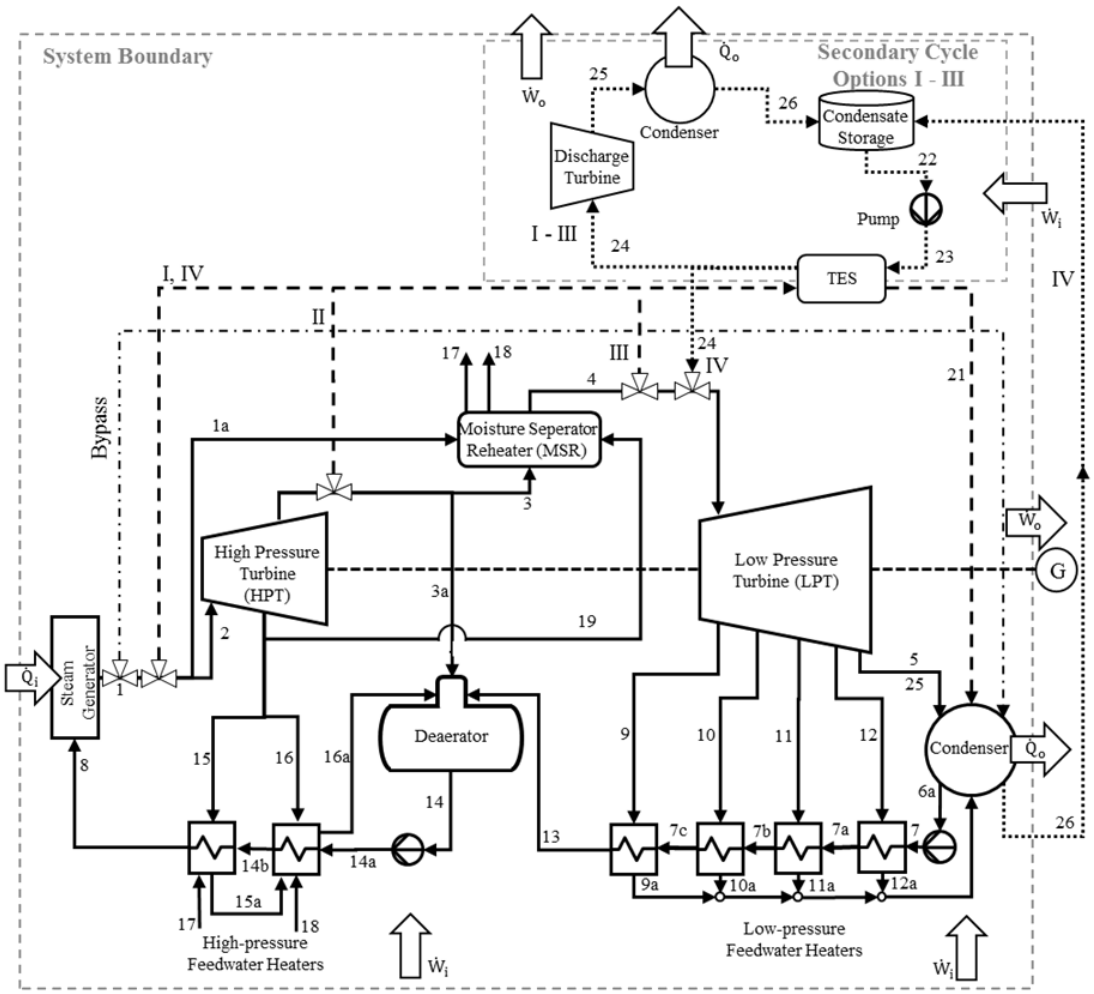

Fig. 21. Diagram of the AP1000 nuclear power plant showing baseload operation, bypass and four TES options. Baseload operation is indicated by solid lines. Steam bypass is indicated by the dotted-dashed line. The four options for diversion of steam from the primary power cycle to charge the TES (dashed lines) are: (I and IV) diversion of steam at the outlet of the steam generator, (II) diversion of steam at the outlet of the HPT and (III) diversion of steam at the outlet of the moisture separator/reheater to the TES. Discharge of the TES through the secondary power cycle (options I – III) and discharge to the primary cycle (IV) are indicated by dotted lines. State points are indicated by number.

feedwater heating system and for steam reheating (SP 19). Before entering the low-pressure turbine (LPT), the steam is reheated to 9.5 Bar and 251°C (SP 4). The LPT expands the steam to 0.1 Bar and a quality of 0.89 (SP 5). Four steam extractions (SPs 9 – 12) provide energy for the low-pressure feedwater heating system. Steam exiting the LPT is cooled to slightly below saturation (SP 6a) and then pressurized (SP 7) and heated to 30 Bar and 138°C (SP 13). In the deaerator (SP 14), oxygen is removed from the condensate and the

condensate is heated using steam diverted from the HPT exhaust (SP 3a). The AP1000 has a net baseload power output of 1052 MW_e and thermal efficiency of 0.31.

3.2.2 Charging the TES

When VRE generation is high, nuclear power to the electrical grid is reduced by diverting a fraction of steam from the main power cycle. The diverted steam charges the TES. The stored energy can be used when peaking power is required. The charging mass fraction (F_C) is the ratio of steam diverted ($\dot{m}_{21}$) to the TES and the total mass flow rate exiting the steam generator ($\dot{m}_1$).

$$F_C = \frac{\dot{m}_{21}}{\dot{m}_1} \tag{22}$$

In the present study, the charging fraction is parameterized over $0 \leq F_C \leq 0.46$. A value of zero represents baseload operation. The diverted steam flow rate cannot exceed 46% of the baseload steam mass flow rate because in that case, the mass flow rate through the LPT would be less than 30% of the design flow rate. Thirty percent of the design condition is the lower limit of empirical data for isentropic turbine efficiency[64].

The four options are shown in Fig. 21. For options I and IV, steam is diverted to the TES at the outlet of the steam generator. This approach provides the highest temperature (271°C) and pressure (55 Bar) steam for charging. For Option II, steam is diverted at the outlet of the HPT. The charging temperature and pressure for option II are 182°C and 10.5 Bar. Exiting the HPT, the steam is a mixed phase with a quality of 0.88. Option III is the only option that uses superheated steam for charging. Steam is diverted at the outlet of the MSR to the TES. The charging temperature and pressure are 251°C and 9.5 Bar. For options I, II and IV the flow of steam through the MSR decreases with increasing charging fraction. Steam for reheating is taken from the high-pressure steam

supply (SP 1a) and from the HPT extraction point (SP 19). Therefore, $\dot{m}_{1a}$ and $\dot{m}_{19}$ are reduced accordingly. Instead of being diverted to the MSR, the steam is expanded in the HPT. For option II, the diversion of steam for charging is after the HPT. Because $\dot{m}_{1a}$ and $\dot{m}_{19}$ are reduced, the mass flow rate through the HPT exceeds the baseload mass flow rate. Therefore, the HPT is modified to accommodate higher steam flow rates. For option IV, steam generated at discharge is combined with the baseload mass flow rate entering the LPT, requiring modification of the LPT to accommodate the higher steam flow rate. These modifications could be accomplished by changes in the flow path. Alteration of the turbine to accommodate additional steam during either charging or discharging impacts the performance of the plant because at baseload the turbine operates at less than the maximum flow rate and efficiency. Table 6 lists the temperatures, pressures and quality of the steam at the inlet of the TES during charging for each option.

Table 6. Temperature, pressure and quality of diverted steam for charging.

	Option I	**Option II**	**Option III**	**Option IV**
T [°C]	271	182	251	271
P [Bar]	55	10.5	9.5	55
χ [-]	1	0.88	-	1

3.2.3 Discharging the TES

When VRE output is reduced and peaking power is required, the TES is discharged. During discharge, water at ambient (1 Bar and 25°C (SP 22)) is pressurized to the turbine inlet pressure and passes through the TES (SP 23). In the TES, the water is heated and exits as steam at P_{24} and T_{24}. For options I, II, and III, the temperature (T_{24}) and pressure (P_{24}) at the inlet of the turbine are parameterized in the model. Steam is expanded to 0.1 Bar (SP 25). Water exits the condenser and is stored at ambient. The discharging mass fraction

(F_D) is the ratio of the mass flow rate of steam exiting the TES and the mass flow rate generated by the TES at the design condition (subscript *ref*).

$$F_D = \frac{\dot{m}_{24}}{\dot{m}_{24,ref}} \tag{23}$$

The design condition generates the highest power of the turbine. The discharging mass fraction is parameterized. For option IV, the steam is combined with the steam exiting the MSR and expanded in the LPT of the primary cycle, increasing the power of the power plant 119 MW compared to baseload [46].

3.2.3.1 Conceptual TES Design

We provide a conceptual design for a multistage TES to illustrate a potential approach. The concept previously presented by Carlson et al. [46] for option IV is updated to include charge/discharge options I, II, and III. The multistage concept is based on one developed for direct steam generating solar thermal power plants [91]. As illustrated in Fig. 22, stages are designated for condensate preheating (stage A), evaporation (stage B) and steam superheating (stage C). During discharge, water enters stage A at the discharge pressure (P_{24}) and ambient temperature (a small amount of heating occurs due to inefficiencies of the pump). The exit of stage A is at saturation ($\chi = 0$). In stage B, the quality of the steam is increased to $\chi = 1$. In stage C, the saturated vapor is superheated to the turbine inlet temperature (T_{24}). The ranges of temperature and pressure depend on the storage option. The temperature and pressure of steam discharged from the TES are lower than that for charging in accordance with the second law of thermodynamics. During charging, the temperature and pressure of the steam entering the TES are fixed and heat is rejected isobarically. At discharge, we impose limits on the temperature and pressure of steam as discussed in section 3.3.1. The resulting ranges of discharging temperature and

pressure are given in Table 7. Option I has the highest possible discharge temperature and pressure at 251°C and 40.4 Bar. Options II and III have significantly lower maximum discharging pressures of 6.5 and 5.8 Bar, respectively. Options II and III are limited to 162°C and 231°C. The temperature and pressure for option IV are 251°C and 10.9 Bar set by the inlet conditions for the LPT.

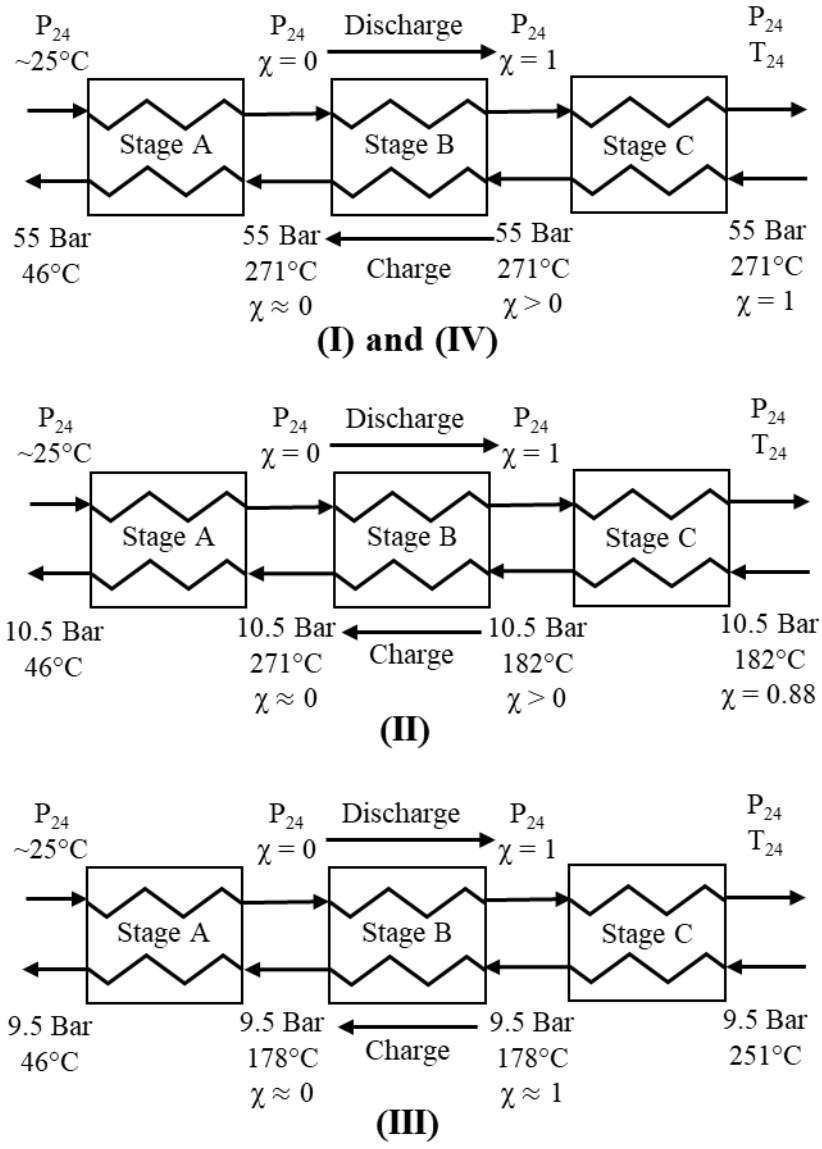

Fig. 22. Three-stage conceptual TES system showing approximate stage inlet and outlet temperatures for options I and IV (top), II (middle) and III (bottom).

Table 7: Temperature and pressure parameters for TES discharging.

Option	Parameters TES outlet temperature (T_{24}) [°C]	TES outlet pressure (P_{24}) [Bar]
I	120 – 251	2 – 40.4
II	120 – 162	2 – 6.5
III	120 – 231	2 – 5.8
IV	251	10.9

During charging, steam enters stage C at the temperature, pressure and quality for each option as listed in Table 6. The flow of steam is in the opposite direction to that during discharging (i.e. counterflow). In options I, II, and IV, the charging steam is not superheated. The steam condenses across stages C and B and enters stage A at $\chi = 0$. In stage A, the water is cooled, exiting at 46°C. In option III, steam enters stage C as a superheated vapor. The steam exits stage C at $\chi \approx 1$. In stage B, the steam condenses and exits at $\chi = 0$. In stage A, the water is cooled, exiting at 46°C.

3.3 Modelling Approach

3.3.1 Overview

The primary objective of the model is to quantify the effects of s option on five key metrics: discharge efficiency (Eq. (24)), TES exergetic efficiency (Eq. (25)), capacity factor (Eq.(26)), thermal efficiency (Eq. (27)), and relative capacity factor and thermal efficiency thermal normalized by the values for steam bypass for a charge/discharge cycle (Eq. (28)).

$$\eta_D = \frac{t_D\left(\dot{W}_D - \dot{W}_{X,BL}\right)}{Q_{TES,C}} \tag{24}$$

$$\epsilon_{TES} = \frac{\dot{E}x}{\left(1 - \frac{T_0}{T_{TES}}\right)\dot{Q}_{TES}} \tag{25}$$

$$CF = \frac{CF_{TES}}{CF_{X,BL}} = \frac{\dot{W}_C t_C + \dot{W}_D t_D}{\dot{W}_{X,BL}(t_C + t_D)} \quad (26)$$

$$\eta_{PP} = \frac{\eta_{TES}}{\eta_{X,BL}} = \frac{\dot{W}_C t_C + \dot{W}_D t_D}{\dot{Q}_i(t_C + t_D)} \quad (27)$$

$$\frac{CF}{CF_{BP}} = \frac{\eta_{PP}}{\eta_{BP}} = \frac{\dot{W}_C t_C + \dot{W}_D t_D}{\dot{W}_{BP} t_C + \dot{W}_{X,BL} t_D} \quad (28)$$

The discharge efficiency (η_D) is the efficiency of stored thermal energy to turbine work. The exergetic efficiency (ε_{TES}) is the comparison of the total change in exergy of the water/steam through the TES to the process if it were reversible. The form shown in Eq. (25) is derived from a steady state exergy rate balance (Eq. (29)) performed on the steam side of the TES.

$$0 = \sum \left(1 - \frac{T_0}{T_{TES}}\right) \dot{Q}_{TES} - \dot{W}_{CV} + \dot{E}x - \dot{E}x_{des} \quad (29)$$

The rate of exergy transferred into the control volume ($\sum(1 - T_0/T_{TES})\dot{Q}_{TES}$) balances the net rate of exergy entering the control volume ($\dot{E}x$) and the rate of exergy destruction ($\dot{E}x_{des}$). In this study, $\dot{Q}_{TES}$ is the net change in enthalpy of the mass flow rate through the TES and T_{TES} is the temperature of the TES. The temperature of the TES equal to the maximum thermodynamic average temperature.

$$T_{TES} = \frac{h_{in,TES} - h_{21}}{s_{in,TES} - s_{21}} \quad (30)$$

The subscript *'i,TES'* refers to state point for steam entering the TES, which depends on the storage option. The reference temperature (T_0) is 298 K. The capacity factor is the ratio of the sum of energy generated over a charge ($\dot{W}_C t_C$) and discharge ($\dot{W}_D t_D$) cycle and the energy that could have been produced by the baseload power plant over the same duration ($\dot{W}_{X,BL}(t_C + t_D)$). The thermal efficiency is the ratio of electric energy generated and heat input over a charge/discharge cycle.

The following assumptions are applied to the TES.

1) The TES is modeled as a black box (i.e. it is modeled in terms of inputs and outputs without consideration of internal heat and mass transfer).
2) The storage capacity ($Q_{TES,C}$) is that required to produce a 119 MW increase in power over a four-hour discharge compared to baseload operation.
    a. The power output of the of 119 MW is set by the highest mass flow rate of the LPT for option IV [46]. Although the secondary cycle could have a higher discharge power, an increase in power of 119 MW at discharge provides a direct comparison to option IV.
    b. The duration of the discharge is specified based on consumer demand predictions by the California Independent System Operator (CAISO). CAISO predicts duration of peak energy demand (times for TES discharge) will be 4 – 5 hours for most of the year increasing up to 9 hours in summer [49].
3) Charging and discharging are steady, isobaric processes.
4) At discharge, the outlet temperature of the TES, T_{24}, is constrained to:

$$T_{sat@2\ Bar} \leq T_{24} \leq T_{in,TES} \tag{31}$$

The upper temperature limit is 20°C less than the temperature of the inlet to the TES, consistent with the temperature difference between the cold and hot streams in industrial steam generators [92]. The lower limit is the saturation temperature at 2 Bar, typically the lowest pressure for steam Rankine cycles [93].

5) At discharge, the steam pressure depends on the charging location and is related to the upper limit on temperature given in Eq. (31) by the Antoine equation [94]:

$$\log_{10}(2) \leq \log_{10}(P_{24}) \leq A + \frac{B^2}{-A + B(C + 20) + \log_{10}(P_{in,TES})} \tag{32}$$

where A, B and C are for water (A = 3.55959, B = 643.748, C = -198.043).

6) During charging, the temperature of water exiting the TES is 46°C, equal to the condenser temperature.

The following assumptions are applied in the analysis of the primary and secondary cycles. The 'design condition' refers to the highest power for the cycle.

7) Thermal input to the steam generator ($\dot{Q}_{SG}$) is 3431 MW_{th}.
8) Thermal losses, and potential and kinetic effects are neglected, as is typical in power plant system analyses [95].
9) The isentropic efficiency of the turbines is 0.84 at the design condition [29]. At off design conditions ($\dot{m} < \dot{m}_{ref}$), the isentropic efficiency of the turbines follows a curve fit of data for a condensing steam turbine [64].
10) Pump isentropic efficiency is 0.82 [29].
11) The lower limit of the mass flow rate of steam through the turbines is 30% of the mass flow rate at the design condition consistent with empirical data for isentropic turbine efficiency [64].
12) The quality of steam exiting the turbine must be greater than 0.88 to avoid erosion of the turbine blades.
13) Steam throttling is isenthalpic.
14) Enthalpies of steam exiting the MSR, feedwater heaters and deaerator are held at the baseload values.
15) The condenser pressure and temperature for both the primary and secondary cycles are 0.1 Bar and 46°C.
16) Water enters the secondary cycle at ambient (1 Bar, 25°C). After exiting the condenser, it is returned to condensate storage and held at ambient.

The ranges of charging and discharging mass fractions are limited by assumption 11 for the primary and secondary cycles. For options I – IV, charging mass fractions are varied over $0 \leq F_C \leq 0.46$. For discharging mass fractions, options I – III are varied over $0.3 \leq F_D \leq 1$. For option IV the discharging mass fraction is varied over $0 \leq F_D \leq 1$. The lower limit on the discharging fraction for option IV can approach zero because the flow rate to the LPT never reaches the limit set by empirical data (see assumption 11). The TES

outlet temperatures and pressures are selected using TES assumptions 4 and 5, respectively and are listed in Table 7.

3.3.2 Modeling Procedure

3.3.2.1 Discharging

Figure 23 is a flow chart of the model of discharging operation. The model yields values of discharge time (t_D), secondary cycle power ($\dot{W}_D$), discharge efficiency (η_D), TES exergetic efficiency (ε_{TES}) and storage capacity ($Q_{TES,C}$) as functions of TES outlet temperature (T_{24}), pressure (P_{24}) for options I – III and discharging mass fraction F_D. The TES outlet pressure (P_{24}) and temperature (T_{24}) are initialized to 2 Bar and 120°C. Beginning with $F_D = 1$ (power of 119 MW), an energy balance is performed on the discharging process (Eqs. (34) – (42)) yielding $Q_{TES,C}$ for the selected T_{24} and P_{24}. In option IV, the temperature and pressure are set at a single value by the operating conditions of the AP1000. If the turbine exit quality (χ_{25}) is less than 0.88, the temperature/pressure combination is eliminated from consideration. If $\chi_{25} > 0.88$, an exergy balance is performed (Eq. (44)). Based on assumptions 1 and 3 for the TES, the exergetic efficiency is only a function of T_{24} and P_{24}. F_D is decreased in increments of 0.005. For $F_D < 1$, an energy balance is performed using Eqs. (34) – (37) and (40) – (43). For a given P_{24}, the temperature is incremented as

$$dT = \frac{T_{max} - T_{sat}}{249} \tag{33}$$

where T_{sat} is the saturation temperature and T_{max} is the highest temperature for each option as listed in Table 7. This analysis is performed for 2 Bar $\leq P_{24} \leq P_{max}$ in increments of 0.1 where P_{max} is the high pressure listed in Table 7.

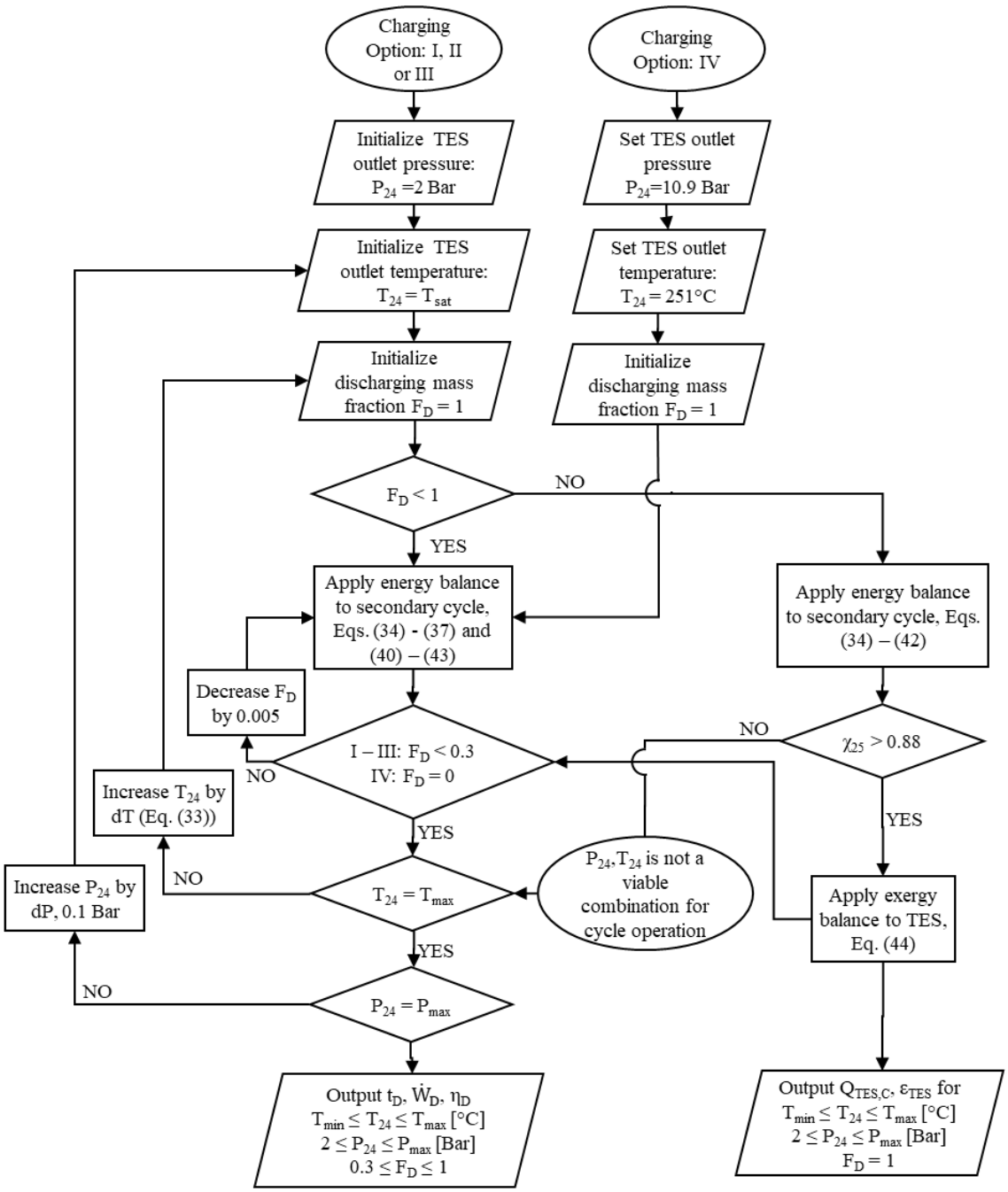

Fig. 23. Flow diagram for analysis of the discharging power cycle.

3.3.2.2 Primary Cycle/Charging

Figure 24 shows the procedure for modeling charging. The model yields values of charge time (t_C) and primary cycle power during charging ($\dot{W}_C$) as functions of the charging mass fraction (F_C). The discharging temperature (T_{24}) and pressure (P_{24}) and $Q_{TES,C}$ are

specified based on the results of the discharging model. The charging fraction (F_C) is initialized to zero for baseload operation. An energy balance is performed on the primary cycle (Eqs. (34) – (37), (40) and (45) – (48)) yielding t_C and $\dot{W}_C$. The charging fraction is increased in increments of 0.005 for $0 \leq F_C \leq 0.46$. Integrating over a cycle of charge and discharge, the capacity factors and thermal efficiencies are calculated using Eqs. (26) – (28).

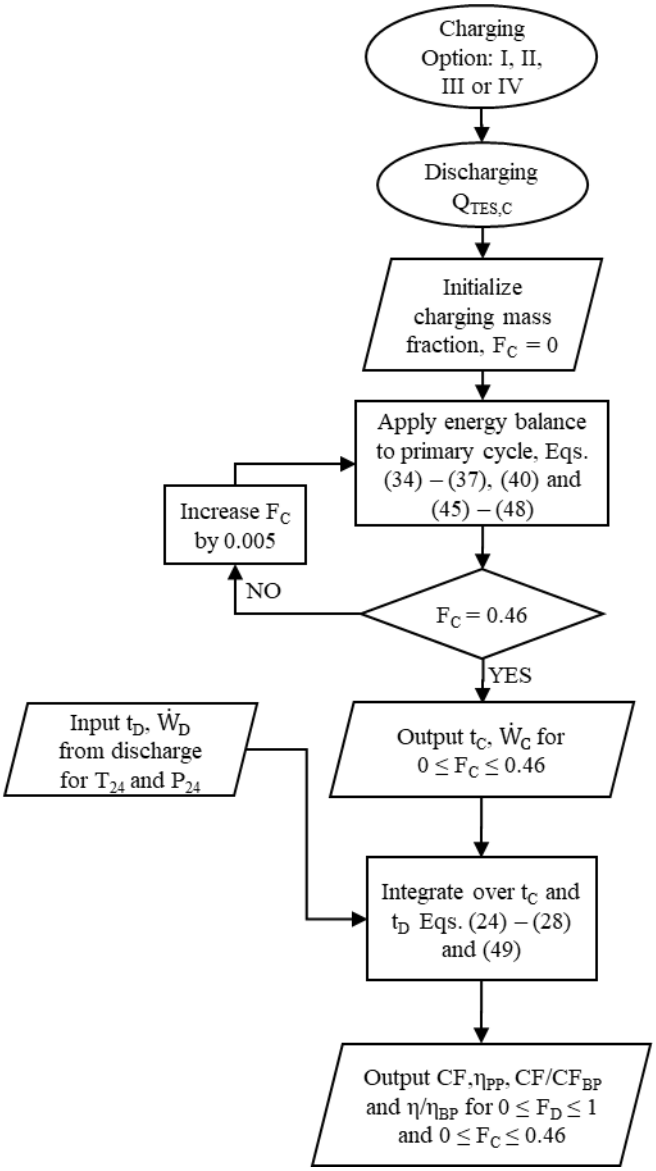

Fig. 24. Flow diagram for analysis of the primary cycle.

3.3.3 Governing Equations

This section provides equations for calculating the design condition for the secondary cycle and equations for adjusting the state point enthalpies with varying charging and discharging mass fractions. The model is executed in Matlab with thermodynamic properties evaluated using XSteam [96].

3.3.3.1 Secondary Cycle

The enthalpy at the exit of the pump is calculated using the isentropic efficiency of the pump.

$$\eta_P = \frac{h_{out,ise} - h_{in}}{h_{out} - h_{in}} \tag{34}$$

where the outlet pressure is P_{24} and the thermodynamic state at the inlet is known. The inlet pressure to the secondary cycle turbine is throttled to the pressure determined from Stodola's Ellipse [79] to maintain a constant turbine outlet pressure (P_{25}).

$$\left(\frac{\dot{m}}{\dot{m}_{ref}}\right)^2 = \frac{(P_{in} - P_{out})^2}{P_{in,ref}^2 - P_{out,ref}^2} \tag{35}$$

The subscript 'ref' refers to the design condition. The enthalpy at the outlet of the turbine is calculated based on the isentropic efficiency of the turbine.

$$\eta_T = \frac{h_{in} - h_{out}}{h_{in} - h_{out,ise}} \tag{36}$$

The isentropic efficiency of the turbine increases with increasing mass flow rate [64].

$$\eta_T = \eta_{T,BL} - \left(-0.22\left(\frac{\dot{m}}{\dot{m}_{ref}}\right)^3 + 0.62\left(\frac{\dot{m}}{\dot{m}_{ref}}\right)^2 - 0.62\left(\frac{\dot{m}}{\dot{m}_{ref}}\right) + 0.22\right) \tag{37}$$

At F_D = 1, the design mass flow rate (Eq. (38)) and associated total heat stored are calculated (Eq. (39)).

$$\dot{m}_{24,max} = \frac{\dot{W}_{D,max} - \dot{W}_{X,BL}}{((h_{24} - h_{25}) - (h_{23} - h_{22}))} \tag{38}$$

$$Q_{TES,C} = \dot{m}_{24,max} t_D (h_{24} - h_{23}) \tag{39}$$

For $F_D < 1$, the net work ($\dot{W}_D$) and discharge efficiency (η_D) are based on a component by component energy balance with adjustments made to the design condition state points using Eqs. (34) – (37). Neglecting the potential and kinetic effects, the general energy balance is

$$\dot{W} - \dot{Q} = \sum_{CV} \dot{m} h \tag{40}$$

The net work at discharge and the discharge efficiency are

$$\dot{W}_D = \dot{m}_{24,max} F_D \big((h_{24} - h_{25}) - (h_{23} - h_{22})\big) + \dot{W}_{BL} \tag{41}$$

$$\eta_D = \frac{(h_{24} - h_{25}) - (h_{23} - h_{22})}{(h_{24} - h_{23})} \tag{42}$$

where $\dot{W}_{BL}$ is the work produced by the primary cycle at $F_C = 0$. The total discharging duration when $F_D < 1$, t_D, is determined by Eq. (43).

$$t_D = \frac{Q_{TES,C}}{\dot{m}_{24,max} F_D (h_{24} - h_{23})} \tag{43}$$

Substitution of Eq. (40) and state points into Eq. (25) yields the exergetic efficiency of the TES.

$$\epsilon_{TES} = \frac{[(h_{24} - h_{23}) + T_0 (s_{23} - s_{24})]}{\left(1 - \frac{T_0 \big(s_{in,C} - s_{21}\big)}{h_{in,C} - h_{21}}\right)(h_{24} - h_{23})} \tag{44}$$

3.3.3.2 Primary Cycle

Carlson et al. [46] provide a detailed description of the model of the primary cycle which yields the power work during charging ($\dot{W}_C$), the capacity factors for option IV and steam bypass. The governing equations of the state points are the same as the secondary

cycle. The pumps in the primary cycle are governed by Eq. (34) and the turbines by Eqs. (35) – (37). For options II and IV, which require modifications to the HPT and LPT, respectively, the reference mass flow rates in Eqs. (35) and (37) are the modified rates.

In the primary cycle, the mass flow rates for the feedwater heaters and deaerator are set to maintain the same enthalpy rise as in baseload operation. The energy balance for the MSR given by Eq. (45) requires an iterative solution.

$$\dot{m}_3(h_4 - h_3) = \dot{m}_{19}(h_{19} - h_{18}) + \dot{m}_{1a}(h_{1a} - h_{17}) + \Delta\dot{E} \tag{45}$$

The enthalpies h_{1a}, h_4, h_{17} and h_{18} are fixed at the baseload values. The mass flow rate of the steam ($\dot{m}_3$) at the inlet of the MSR is

$$\dot{m}_3 = \dot{m}_2 - \dot{m}_{1a} - \dot{m}_{15} - \dot{m}_{16} - \dot{m}_{3a} - \dot{m}_{19} \tag{46}$$

The mass flow rates $\dot{m}_{1a}$ and $\dot{m}_{19}$ are assumed to be reduced in the same proportion to the baseload values.

$$\frac{\dot{m}_{1a}}{\dot{m}_{1a,X,BL}} = \frac{\dot{m}_{19}}{\dot{m}_{19,X,BL}} \tag{47}$$

The criteria for the solution is $\Delta\dot{E} < 10$ kW or 0.001% of the total power produced.

The charging duration (t_C) is determined by Eq. (48).

$$t_C = \frac{Q_{TES,C}}{\dot{m}_1 F_C (h_{in,C} - h_{21})} \tag{48}$$

Using Eqs. (34) – (48), the capacity factor of the system for a full cycle of charge and discharge is calculated (Eq. (26)) and compared to the capacity factor using steam bypass. The capacity factor during steam bypass is calculated using Eq. (49).

$$CF_{BP} = \frac{(\dot{W}_{C,I} t_c + \dot{W}_{BL} t_D)}{\dot{W}_{BL}(t_C + t_D)} \tag{49}$$

3.4 Results

3.4.1 Selection of Storage Capacity

In this section, we discuss the results of the parametric study of temperature/pressure during discharge of the TES for $F_D = 1$. The temperature/pressure combination that yields the highest discharge efficiency (η_D) and exergetic efficiency (ε_{TES}) is identified for TES options I-III and is referred to as the design condition. The storage capacity ($Q_{TES,C}$) is determined at the design condition to produce 119 MW for four hours.

Higher TES outlet temperature and pressure provide higher discharge and exergetic efficiencies, but the constraints on exit quality and temperature limit the operating range for options I and II. Figure 25 shows the discharge efficiency of the TES as a function of the TES outlet temperature (T_{24}) and pressure (P_{24}). Solid lines are isobars with the saturation temperature at the far left of the curves. Vertical dashed lines represent the temperature limits imposed by TES assumption 4. Horizontal dashed lines represent the pressure limit imposed by TES assumption 5. The region for option I, shaded in light grey, has an upper limit of 11.4 Bar and 251°C corresponding to a discharge efficiency of 0.23. The region for option I extends over the operating regions for options III and II. The region for option III, shaded in medium grey, has an upper limit of 5.8 Bar and of 231°C corresponding to a discharge efficiency of 0.20. The region for option III extends over the region of option II. Option II, indicated by dark grey, has the most restricted range of temperatures and pressures and lowest discharge efficiency. The upper limit is 4.14 Bar and 162 °C corresponding to a discharge efficiency of 0.18.

The TES outlet temperature (251°C) and pressure (10.9 Bar) for option IV corresponds to $\eta_D = 0.23$. The presence of extraction points in the LPT increases the

discharge efficiency marginally compared to option I, which is charged identically but is discharged to the secondary cycle turbine.

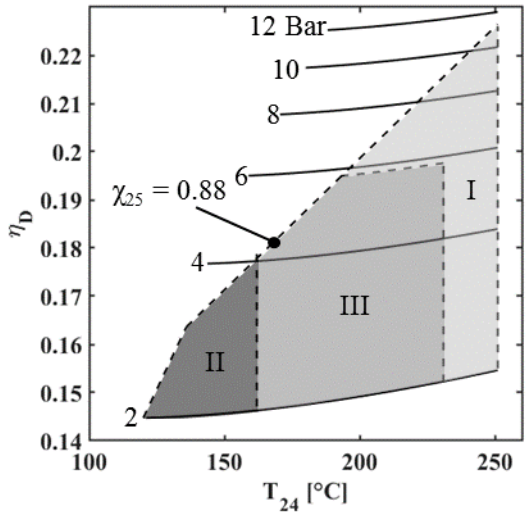

Fig. 25. Discharge efficiency of the secondary cycle (η_D) as a function of the TES outlet pressure (P_{24}) and temperature (T_{24}) for option I (light grey), II (dark grey) and III (grey) for $F_D = 1$.

Figure 26(a)-(c) shows the exergetic efficiency of the TES for options (a) I and IV, (b) II and (c) III. The trends of exergetic efficiency with temperature and pressure are the same as the trends for discharge efficiency, shown in Fig. 25. The highest exergetic efficiency is obtained with option III (0.90), followed by options II (0.84), I (0.81) and IV (0.80). Option III has the highest exergetic efficiency because the maximum pressure is not limited by the exit quality. As a result, this option has the smallest difference between the saturation temperature of charging steam (178°C) and discharging steam (158°C).

Table 8 lists the storage capacities (Q_{store}) for all options. The table includes the temperature/pressure of the charging steam and the temperature/pressure combination selected from Fig. 25 and Fig. 26 for discharging the TES. Options I and IV have the lowest storage capacity, 2.09 and 2.05 GWh_{th}, respectively, because steam from the exit of the steam generator provides the highest charging temperature (271°C) and highest discharge

efficiency. For Options II and III, the charging temperatures are 182°C and 251°C and the required storage capacities are 2.66 and 2.41 GWh_{th}.

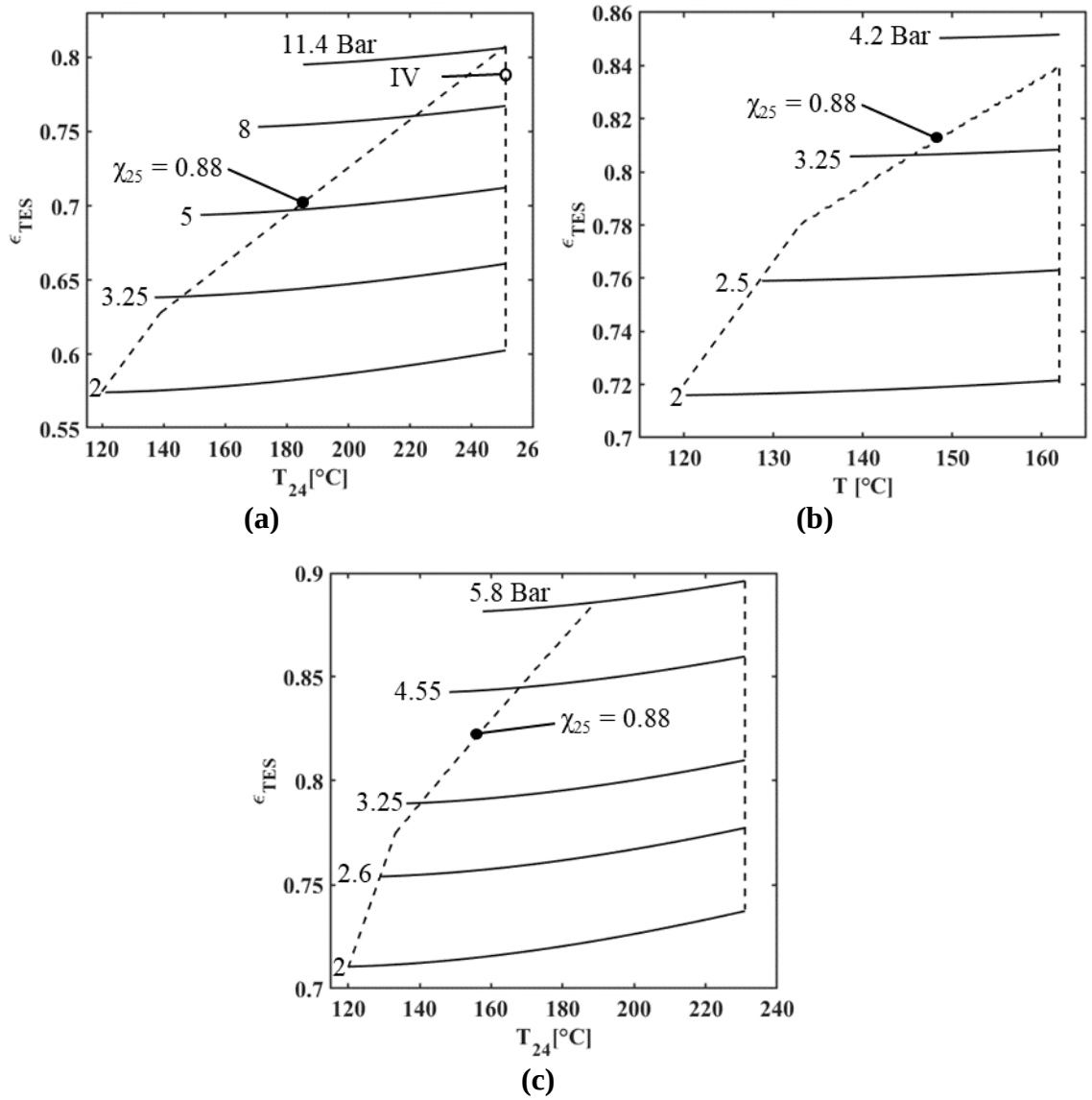

Fig. 26. Exergetic efficiency of the TES (ε_{TES}) as a function of the TES outlet pressure (P_{24}) and temperature (T_{24}) for option I (a), option II (b) and option III (c) at F_D = 1. The fixed pressure/temperature for option IV is indicated by an open circle data marker on the plot (a) for option I.

Table 8. Storage Capacity ($Q_{TES,C}$), charging and discharging steam conditions and discharging figures of merit, discharge efficiency (η_D) and TES exergetic efficiency (ε_{TES}) for options I-IV for design conditions $F_D = 1$.

		Charging		Discharging			
Option	$Q_{TES,C}$ [GWh_{th}]	T [°C]	P [Bar]	T_{24} [°C]	P_{24} [Bar]	η_D	ε_{TES}
I	2.09	271	55	251	11.4	0.23	0.81
II	2.66	182	10.5	162	4.14	0.18	0.84
III	2.41	251	9.5	231	5.80	0.20	0.90
IV	2.05	271	55	251	10.90	0.23	0.80

3.4.2 Charge/Discharge Cycle for the Design Condition ($F_D = 1$)

In this section we present the performance of the nuclear power plant for the TES design conditions listed in Table 8. Figure 27 shows the capacity factor (Fig. 27(a)) and thermal efficiency (Fig. 27(b)) versus charging fraction for options I – IV and steam bypass (labelled 'BP'). In an electrical grid in which the nuclear power plant integrated with TES complements VRE generation, the charging mass fraction would vary with temporal variations in VRE generation. Baseload operation is represented by $F_C = 0$; CF is unity and $\eta_{PP} = 0.31$ for the AP1000 [29]. For TES options I and III and steam bypass, the baseload values are unchanged. For option II, the baseload values are slightly lower due to modifications to the HPT turbine to accommodate increased mass flow rates during charging; CF = 0.9 and $\eta_{PP} = 0.28$. For option IV, the baseload values are lower due to modification of the LPT to accommodate higher mass flow rates during discharging; CF = 0.99 and $\eta_{PP} = 0.31$.

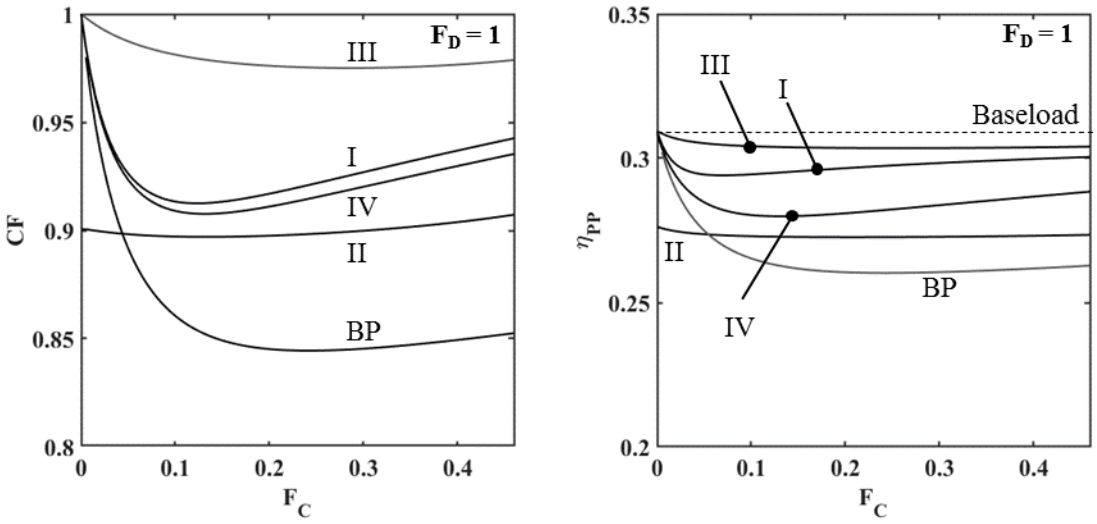

Fig. 27. Capacity factors relative to baseload (a) and thermal efficiency (b) of options I - IV and steam bypass for $0 \leq F_C \leq 0.46$ and $F_D = 1$.

For all storage options and steam bypass, CF and η_{PP} decrease as steam is diverted. In practice, the charging mass fraction is likely to be greater than 0.1 based on forecasts for off-peak hours by the California Independent System Operator (CAISO) for 2021 [49]. The prediction is off–peak demand will be as long as 19 hours per day and super off–peak hours, when demand is much lower than supply, will be seven hours/day [49]. As illustrated in Fig. 28, which shows the time to charge the TES as a function of F_C, charging mass fractions equal to or greater than 0.1 are reasonable to fully charge the TES during the projected off–peak and super off–peak hours. As a representative example, we focus the discussion on $F_C = 0.2$, corresponding to $2.2 \leq t_C \leq 2.8$ hours depending on the storage option. Option III offers the highest CF and η_{PP}; CF = 0.98 and $\eta_{PP} = 0.30$. For option I, CF = 0.92 and $\eta_{PP} = 0.29$. For option IV, CF = 0.91 and $\eta_{PP} = 0.28$. For option II, CF = 0.90 and $\eta_{PP} = 0.27$. TES offers a significant performance advantage over steam bypass, for which CF = 0.85 and $\eta_{PP} = 0.26$.

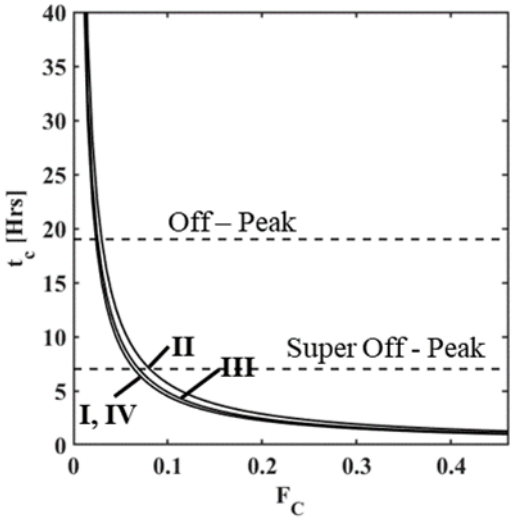

Fig. 28. Charging times (t_C) to fully charge the TES for options I - IV with limits shown for a full-charge at off–peak and super off–peak hours.

To better visualize the advantage of TES over steam bypass, the ratios of capacity factor and efficiency of the storage options and steam bypass are plotted in Fig. 29 versus F_C for $F_D = 1$. The ranking of options follows Fig. 27. In general, the benefits of TES over steam bypass increase with increasing F_C. For $F_C > 0.2$, CF/CF_{BP} and η_{PP}/η_{BP} are less sensitive to increases in charging mass fraction and thus by implication, less sensitive to increases in VRE power. The relative capacity factor (and relative efficiency) for option III is 1.15 for $F_C > 0.1$. Options I and IV have relative capacity factors (and efficiencies) of 1.09 and 1.08 at $F_C = 0.2$. Option II has the lowest relative capacity factor and thermal efficiency of 1.06.

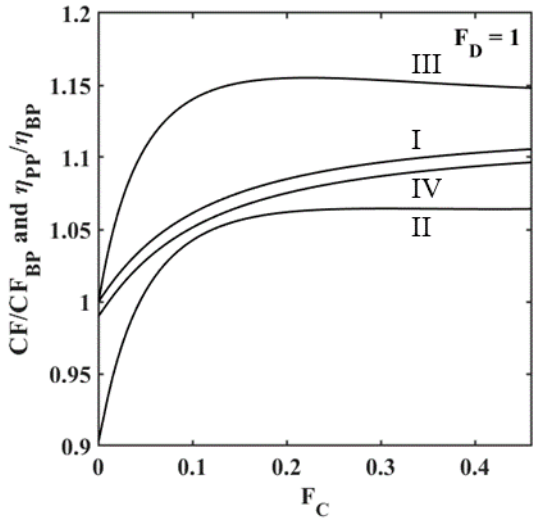

Fig. 29. Relative capacity factor (CF/CF_{BP}) and relative thermal efficiency (η_{PP}/η_{BP}) for options I - IV compared to bypass values for $0 \leq F_C \leq 0.46$ and $F_D = 1$.

3.4.3 Charge/Discharge Cycle for Off Design Conditions ($F_D < 1$)

The discharging fraction would be varied to meet variations in peak demand. To address how changes in F_D impact performance of the plant, we consider off design operation of the TES for $0 \leq F_D \leq 1$. The discharge efficiency, shown in Fig. 30, is highest for option IV, 0.23, with only a 3% variation over the range of discharging fraction. Option IV is the only storage option that operates for $F_D < 0.3$ because even as F_D approaches zero, the mass flow rate through the LPT is greater than the minimum value of 30% of the design mass flow rate. For discharge to a secondary cycle, option I provides the highest discharge efficiency. At $F_D = 1$, the discharge efficiency is the same as that for option IV, but as the mass flow rate through the TES is decreased to reduce power, the discharge efficiency decreases monotonically to 0.16 at $F_D = 0.3$. Options II (0.18 – 0.11) and III (0.20 – 0.15) behave similarly to option I but with lower discharge efficiencies.

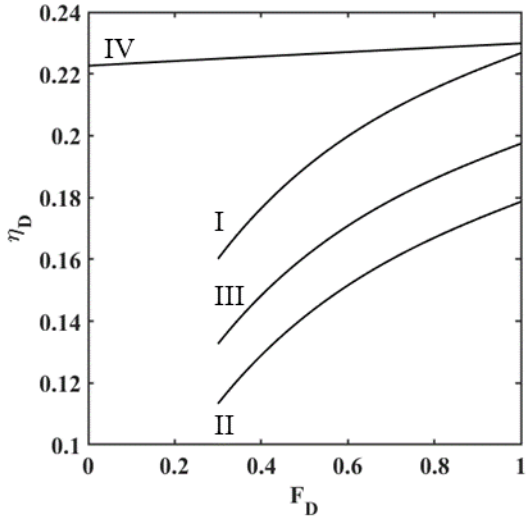

Fig. 30. Discharge efficiency (η_D) for options I - IV for $0 \leq F_D \leq 1$.

The impact of the variation of F_D on the capacity factor and thermal efficiency relative to steam bypass is shown in Fig. 31. Results are shown for $F_C = 0.2$. Relative capacity factors and thermal efficiencies increase with increasing discharging fraction (and thus increasing η_D). Option III operates at the highest thermal efficiency and capacity factor for $0.3 \leq F_D \leq 1$. Relative to steam bypass, CF and efficiency increase from 1.05 at F_D = 0.3 to 1.15 at $F_D = 1$. Options I and IV have similar performance with the exception that option I cannot operate for $F_D < 0.3$. For option I, relative capacity factor and thermal efficiency increase from 1 to 1.09 over $0.3 \leq F_D \leq 1$. For option IV, relative capacity factor and thermal efficiency increase from 1 to 1.08 over $0 \leq F_D \leq 1$ Option II is the poorest performer. Relative capacity factor and thermal efficiency increase from 0.95 to 1.06 over $0.3 \leq F_D \leq 1$.

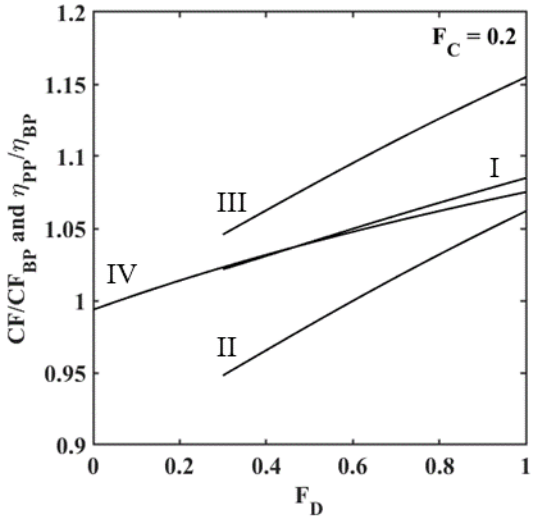

Fig. 31. Relative capacity factor (CF/CF_{BP}) and relative thermal efficiency (η_{PP}/η_{BP}) for options I - IV compared to bypass values for $0 \leq F_D \leq 1$ and $F_C = 0.2$.

Options III and IV are good candidates for implementation of TES. Option III has the highest relative first and second law efficiencies and capacity factor over the full range of charging and discharging mass fractions considered. Option IV has a slight reduction in relative capacity factor and efficiency compared to option I, but it can be operated at discharge fractions less than 0.3 and does not require a secondary power cycle. The TES storage capacities are comparable, 2.05 GWh_{th} and 2.09 GWh_{th}. These results are specific to a four-hour discharge at 119 MW_e and but provide a good comparison of the four power plant/TES configurations. Additional consideration of the mix of generation sources in the grid and consumer demand to determine how operation would be affected and to optimize storage capacity and power requirements.

3.5 Conclusion

Thermal energy storage is considered as a method to increase the flexibility of a baseload electric power plant and thus facilitate higher penetration of solar and wind and decarbonization of the electric grid. First and second law thermodynamic models of TES integrated with a 1052 MW_e nuclear power plant are developed and applied to compare the

pros and cons of four options for charging and discharging the TES within the power cycle. The present work extends prior work [46] that was restricted to the single option (referred to as option IV) of charging the TES with steam diverted at the outlet of the steam generator and discharging the TES to the LPT. In the present study, we consider three new storage options which discharge to a secondary cycle. The three options are differentiated by where in the primary cycle steam is diverted for charging. We consider diversion at the outlet of the steam generator (option I), at the outlet of the HPT (option II), and at the outlet of the MSR (option III). The storage options are compared to steam bypass. The comparison is based on the discharge efficiency, the TES exergetic efficiency, and the capacity factor and the thermal efficiency of the power plant over a charge/discharge cycle. The performance of the plant is explored over a range of steam mass flow rates for both charge and discharge. The study is the first to consider how storage impacts the behavior of a nuclear power plant. The results reveal important aspects of using TES in this application and point toward the focus of future work.

All storage options reduce the capacity factor and thermal efficiency during a charge/discharge cycle compared to baseload operation without storage. However, based on earlier work by Denholm et al. [20] and Forsberg and co-workers [17], [19], [24], [25], [39], [41], the benefit of increased flexibility is significant in terms of providing greater opportunity for renewable energy. Implementing these storage options would require optimization of the storage capacity and power output to best support the mix of generation resources in the grid.

All TES options outperform steam bypass. Though steam bypass provides flexibility, the energy of the steam that is diverted from the steam generator is lost. TES

provides the ability to recuperate that energy and use it for peaking power when renewable energy generation cannot meet the load. We identify two promising storage options. TES option III with discharge to a secondary cycle provides the highest capacity factor and efficiency. The capacity factor and efficiency are 115% of that for steam bypass at steam flow rates that represent practical values. Option IV, which discharges to the primary cycle, and thus is not burdened by the cost of a secondary cycle, has capacity factors and efficiencies as much as 108% of that for steam bypass and has the smallest TES storage capacity. In addition, this option is capable of discharge at very low power which may be beneficial in some situations. Both options are considered worthy of additional economic analysis followed by development of TES storage modules for this application.

3.6 Supplementary Information

The HPT inlet condition (SP 2) is the same for all options and values of F_C (55 Bar, 271°C). Without charging ($F_C = 0$), the extraction and outlet pressure and temperature are 30 Bar and 241°C and 10.5 Bar and 182°C. The HPT generates 380 MW at $F_C = 0$. For option I, the pressure and temperature at the extraction point (SP 14, 15, 19) and the exit (SP 3) rise nonlinearly with increasing F_C. The nonlinearity is attributed to the shape of Stodola's ellipse when maintaining a constant inlet pressure and decreasing the mass flow rate and the nonlinear reduction in isentropic efficiency. The isentropic efficiency decreases from 0.84 to 0.81 Power is reduced monotonically from 380 MW at $F_C = 0$ to 50 MW at $F_C = 0.46$.

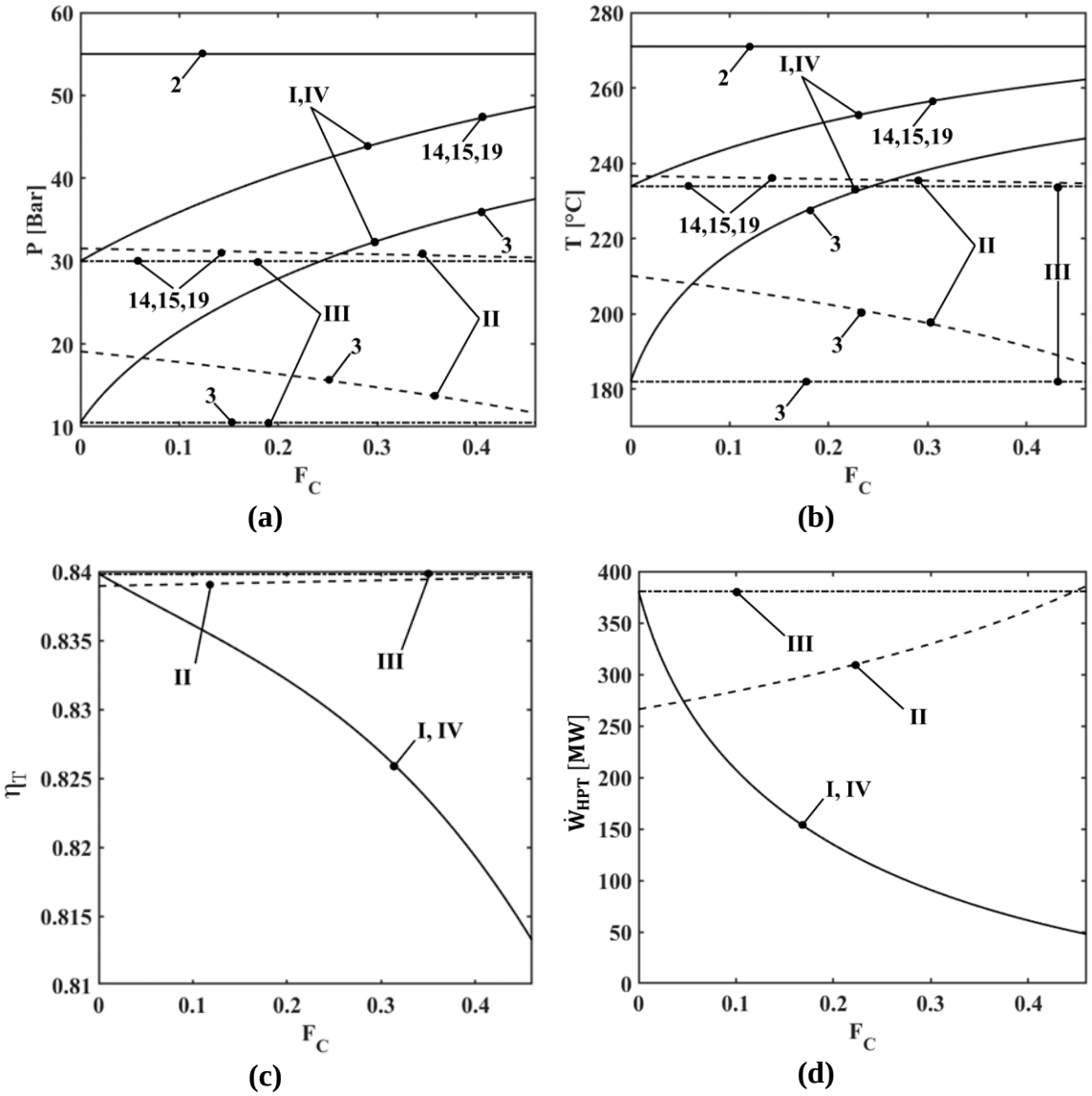

Fig. 32. Behavior of the HPT during charging for $0 \leq F_C \leq 0.46$: (a) pressure and (b) temperature for options I and IV (solid lines), II (dashed lines) and III (dash dot lines) for the inlet (SP 2), extraction points (SPs 14,15,19) and outlet (SP 3); (c) turbine isentropic efficiency and (d) high – pressure turbine power.

For option II, steam is diverted at the exit of the HPT and before the MSR and thus less steam is needed for reheating (SPs 1a and 19) the mass flow rate exiting the HPT (SP 3) as F_C is increased. The mass flow rate at the inlet of the HPT increases from 1800 at baseload to 1830 kg/s at $F_C = 0.46$. The mass flow rate into the second section of the HPT increases from 1260 kg/s at $F_C = 0$ to 1430 kg/s at $F_C = 0.46$. The temperature and pressure

decrease nonlinearly with increasing F_C. Pressure decreases at the extraction point from 31.5 Bar to 30 Bar and the exhaust decreases from 19.5 Bar to 10.5 Bar. Steam enters the HPT as a saturated vapor; therefore, the extraction point and exit are a mixed phase and the reduction in temperature follows the saturation temperatures of steam pressure. The magnitude of the change of temperature and pressure is smaller than the magnitude of change in option I because the magnitude of the change in mass flow rate is less over $0 \leq F_C \leq 0.46$. The nonlinear decrease in pressure and temperature is attributed to the shape of Stodola's ellipse when maintaining a constant inlet pressure and increasing the mass flow rate and the nonlinear increase in isentropic efficiency. The change in isentropic efficiency is smaller (0.1%) over the range of F_C compared to option I because of the small increase in mass flow rate. The decrease in pressures and temperatures increase the power monotonically from 260 MW at $F_C = 0$ to 385 MW at $F_C = 0.46$. Compared to all other options, at $F_C = 0$, the power out of the HPT is 120 MW lower. The lower power at $F_C = 0$ is credited to increasing the size of the turbine to accommodate the addition mass flow rate while maintaining the inlet pressure and keeping the turbine exit pressure greater than the baseload condition.

For option III, the diversion of steam for charging the TES is after the HPT and MSR and therefore there is no change in mass flow rate with increasing charging mass fraction. Likewise, pressure, temperature and power of the HPT are not affected by changing the charging fraction. The only difference between options IV and I is during discharge, and thus there is no difference in operation of HPT during charging as shown in Fig. 32.

The LPT outlet pressure and temperature are the same for all options and values of F_C (0.1 Bar, 46°C). The fixed pressure and temperature of the LPT exhaust are dictated by rejection of heat at a temperature no greater than 46°C for environmental considerations. Without charging, the pressures at the inlet and extraction points are 9, 3.5, 3, 1.5, 0.5 Bar. The pressures and corresponding temperatures at $F_C = 0$ are summarized in the 'Baseload' column in Table 9. For option I, the inlet pressure drops from 9.5 Bar to 4.17 Bar. The steam is throttled to achieve this pressure. Because throttling is an isenthalpic process, the temperature decreases from 251°C to 241°C. Due to the throttling of steam at the inlet and reduced mass flow rates through the LPT, the pressures and temperatures at the extraction points reduce with increasing charging fraction. The total decreases at $F_C = 0.46$ are summarized in Table 9. Unlike the HPT, the reduction in pressure is linear. The linear reduction in pressure is due to the shape of Stodola's ellipse when selecting to keep a fixed outlet pressure. For state points outside the vapor dome (SP 4) the temperature decreases linearly. For state points inside the vapor dome the temperature decreases nonlinearly. The reduction in turbine work is nonlinear due to the nonlinear reduction in turbine isentropic efficiency (0.84 to 0.8). The behavior of the LPT during charging for option II is identical to option I because the flow rates into the turbine are exactly the same and the LPT has not been redesigned to accommodate additional mass flow rate at discharge. The power of the LPT for options I and II reduces from 693 MW at $F_C = 0$ to 225 MW at $F_C = 0.46$.

The LPT outlet pressure and temperature are the same for all options and values of F_C (0.1 Bar, 46°C). The fixed pressure and temperature of the LPT exhaust are dictated by rejection of heat at a temperature no greater than 46°C for environmental considerations. Without charging, the pressures at the inlet and extraction points are 9, 3.5, 3, 1.5, 0.5 Bar.

The pressures and corresponding temperatures at $F_C = 0$ are summarized in the 'Baseload' column in Table 9. For option I, the inlet pressure drops from 9.5 Bar to 4.17 Bar. The steam is throttled to achieve this pressure. Because throttling is an isenthalpic process, the temperature decreases from 251°C to 241°C. Due to the throttling of steam at the inlet and reduced mass flow rates through the LPT, the pressures and temperatures at the extraction points reduce with increasing charging fraction. The total decreases at $F_C = 0.46$ are summarized in Table 9. Unlike the HPT, the reduction in pressure is linear. The linear reduction in pressure is due to the shape of Stodola's ellipse when selecting to keep a fixed outlet pressure. For state points outside the vapor dome (SP 4) the temperature decreases linearly. For state points inside the vapor dome the temperature decreases nonlinearly. The reduction in turbine work is nonlinear due to the nonlinear reduction in turbine isentropic efficiency (0.84 to 0.8). The behavior of the LPT during charging for option II is identical to option I because the flow rates into the turbine are exactly the same and the LPT has not been redesigned to accommodate additional mass flow rate at discharge. The power of the LPT for options I and II reduces from 693 MW at $F_C = 0$ to 225 MW at $F_C = 0.46$.

Table 9. Pressure and temperature of the LPT inlet (SP 4), extractions (SPs 9 – 12) and outlet (SP 5) at baseload and at $F_C = 0.46$ for options I – IV.

	Baseload		I		II		III		IV	
SPs	P [Bar]	T [°C]	P [Bar]	T [°C]	P [Bar]	T [°C]	P [Bar]	T [°C]	P [Bar]	T [°C]
4	9.5	251	4.17	242	4.13	242	2.88	240	4.17	242
9	3.5	157	1.39	147	1.38	146	0.88	142	1.39	147
10	3	144	1.17	132	1.15	132	0.72	127	1.17	132
11	1.5	111	0.55	83	0.55	83	0.33	72	0.55	83
12	0.5	81	0.19	59	0.19	59	0.13	51	0.19	59
5	0.1	46	0.10	46	0.10	46	0.10	46	0.10	46

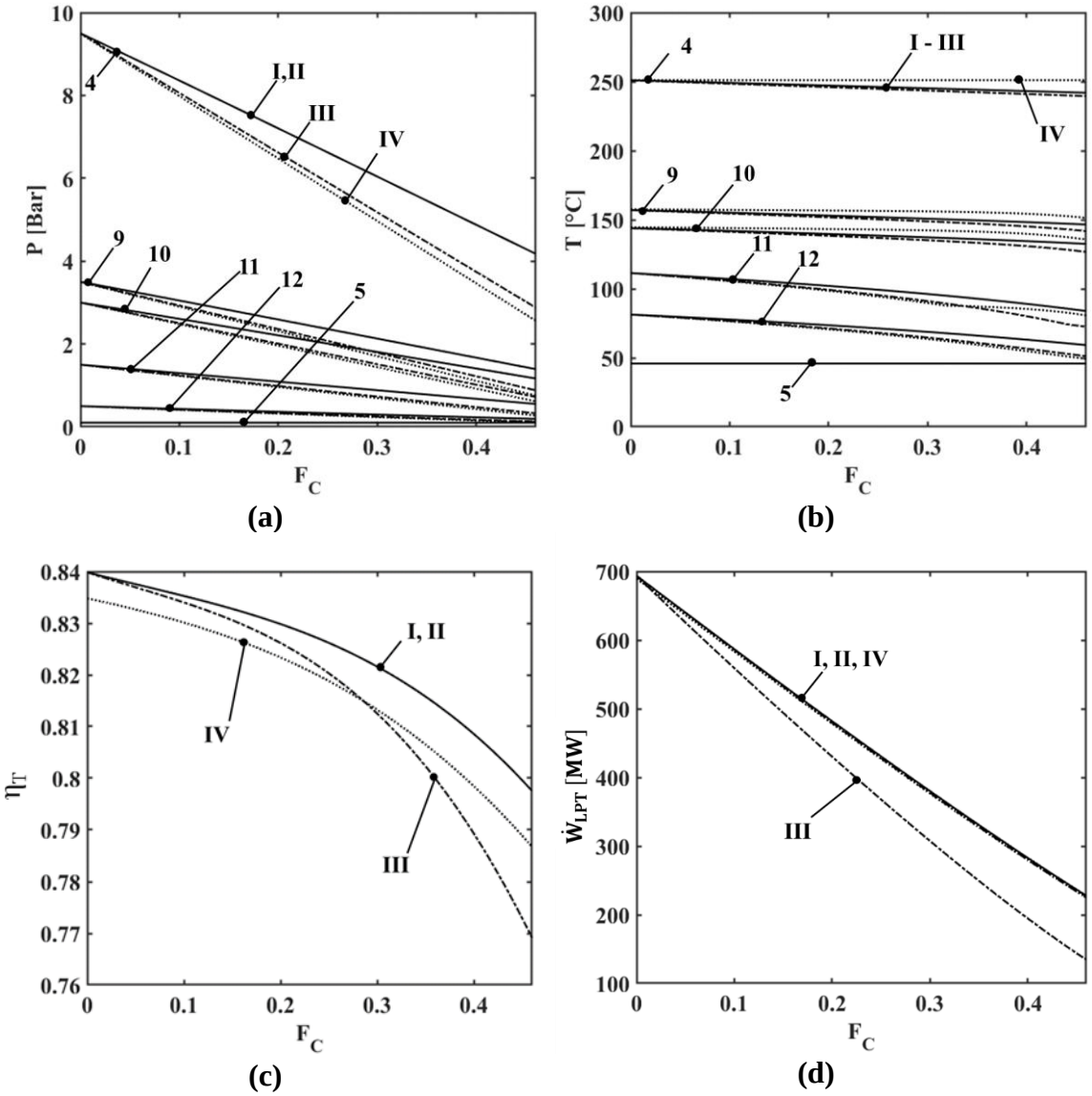

Fig. 33. Behavior of the LPT during charging for $0 \leq F_C \leq 0.46$: (a) pressure, (b) temperature for options I (solid lines), II (dashed lines), III (dash dot lines) and IV (dotted lines) for the inlet (SP 4), extraction points (SPs 9 -12) and outlet (SP 5); (c) turbine isentropic efficiency and (d) low – pressure turbine power.

For option III, there is a greater decrease in pressure than options I and II over the range of F_C. As previously mention, for storage options in which steam is diverted before the MSR (I, II and IV), the amount of steam needed for reheating is reduced. Therefore, for the same F_C, option III has a lower steam mass flow rate through the LPT, resulting in lower pressures. The inlet pressure is reduced from 9.5 Bar at $F_C = 0$ to 2.88 Bar at $F_C =$

0.46. Extraction pressures and temperatures decrease and are summarized in Table 9. The lower mass flow rate results in a greater reduction in isentropic efficiency (0.84 to 0.77). The combination of a greater reduction in pressure and isentropic efficiency contribute to the greatest reduction in LPT power for all options. The LPT power is reduced from 693 MW to 134 MW over the range of F_C.

For option IV, the reduction in pressure over $0 \leq F_C \leq 0.46$ is similar to option III and reductions in temperatures are similar to all other options. The primary difference in option IV is illustrated in the isentropic efficiency of the LPT. At $F_C = 0$, $\eta_{s,LPT} = 0.835$. The LPT has been redesigned to accommodate additional steam at discharge. At $F_C = 0$, the LPT is not operating at its highest mass flow rate and therefore has a slight reduction in isentropic efficiency compared to options I – III. Option IV has the lowest isentropic efficiency for $F_C < 0.285$. For $F_C > 0.285$ the isentropic efficiency is greater due to the higher mass flow rates in the LPT due to reductions in steam mass flow rates to the MSR as previously discussed. The impact of the reduction in isentropic efficiency on the turbine power is almost undiscernible at $F_C = 0$, reducing the power by 4 MW compared to options I – III. The LPT power barely deviates from options I and II never varying more than 4 MW over the range of F_C.

Figure 34 illustrates the behavior of the secondary power cycle used for converting steam generated by the TES to turbine work. These plots support Fig. 30 in the main text showing the discharge efficiency (η_D) as a function of the discharging mass fraction (F_D). Options I – III are shown in Fig. 34. Detailed discharging operation for option IV is detailed in the main text in section 2.4.2. The turbine exit pressure and temperature are the same for all options (0.1 Bar and 46°C). For option I, the turbine inlet pressure increases linearly

from 3.5 Bar at $F_D = 0.3$ to 11.4 Bar at $F_D = 1$. Similar to charging for the LPT, the linear increase in pressure is due to the constant turbine outlet pressure. The temperature shows a slight increase over the same range. The temperature and pressure at $F_D = 1$ are equivalent to the temperature and pressure given in Table 3 (in the main text) (11.4 Bar and 251°C). The increase in temperature (237 – 251°C) is due to isenthalpic throttling of the steam from the steam generator outlet to the calculated turbine inlet condition. As a function of F_D, the secondary cycle turbine isentropic efficiency increases from 0.77 to 1 over the range $0.3 \leq F_D \leq 1$. For a steam turbine, a mass flow rate of at least 30% of the design condition is needed to generate power. The power increases from 25 – 119 MW. These results increase η_D from 0.16 to 0.23 for $0.3 \leq F_D \leq 1$. Having the highest η_D,, option I requires the smallest discharging mass flow rate (185 kg/s) to generate 119 MW. Option I has the highest η_D for all options discharging to the secondary cycle.

For option II, the pressure and temperature of the steam generated during discharge are the lowest for all options. The turbine inlet pressure increases 1.5 Bar to 4.8 Bar, and the temperature increases from 152 to 162° over the range of F_D. Like option I, the increase in pressure and temperature are linear and are a consequence of the constant turbine outlet pressure and the effects of isenthalpic throttling. There is no difference between the effects of F_D on isentropic efficiency for all charging options. In the discharging fraction, the discharging mass flow rate is normalized by the mass flow rate required to generate 119 MW. The normalizing mass flow rate is given in Table 8. For each option, equivalent values of F_D have different mass flow rates. Option II increases from 22.64– 199 MW. To generate 119 MW, the mass flow rate out of the TES in option II is 249 kg/s. The slight deviation in power at lower values of F_D is due to the significant decrease in η_D compared

to option I. The value of η_D in Fig. 30 is lower than all other storage options, increasing from $\eta_D = 0.11$ at $F_D = 0.3$ to $\eta_D = 0.18$ at $F_D = 1$.

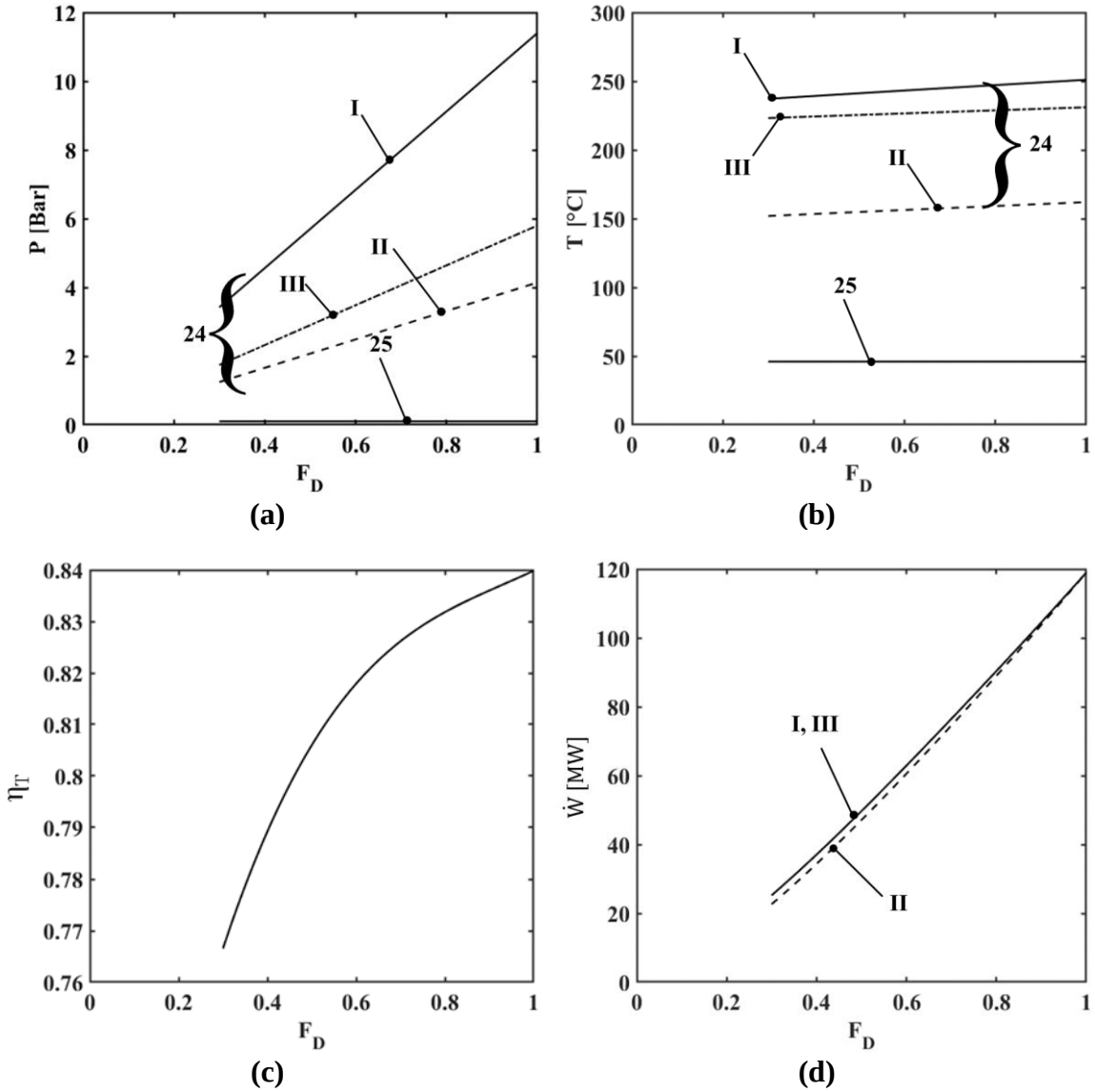

Fig. 34. Behavior of the secondary cycle turbine during charging for $0 \leq F_D \leq 1$: (a) pressure, (b) temperature for options I (solid lines), II (dashed lines) and III (dash dot lines) for the inlet (SP 24), and outlet (SP 25); (c) turbine isentropic efficiency and (d) low – pressure turbine power.

Option III has the second highest TES discharge pressure and temperature as given in Table 8 and thus has the second highest η_D among the options discharging to a secondary cycle. Similar to options I and II, the increase in pressure and temperature is linear over 0.3

$\leq F_D \leq 1$. The pressure increases from 1.7 Bar to 5.8 Bar and the temperature has only a slight increase from 223°C to 231°C. Isentropic efficiency over the range of F_D is identical to options I and II. Secondary cycle turbine power is only marginally less than option I (1.2 MW at $F_C = 0.3$) and indiscernible when plotted (Fig. *34*(d)). These change in state points and isentropic efficiency increase the overall discharge efficiency from 0.14 to 0.2 over $0.3 \leq F_D \leq 1$.

Detailed state point values and a discussion of option IV are discussed in the main text in Chapter 2.

4 Parametric Study of Thermodynamic and Cost performance of Thermal Energy Storage Coupled with Nuclear Power

Thermal energy storage for nuclear power can increase the flexibility of low carbon baseload power plants and facilitate greater use of renewable energy sources. The thermodynamic performance and cost of approaches to integrate thermal energy storage with a 1050 MW nuclear power plant are compared in a parametric study over practical ranges of charge/discharge durations, peaking power and round-trip efficiency of the storage. Conceptual designs for sensible and latent heat storage modules are presented. The results quantify for the first time how different options for thermal energy storage affect technical performance of a nuclear power plant and are interpreted to identify the most efficient options and operating conditions. The three configurations are distinguished by charge and discharge operation. Configuration I charges the storage via high-pressure steam supply and discharges steam to the low-pressure turbine. Configuration II charges via high–pressure steam and discharges preheated condensate to the steam generator. Configuration III charges via low-pressure steam and discharges steam to a secondary Rankine cycle. The diurnal energy production ratio, or capacity factor, versus peaking power, and storage material cost are the metrics used to compare configurations. Configuration III, which does not require changes to the primary cycle turbines and thus has no detrimental impact on the efficiency of baseload operation, has the highest energy production ratio of 0.99. Energy production ratio increases as charging duration and discharge power are reduced. Configurations I and III can provide peaking power more

than 1.5 times the baseload plant. Configuration II is limited to a peaking power of less than 1.1 times that of baseload and is cost effective in this range, albeit with lower energy production ratio than configuration III. Sensible heat storage in a rock bed is more economical than latent heat storage due to the relatively high cost of eutectic salt mixtures with appropriate melt temperatures. Keywords: thermal storage, nuclear, thermodynamic, sensible heat, latent heat

4.1 Introduction

The rapid growth of variable renewable energy (VRE) sources, such as wind and solar, can disrupt the balance utilities must sustain to provide electricity for fluctuating demand as shown by models of power grids by the U.S. National Renewable Energy Laboratory [83]. When regional penetration of wind and solar rises above 10%, VRE sources may be curtailed in favor of dispatchable energy sources such as natural gas, coal and nuclear [53]. Greater flexibility of conventional baseload power plants to respond to dynamic changes in supply and demand has been suggested as one important route to speed the expansion of solar and wind on the grid [50]. One option to increase the flexibility of baseload power plants is energy storage [39]. Of the limited energy storage deployed by utilities, the majority is pumped hydro storage. Despite the increasing need for energy storage, deployment of pumped hydro has slowed due to geographical limitations [83] and public policy barriers [15]. Batteries and the associated power electronics are gaining interest but are not yet economically attractive for widespread utility-scale use [16].

Thermal energy storage (TES) has the potential to provide utility-scale energy storage at an order of magnitude lower cost than batteries and at equivalent cost to pumped hydro [12]. Thermal energy storage can be integrated with any size thermal power plant at any location. Thermal energy is stored during periods when electricity prices are low and

then the stored thermal energy is converted to electricity when electricity prices are high. According to Forsberg et al. [17] the increase in the value of electricity from nuclear power plants with storage could ensure that low carbon nuclear energy is more financially secure, reversing the trend of uneconomic operation of nuclear power plants. This economic situation is made more challenging in non-regulated markets [36]. Denholm et al. recommend TES with nuclear power to provide low carbon peaking power and predict capacity factors of nuclear with TES for hypothetical power grids [20]. The prior work does not model the impact of TES on the efficiency of the baseload plant.

In the U.S., the existing fleet of nuclear power plants was designed for constant power and, consequently, cannot rapidly control power to accommodate changes in supply or demand. Practical limits on the rate of modulation of power are < 0.5% per minute [8] down to 50% of rated power [27]. The limits on flexible operation are attributed to the risk of thermal stresses induced in the fuel assembly [8]. With TES, changes in power can be accomplished without the risk of thermal stresses in the reactor. The ramp rate, or rate of change of power, is limited only by the ability to modulate the steam turbines and the rate of heat addition or extraction from the TES. Most turbines are able to change power about 7% per minute [27], with a maximum decrease of 30% of rated power. In a review of approaches to electrical energy storage, the rates of power modulation on the order of MW/min were suggested to meet the majority of requirements for time-shifting supply related to electricity pricing, and changes in supply and demand due to use of VRE [11]. Modeling of the California grid with 60% VRE penetration shows that the maximum upward ramp rate is 3,142 MW/hr. A 1050 MW_e nuclear power plant, such as the one presented in this work, able to operate with a change of power of 7% per minute is able to

meet this maximum. Batteries and super capacitors can provide frequency control for which response time is on the order or seconds and storage requirements are less than 1 MWh_e

Carlson et al. [46], Carlson and Davidson [48] and Kluba and Field [45] proposed different options of integrating TES into the Rankine power cycle, and modeled the capacity factor for a fixed discharge power over single a charge/discharge cycle. As discussed in more detail in the following three paragraphs, the prior work provides sufficient data to select integration options for the present parametric study, but the prior modeling studies do not capture the technical performance of TES with nuclear over the range of operating scenarios that could be encountered in power grids, particularly with high penetration of solar and wind. Moreover, the impact of TES on the operation of the plant during baseload operation (i.e., neither charging nor discharging) was not included in the previously reported capacity factors. As demonstrated in the present work, this impact is important. The present study provides a more accurate and complete technical comparison of options for TES used with nuclear power.

In the first technical evaluation of TES with nuclear power, Carlson et al. [46] developed and applied a first law thermodynamic model of TES integrated within the primary cycle of the Westinghouse AP1000 nuclear power plant (rated at 1050 MW_e) [62]. In the configuration initially proposed, referred to in the present work as configuration I, the TES is charged by diverting steam exiting the steam generator to charge the TES. The stored energy is discharged to generate steam which is expanded in the low-pressure turbine (LPT). Typically, modification, as opposed to replacement, of turbines can accommodate mass flow rates up to 115% of the design point mass flow rate [97]. For a

one hour charge and a full discharge, the reported capacity factor is 9.8% higher than the capacity factor for steam bypass. The capacity factor was defined as the ratio of energy generated over a cycle of charge and discharge to the energy that would have been generated in conventional operation without TES. TES will always provide higher capacity factor than will steam bypass, which is non-storage alternative for reducing baseload power.

Carlson and Davidson also considered discharging the TES to a secondary cycle, referred to in the present work as configuration III [48]. Configuration III provides the ability to scale-up discharge power without modification to the primary cycle. Charging the TES was explored using both high- and low-pressure steam. Diverting low-pressure steam yields higher capacity factors and thus the present study considers this approach. In the prior work, discharge power of the secondary cycle was constrained to 119 MW_e to allow direct comparison with discharge to the primary cycle. In this case, capacity factor over a charge/discharge cycle is 15% higher than capacity factor with steam bypass.

Kluba and Field [45] modeled TES for the Korea Electric Power Corporation APR1400 nuclear power plant using the commercial software package PEPSE. The proposed option, referred to in the present work as configuration II, charges the TES using high-pressure steam like configuration I. The configuration is distinct from configuration I in the approach for discharge. The TES is discharged to preheat condensate for the steam generator, allowing steam typically used for preheating to be expanded through the high-pressure turbine (HPT) and LPT. Power during discharge is limited to ~108% of rated baseload power. The approach is similar to that proposed by Richter et al. [98] and Garbrecht et al.[99] to improve load response in coal fired power plants. Kluba and Field

considered a scenario in which the TES is charged for 8 hours followed by 15 hours of discharge. The predicted capacity factor in this case is 81%. A comparison to steam bypass was not provided.

In the present study, three TES configurations are selected from the results of the prior work and the technical performance of these options are modeled over the wide range of operating parameters that could occur in a utility grid to support expansion of VRE. In grid operation, operating parameters, including discharge power and charge/discharge rates and duration, depend on the resource mix, consumer demand and the market regulatory structure. Given the variety of expected operating scenarios, it is critical to understand the impacts of these parameters on the capacity factor and required storage capacity and cost. The impacts of the discharge power, charge and discharge duration and round-trip efficiency of the TES on the diurnal Energy Production Ratio (EPR) versus discharge power ratio (DPR) are presented. The EPR reflects the impact of TES on the efficiency and capacity factor of the plant during charging, discharging and baseload operation. With TES, EPR is less than unity with a higher fraction representing more efficient operation of the plant and TES. The DPR is the ratio of power generated during TES discharge and the power generated in baseload without TES. The relative size and material costs for representative storage materials are presented for sensible and latent heat storage materials. The results are interpreted to suggest favorable ranges of parameters for the configurations and to compare the metrics of the three configurations in probable operating parameters.

4.2 Methods

Detailed configurations of TES within the AP1000 power cycle are presented in section 4.2.1. The modeling approach and model formulation are presented in sections

4.2.2 and 4.2.3, respectively. Concepts of TES storage modules are presented in section 4.2.4.

4.2.1 Thermal Energy Storage and Cycle Configurations

The three TES configurations are: I) TES charging via high-pressure steam supply and discharging steam to the LPT, II) TES charging via high–pressure steam and discharging preheated condensate to the steam generator, and III) TES charging via low-pressure steam and discharging steam to a secondary Rankine cycle. Figure 35 shows operation of the Westinghouse AP1000 nuclear plant with and without storage. The three configurations are differentiated by Roman numeral. Key thermodynamic state-points (SP) are labelled. Numerical values are provided for state-points that are fixed in the analysis. Operation of the baseload power plant is indicated by solid lines. Charging operation is denoted by dashed lines. Discharging is indicated by dotted lines.

4.2.1.1 Configuration I

Configuration I charges and discharges the TES within the primary Rankine cycle. When renewable output is high and it is desirable to reduce baseload power, steam is diverted upstream of the HPT (SP 1) at a temperature and pressure equivalent to the steam generator (271°C and 55 Bar) to charge the TES. Energy is stored as the steam is cooled isobarically to the condenser temperature (46°C, SP 21). The condensate is returned to the feedwater heating system via the condenser. During charging, efficiencies of the HPT and LPT are reduced as the mass flow rate to the TES is increased (commensurate with off-design operation of the turbines).

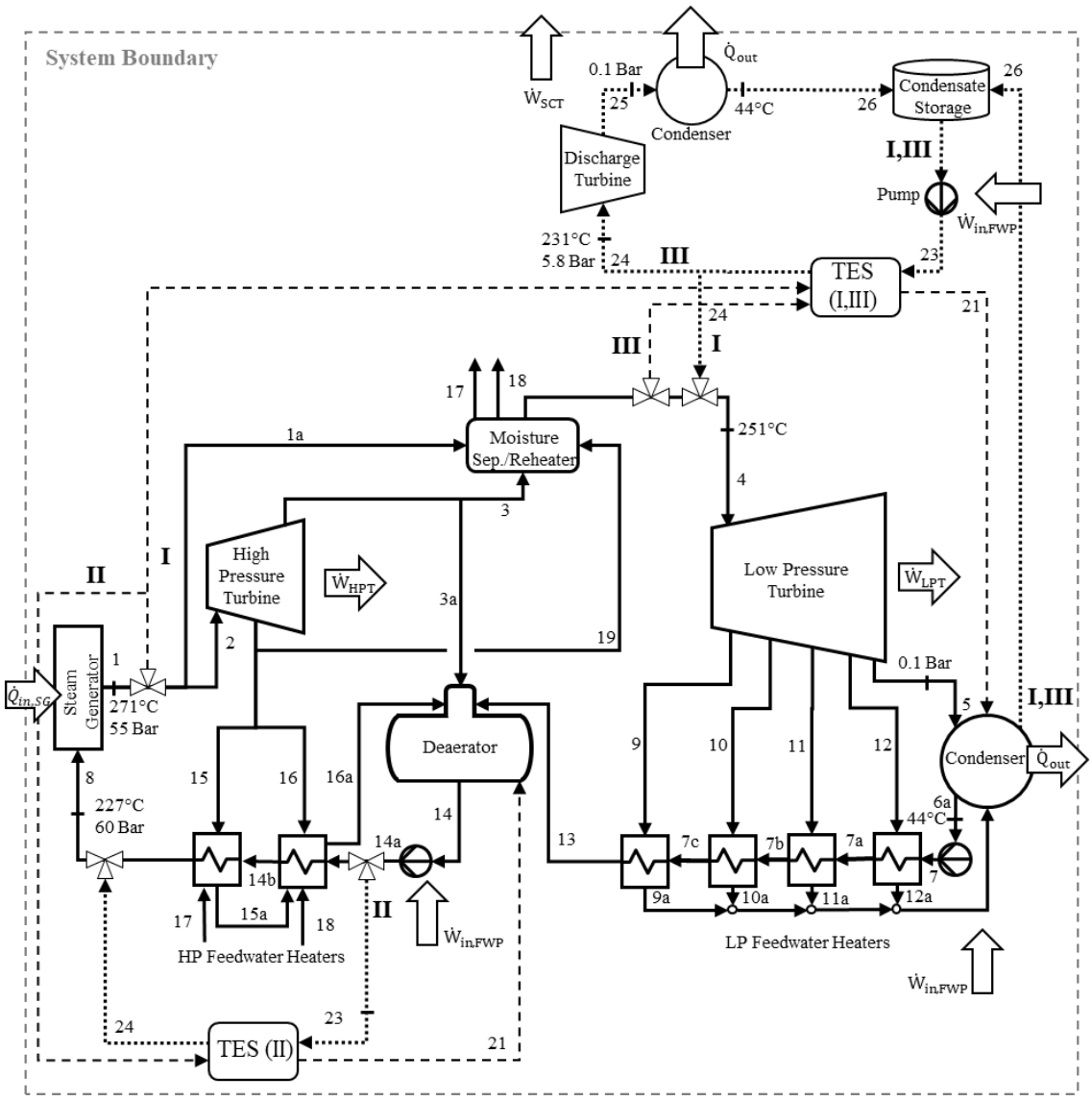

Fig. 35. Diagram of the Westinghouse AP1000 showing baseload, charge and discharge operation of TES configurations I, II and III. Baseload operation is indicated by solid lines. Charging is indicated by dashed lines. Discharging is indicated by dotted lines.

The TES is discharged using water stored at ambient temperature and pressure. The stored water is pressurized to the inlet pressure of the LPT (SP 23) and superheated to 251°C, 20°C cooler than steam used for charging. A temperature difference between charge and discharge is imposed to allow heat transfer to/from the storage material and the charge/discharge fluid. The flow of steam from the TES increases the mass flow rate through the LPT (SP 24). An increase of the mass flow rate up to 15% is possible via an

alteration of the steam flow passage [58]. The mass flow rate through the HPT also increases, but the incremental increase is much less than for the LPT. Water is returned to storage via the condenser.

During baseload operation, the cycle is operated conventionally, but the turbines operate off-design due to modification of the design points of the turbines required for higher flow rates during discharge.

4.2.1.2 Configuration II

Configuration II [45] also integrates the TES within the primary Rankine cycle. Like configuration I, the TES is charged isobarically by diverting steam upstream of the HPT (SP 1) at 271°C and 55 Bar. The temperature of condensate exiting the TES depends on the storage material. For sensible heat storage, using for example rock, the exit temperature is set to 230°C. For latent heat storage, a mixture of 73% sodium hydroxide and 27% sodium nitrite, by molar percentage, ($NaOH:NaNO_2$ (73:27)) is considered and has a melt temperature of 238°C. In this case, water is assumed to exit the TES at 247°C, which is 20°C higher than the temperature of condensate exiting the TES during discharge.

To discharge the TES, condensate is diverted from the high-pressure feedwater heater (SP 14a) to the TES at 210°C and 60 Bar and heated isobarically to the temperature at the inlet of the steam generator (227°C). The discharge power of configuration II is shown to be limited to 110% of baseload.

During baseload, the cycle is operated conventionally, but the HPT and LPT both operate off-design. The penalty of off-design operation of the HPT is greater than for configuration I. The penalty of off-design operation of the LPT is similar to that for configuration I.

4.2.1.3 Configuration III

Configuration III is unique among the three options in that the TES is discharged to a secondary Rankine cycle. The advantage of this approach is the turbines in the primary power cycle do not require modification and do not operate off-design during baseload.

The TES is charged by diverting steam downstream of the moisture separator/reheater (SP 4) at 251°C and 9.5 Bar. There is no change in operation of the HPT. The efficiency of the LPT decreases as the mass flow rate diverted to the TES is increased. Like configuration I, water exits the TES at 46°C (SP 21) and is recycled to the feedwater system via the condenser.

To discharge the TES, stored condensate is pressurized (SP 23) to 5.8 Bar, heated to 231°C and expanded in the secondary cycle steam turbine. The discharge pressure and temperature are the highest possible for the saturation temperature and pressure of steam used to charge the TES.

During baseload, the cycle is operated conventionally with no penalty due to TES.

4.2.2 Modeling Approach

A parametric study quantifies the thermodynamic performance of configurations I, II, and III for four parameters: Discharge Power Ratio (DPR), charge duration (t_C), discharge duration (t_D) and round-trip efficiency of the TES (η_{RT}). The metric for comparison is the diurnal Energy Production Ratio (EPR), which is the ratio of energy generated over 24 hours with TES and the energy that could have been generated over the same period without TES.

$$\mathrm{EPR} = \frac{\dot{W}_C t_C + \dot{W}_D t_D + \dot{W}_{BL} t_{BL}}{\dot{W}_{X,BL}(t_C + t_D + t_{BL})} \tag{50}$$

The subscripts ‘C’, ‘D’ and ‘BL’ refer to charge, discharge and baseload operation with TES. The subscript ‘X,BL’ refers to baseload operation of a plant without TES.

DPR is the ratio of the net power during discharge and the net power without TES.

$$\mathrm{DPR} = \frac{\dot{W}_{D}}{\dot{W}_{X,BL}} \tag{51}$$

Without TES, DPR = 1. With TES, DPR > 1. The DPR is varied over a wide range to capture the range that utilities might desire. There are limits to DPR for each configuration.

The round-trip efficiency (η_{RT}) accounts for the non-ideal behavior of the TES. It is the ratio of energy discharged to energy stored during charging.

$$\eta_{RT} = \frac{Q_{TES,D}}{Q_{TES,C}} \tag{52}$$

For an idealized TES, η_{RT} = 1.

The ranges of DPR, t_C, t_D and η_{RT} listed in Table 10 span the values that might be used to support VRE generation in utility grids. The value of DPR depends on the mass flow rate through the TES during discharge ($\dot{m}_{24}$), which is selected to achieve a desired DPR. For configuration I, the DPR of the primary cycle is limited by the power rating of commercial electrical generators. The largest available electric generator based on data available from manufacturers is 2000 MW_e [100]. Therefore, the maximum DPR considered is 1.9 for the AP1000, assuming an electrical generator efficiency of unity (generator efficiencies approach 99% [101]). For configuration II, DPR is limited to 1.1 by the mass flow rate of steam through the high-pressure feedwater heaters (180 kg/s). For configuration III, an upper limit of DPR = 2 is considered for a single power plant. The Westinghouse Electric Company is investigating the use of TES in future lead cooled

reactors. They aim to achieve power 20% above baseload using TES (i.e., DPR = 1.2) [102]. For this reason, a DPR = 1.2 is presented as a relevant example in the results.

Table 10. Parameter Ranges

Parameter	Symbol	Range	Increment
Discharge Power Ratio	DPR	1-1.9 (I) 1-1.1 (II) 1-2 (III)	~0.005
Charging Duration	t_C	2-10 hour	0.5
Discharging Duration	t_D	2-10 hour	0.5
Round Trip Efficiency	η_{RT}	0.7-1	0.1

Prior economic studies that explored the financial benefit of storage based on energy arbitrage guided the selection of the range of durations of charge and discharge. In this scenario, the TES would be charged during periods when energy prices are low (when generation capacity exceeds demand) and discharged during periods when energy prices are high (when peaking power is required). Considering a nonspecific storage type, Sioshansi et al. [44] predict a charge duration of eight hours would capture 85% of the maximum annual arbitrage value in the PJM interconnection in the eastern U.S. An energy storage round trip efficiency of 0.8 and equal rates of charge and discharge were assumed (i.e., $t_D = t_C\eta_{RT}$). The analysis did not include capital or operation and maintenance costs. McConnell et al. [43] applied a similar approach to model the Australian National Energy Market. They predict 90% of the maximum annual revenue would be captured in a 4 hour charge. Bradbury et al. [42] calculated the internal rate of return (IRR) for energy storage systems for eight U.S. grids and treated capital cost as a parameter. Charge and discharge rates were assumed equal. They set 10% IRR as the goal for profitability. Results indicate IRR $\geq$ 10% for capital costs from \$5 to \$100 per kWh_e and charge durations up to 10 hours.

Cost of TES systems have been reported from $30 to $60 per kWh_e [12]. Based on these economic studies, a range of charge and discharge durations from 2 to 10 hours is studied.

The range of round-trip efficiencies considered is from 0.7 to an idealized maximum of unity. Factors that can affect the round-trip efficiency include the rate of thermal loss to the surroundings and heat transfer during charge and discharge of the TES. Daily thermal losses can be held to about 1% of total energy stored based observed rates in large scale high temperature sensible heat molten salt and solid concrete storage devices for concentrating solar energy [103]. Heat transfer limitations can limit charge or discharge rates which can change as charge/discharge progresses. Round-trip efficiencies of TES as high as 0.95 have been demonstrated for a 105 MWh_{th} pilot scale sensible heat molten salt storage with concentrating solar power [81].

4.2.3 Model Formulation

Component and system level energy balances quantify the first law thermodynamic performance of the AP1000 with and without TES. The model of configurations I [46] and III [48] is described in detail in prior publications. The model of configuration II is built into the same Matlab framework with modification for the change in operation as described in section 2.2. State-point values and turbomachinery isentropic efficiencies for the plant without TES are published values for the AP1000 [29]. The state-point values are modified for the TES configurations. The steam generator provides a thermal input of 3431 MW_{th}, generating steam at 271°C, 55 Bar and 1886 kg/s. The inlet temperature and pressure of the steam generator are 227°C and 60 Bar. Other fixed values in the cycle include LPT inlet temperature (251°C), condenser pressure (0.1 Bar) and condenser exit temperature (44°C).

The TES is modeled as a black box with fixed inlet and outlet temperatures as described for each configuration in section 4.2.1. The storage capacity of the TES ($Q_{TES,C}$) is given by Eq. (53).

$$Q_{TES,C} = \frac{Q_{TES,D}}{\eta_{RT}} = \frac{t_D \dot{m}_{24}(h_{24} - h_{23})}{\eta_{RT}} \tag{53}$$

In the parametric study, set values are the discharge mass flow rate ($\dot{m}_{24}$), charge (t_C) and discharge durations (t_D) and the mass flow rate to the TES during charging ($\dot{m}_{21}$) is adjusted to satisfy Eq. (54).

$$\dot{m}_{21} = \frac{Q_{TES,D}}{\eta_{RT} t_C (h_{TES,in} - h_{21})} \tag{54}$$

State-point enthalpies are evaluated in Matlab using the function XSteam [96].

The net mechanical power is the sum of the power generated by the turbines minus the power to pressurize the condensate ($\dot{W}_{FWP}$).

$$\dot{W}_{net} = \dot{W}_{HPT} + \dot{W}_{LPT} + \dot{W}_{SCT} - \sum \dot{W}_{FWP} \tag{55}$$

$\dot{W}_{SCT}$ is the power of the secondary cycle turbine for configuration III and is not applicable for configurations I and II. Based on the assumptions of steady state operation, adiabatic behavior and no potential and kinetic losses, the power generated by the turbines is

$$\dot{W}_{HPT} = \dot{m}_2(h_2) - (\dot{m}_{15} + \dot{m}_{16} + \dot{m}_{19})(h_{15}) - (\dot{m}_3 + \dot{m}_{3a})(h_3) \tag{56}$$

$$\dot{W}_{LPT} = \dot{m}_4(h_4) - \sum_{SP=9}^{12} (\dot{m}_{SP} h_{SP}) - \dot{m}_5(h_5). \tag{57}$$

For configuration III, power generated by the secondary cycle is

$$\dot{W}_{SCT} = \dot{m}_{24}(h_{24} - h_{25}). \tag{58}$$

Power required to pressurize the condensate in the primary and secondary cycles is

$$\dot{W}_{FWP} = \dot{m}(h_{SP,out} - h_{SP,in}). \tag{59}$$

Enthalpy of condensate exiting the feedwater pumps ($h_{SP,out}$) depends on the isentropic efficiency of the pumps, which is set at $\eta_{FWP} = 0.82$ [29].

$$\eta_{FWP} = \frac{h_{SP,out,ise} - h_{SP,in}}{h_{SP,out} - h_{SP,in}} = 0.82 \tag{60}$$

Modeling of the turbines is a critical step to predict performance accurately. For TES configurations I and II, the maximum mass flow rate through the turbines is higher than in the AP1000 without TES. This change is addressed by establishing new design point pressures and mass flow rates (subscript 'DP') for the HPT and LPT and then adjusting turbine performance during periods of off-design (subscript 'OD') operation when steam flow rates are lower during charging and baseload operation. Stodola's ellipse (Eq. (61)), also referred to as the ellipse law, is applied to calculate the pressures at the inlet and outlet of each turbine section for off-design mass flow rates.

$$\frac{\dot{m}_{OD}}{\dot{m}_{DP}} = \sqrt{\frac{P_{in,OD}^2 - P_{out,OD}^2}{P_{in,DP}^2 - P_{out,DP}^2}} \tag{61}$$

The ellipse law predicts turbine operation without the computational cost of a stage by stage flow calculation [80] and is accurate for as few as five stages [104]. The adjusted isentropic efficiency of the turbines (η_T) is determined using a curve fit of the estimating procedure developed by Bartlett [64].

$$\eta_T = 0.84 - \left(-0.22\left(\frac{\dot{m}_{OD}}{\dot{m}_{DP}}\right)^3 + 0.62\left(\frac{\dot{m}_{OD}}{\dot{m}_{DP}}\right)^2 - 0.62\left(\frac{\dot{m}_{OD}}{\dot{m}_{DP}}\right) + 0.22\right) \tag{62}$$

The assumed design point isentropic efficiency of the HPT and LPT is 0.84 [29]. The enthalpy at the outlet ($h_{SP,out}$) is given by Eq. (63).

$$\eta_T = \frac{h_{SP,in} - h_{SP,out}}{h_{SP,in} - h_{SP,out,ise}} \tag{63}$$

The isentropic outlet enthalpy ($h_{SP,out,ise}$) is fixed by the inlet entropy ($s_{SP,in}$) and the outlet pressure (P_{SP}). It is assumed that the turbines operate for LPT inlet values of $0.3 \leq \frac{\dot{m}_{OD}}{\dot{m}_{DP}} \leq 1$ based on the lower limit for Eq. (62) and the possibility of unstable turbines operation at $\frac{\dot{m}_{OD}}{\dot{m}_{DP}} < 0.3$ [97]. Turbine exit moisture is not allowed to exceed 12% ($\chi \geq 0.88$) to avoid erosion of the turbine rotor [105]. The extraction mass flow rates to the feedwater heaters are adjusted during baseload, charge and discharge so that the enthalpy flows at the extraction points of the turbines are the same as those of the conventional cycle without TES.

$$\dot{m}_{SP,OD} = \frac{\dot{m}_{SP,X,BL} h_{SP,X,BL}}{h_{SP,OD}}. \tag{64}$$

In this expression, the subscript SP is an index for the extraction positions (SPs 9-12, 15, 16). Drain enthalpies of the high- and low-pressure feedwater heaters are held constant at conventional values [29].

The modeling process is initiated by specifying the mass flow rate through the TES ($\dot{m}_{24}$) during discharge. The discharge mass flow rate establishes the DPR. Design points for all sections of the HPT and LPT are determined for configurations I and II in an iterative process. Initial estimates for the design point mass flow rates for each configuration are determined from conservation of mass across the turbine sections during discharge. For configuration I, steam is discharged to the LPT and section S3 is adjusted accordingly:

$$\dot{m}_{S3} = \dot{m}_4 + \dot{m}_{24,I}. \tag{65}$$

For configuration II, the steam mass flow rate is increased in the second section of the HPT:

$$\dot{m}_{S2} = \dot{m}_{S1} - \frac{\dot{m}_1 - \dot{m}_{24,II}}{\dot{m}_1} (\dot{m}_{15} + \dot{m}_{16}) - \dot{m}_{19}. \tag{66}$$

Otherwise the turbine sections mass flow rates are calculated via Eqs. (67)-(73).

$$\dot{m}_{S1} = \dot{m}_2 \tag{67}$$

$$\dot{m}_{S2} = \dot{m}_{S1} - (\dot{m}_{15} + \dot{m}_{16} + \dot{m}_{19}) \tag{68}$$

$$\dot{m}_{S3} = \dot{m}_4 \tag{69}$$

$$\dot{m}_{S4} = \dot{m}_{S3} - \dot{m}_9 \tag{70}$$

$$\dot{m}_{S5} = \dot{m}_{S4} - \dot{m}_{10} \tag{71}$$

$$\dot{m}_{S6} = \dot{m}_{S5} - \dot{m}_{11} \tag{72}$$

$$\dot{m}_{S7} = \dot{m}_{S6} - \dot{m}_{12} \tag{73}$$

The ellipse law (Eq. (61)) is applied to determine the design point pressures of each section of the HPT and LPT. In the first iteration, off-design mass flow rates and pressures are assumed to be the values for the AP1000 without TES given in reference [29]. The state-point values throughout the cycle are then determined from a system level energy balance applied to discharge, baseload and charge modes of operation. The convergence criteria for the energy balance is 10 kW. Isentropic efficiency for each turbine section is calculated using Eq. (62). State point enthalpies exiting the turbines are calculated using Eq. (63). Extractions to the high- and low-pressure feedwater heaters are governed by Eq. (64). Extractions to reheat the steam ($\dot{m}_{1a}$ and $\dot{m}_{19}$) upstream of the LPT are governed by Eqs. (74) and (75).

$$\dot{m}_{1a}(h_{1a} - h_{17}) + \dot{m}_{19}(h_{19} - h_{18}) = \dot{m}_3(h_4 - h_3) \tag{74}$$

$$\frac{\dot{m}_{1a}}{\dot{m}_{19}} = \frac{\dot{m}_{1a,X,BL}}{\dot{m}_{19,X,BL}} \tag{75}$$

The design point mass flow rates are updated for the turbine sections based on the results of the energy balance. The largest mass flow rate into each turbine section over the three modes of operation is the updated design mass flow rate. Design pressures are updated using the ellipse law. This iterative procedure is terminated when the residual (R) between successive determinations (index 'j') of design point mass flow rates is ≤ 1 kg/s.

$$R = \sum_{n=S1}^{S7} \left| \dot{m}_{n,j} - \dot{m}_{n,j-1} \right| \tag{76}$$

The residual is the sum of the absolute difference between successive iterations (subscript 'j') of mass flow rates through seven turbine sections. The process yields values of $\dot{W}_D$, DPR, $\dot{W}_C$, $\dot{W}_{BL}$, $Q_{TES,D}$, $Q_{TES,C}$ and EPR for specified values of $\dot{m}_{24}$, t_C, t_D, η_{RT}. This process is repeated for all values of $\dot{m}_{24}$, t_D, t_C and η_{RT}.

The model is validated by comparison to the model of the Westinghouse AP1000 nuclear plant by Wibisino and Shwageraus [29]. Power of the turbines is within 1% of the prior work. There is no means to validated the model with TES, but we note that the present model yields nearly identical results to that of Kluba and Field [45] for configuration II.

4.2.4 Conceptual Designs

Conceptual storage modules are illustrated in Fig. 36. Sensible and latent heat storage materials are considered. The temperatures and pressures entering and exiting the TES for each configuration are consistent with the descriptions provided in section 4.2.1. Table 2 lists key thermophysical properties and specific cost (\$ kg^{-1}) of potential storage materials. The listed materials provide a basis for comparison and are not intended to be comprehensive.

A single stage TES module is illustrated in Fig. 2(a) for sensible heat storage. Solid materials such as rock, sand and concrete are among the suitable materials. Concrete manufacturing accounts for about 8% of the global emission of carbon dioxide [106]. For this reason, rock is selected. The thermophysical properties of rock listed in Table 2 represent a range of types. Specific heat of rock ranges from 0.6 to 1.2 kJ kg^{-1} K^{-1} [107]–[110]. A specific heat of 0.85 kJ kg^{-1} K^{-1} is assumed. The specific heat of most rock types are clustered within 0.8-0.9 kJ kg^{-1} K^{-1} [107]–[111]. Density of rock varies from 2200 kg

m^{-3} for basalt to 2860 kg m^{-3} for quartzite. A density of 2600 kg m^{-3} is assumed. The void fraction of the rock bed (ϕ) is assumed to be 0.365, which is an idealized value for 0.02 m diameter spherical particles [112]. Cost of rock varies with type and transport distance from the source. A cost of $0.02 per kilogram for crushed rock is assumed based on cost information of [113].

A single stage latent heat storage is considered for configuration II (Fig. 36(b)) because the operating temperature range of the TES is relatively small (50°C). The desired phase change temperature is $230 \leq T_m \leq 245$°C. NaOH:$NaNO_2$ (73:27has a phase transition at 237°C, and heat of fusion of 275 kJ kg^{-1} [72]. Densities and costs of eutectic salt mixtures for latent heat storage are not widely reported. Raud et al. [114] show that density of salt mixtures at the melting point can be estimated with typically less than 3% error based on mole fraction (x_i).

$$\rho = \sum x_i \rho_i \tag{77}$$

The density (ρ_i) is the density of the salt component linearly extrapolated to the melt temperature (T_m). Cost is estimated in the same manner using reported bulk cost of components.

$$c = \sum x_i c_{mat,i} \tag{78}$$

The estimated cost is $0.50 per kilogram based on reported cost of NaOH [115] and $NaNO_2$ [71].

Table 11. Thermophysical properties and cost of storage materials

Material (mol%)	c_p [kJ kg^{-1} K^{-1}]	T_m [°C]	h_{fus} [kJ kg^{-1}]	ρ [kg m^{-3}]	c_{mat} [$ kg^{-1}]
Rock [107]–[110]	0.6 - 1.2	-	-	2200-2860	0.02 [113]
$NaNO_3$:NaOH (18.5:81.5) [68]	-	257	292	2170	0.50
NaOH:$NaNO_2$ (73:27) [72]	-	237	275	2145	0.50
NaOH:KOH (50:50) [72]	-	170	208	2125	0.75

A multistage TES is considered for configurations I and III as illustrated in Fig. 36(c). The conceptual design is similar to the direct steam generation TES systems for concentrating solar thermal power plants [91]. Stages are defined by (A) condensate preheating, (B) evaporation, and (C) steam superheating. Stages A and C are sensible heat storage because of the relatively wide range of operating temperature for preheating condensate and superheating steam. Stage B is latent heat storage with requirement that the storage material has phase transition temperature (T_m) between the saturation temperature of the steam used for charging and the steam generated during discharging. The isothermal, high enthalpic processes of evaporation and condensation of steam match well with latent heat storage.

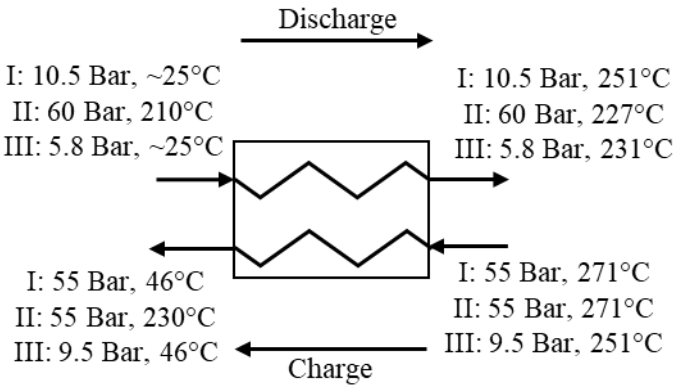

(a)

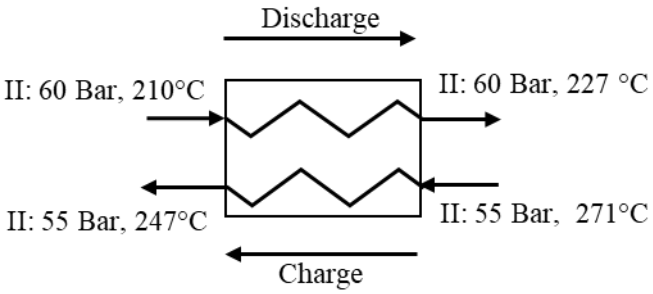

(b)

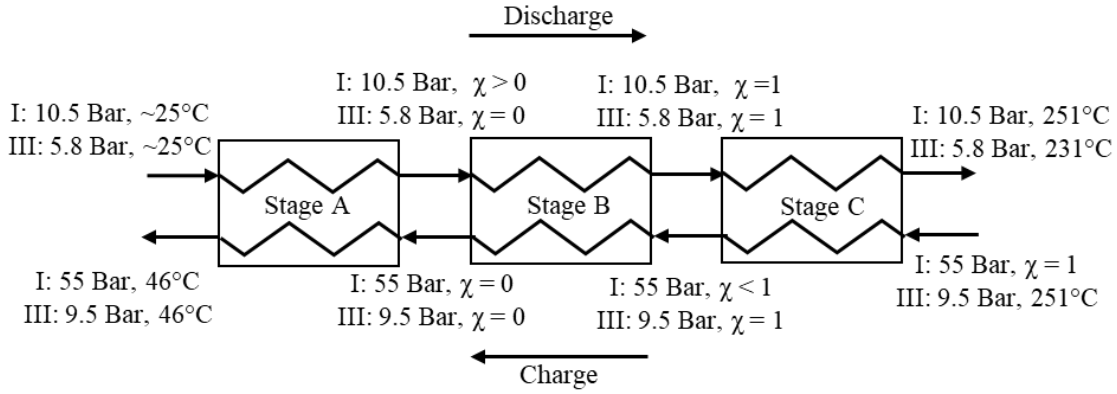

(c)

Fig. 36. Conceptual TES with (a) single stage sensible heat storage (configurations I-III), (b) single stage latent heat storage (II), and (c) multistage storage using sensible and latent heat storage (I and III).

During discharge, water enters stage A at the discharge pressure and temperature and is heated to the saturation temperature. Entering stage B at $\chi = 0$ (or in the case of configuration I, $\chi > 0$), the preheated water is evaporated and exits at $\chi = 1$. Configuration

I requires a material with $182 \leq T_m \leq 271°C$, a range provided by eutectic mixtures of sodium nitrate and sodium hydroxide. A mixture of sodium nitrate and sodium hydroxide with molar fractions of 0.185 and 0.815, respectively ($NaNO_3$:NaOH (18.5:81.5)), has a phase transition at 255°C [68], and heat of fusion of 292 kJ kg^{-1} [68]. Based on current bulk prices [71], [115], the cost of the mixture is $0.50 per kg. Configuration III requires a material with $157 \leq T_m \leq 177°C$. One candidate is an 0.5/0.5 molar mixture of sodium hydroxide and potassium hydroxide (NaOH:KOH (50:50)), which changes phase at 170°C [72] and has a heat of fusion of 208 kJ kg^{-1}. The cost of the mixture is $0.75 per kg based on reported bulk costs of NaOH [115] and KOH [116]. Lithium-nitrate salts have good thermophysical properties for this application but are not considered here due to high cost (> $1 per kg [117]). In stage C, the saturated vapor is heated to the turbine inlet temperature using sensible heat storage. During charging, superheated steam enters stage C. The steam is cooled, entering stage B at $\chi \approx 1$. In stage B, the steam is condensed, and water exits the stage slightly below the saturation temperature. In stage C, the water is cooled to the condenser temperature, 46°C. Both discharge and charge are isobaric processes.

The volume, mass and cost of TES modules are evaluated for each configuration for t_C =4, t_D = 3 hours, and η_{RT} = 0.9 over the range of applicable DPR. The reported values do not include the cost of the container or any auxiliary equipment. The reported values are broken down into single stage (subscript 'ss') and multistage concepts (subscript 'ABC'). The fraction of heat stored in each stage (f_k) is determined by the change in enthalpy for the temperature, pressure and steam quality during charging as shown in Fig. 36.

$$f_k = \frac{h_{k,in} - h_{k,out}}{h_{TES,in} - h_{TES,out}} \tag{79}$$

The subscript ‘k’ refers to the TES stage... The storage capacity equals the energy stored during charging in each stage.

$$Q_{TES,C} = Q_{TES,C}(f_A + f_B + f_C) \tag{80}$$

The mass (m_{TES}) of the storage material is the sum of the mass in each stage.

$$m = m_A + m_B + m_C = \frac{Q_{TES,C}}{u_{ss}} \tag{81}$$

$$m_k = \frac{Q_{TES,C} f_k}{u_k} \tag{82}$$

The specific energy density of latent storage materials (u_{fus}) is given by Eq. (34)

$$u_{fus} = h_{fus} \tag{83}$$

Specific energy density of sensible heat storage is given by Eq. (84).

$$u_s = c_p \Delta T \tag{84}$$

The temperature difference is estimated by assuming a streamwise one-dimensional temperature profile of steam/water in the TES. The change of enthalpy per unit length of the TES is assumed constant. The enthalpy is expressed as a function of the non-dimensional flow length, L = y/*l*, where *l* is the length of the flow passage.

$$h(L) = h_{TES,in} + \left(h_{TES,out} - h_{TES,in}\right)L \tag{85}$$

For the isobaric processes, the temperature profile can be determined from the spatial distribution of enthalpy and the pressure for each configuration. The temperature difference is

$$\Delta T = \int_{L_1}^{L_2} (T_C(h(L), P_C) - T_D(h(L), P_D)\, dL. \tag{86}$$

For a single stage module, the limits of integration are $L_1 = 0$ and $L_2 = 1$. In a multistage module, stages A and C are sensible heat storage. For stage A, the limits of integration are $L_{1,A} = 0$ and $L_{2,A} = f_A$. For stage C, the limits of integration are $L_{1,C} = (1 - f_C)$ and $L_{2,C} = 1$.

The estimated total storage volume, including the void space in the packed rock bed is given by Eq. (87).

$$V = \frac{m_A}{\rho_A(1-\phi)} + \frac{m_B}{\rho_B} + \frac{m_C}{\rho_C(1-\phi)} = \frac{m_{ss}}{\rho_{ss}(1-\phi)} \tag{87}$$

The cost of the storage material (C) is given in Eq. (88).

$$C = m_A c_{mat,A} + m_B c_{mat,B} + m_C c_{mat,C} = m_{ss} c_{ss} \tag{88}$$

The cost per kilowatt hour (electric) is given in Eq. (89).

$$c = \frac{C}{\eta_D Q_{TES,C}} \tag{89}$$

The discharge efficiency (η_D) is the conversion efficiency from stored heat to electrical energy.

$$\eta_D = \frac{t_D \dot{W}_{X,BL}(DPR-1)}{Q_{TES,C}} \tag{90}$$

4.3 Results

Diurnal energy production ratio (EPR) is presented first for a case study using operating scenarios, specifically charge and discharge durations, identified as economically favorable by prior analyses of the value of electricity storage in arbitrage markets in U.S. markets presented by Sioshansi et al. [44] and Bradbury et al. [42] and in the Australian wholesale market by McConnell et al. [43].In Section 4.3.2, EPR is presented over the full range of charge and discharge durations considered. In Section 4.3.3, the size and cost of TES material options are estimated and compared for representative values of DPR and charge/discharge durations.

4.3.1 Case Study

Figure 37 shows the diurnal EPR, which encompasses charge, discharge and baseload operation, versus DPR for two charge/discharge durations equal to $t_C = 4/t_D = 3$ hours and $t_C = 8/t_D = 6.5$ hours. Round-trip efficiency (η_{RT}) of the TES is 0.9 in these plots

and based on prior work on thermal storage for solar power plants [103], this value can be achieved for sensible storage at a large scale. The EPR is unity without TES (DPR = 1) and decreases with increasing DPR for all configurations and both charge/discharge durations. The decrease in EPR with increasing DPR is due to the penalty of off-design operation during charge and baseload operation. The change in the design point of the turbines becomes larger as DPR is increased. The choice of DPR in practice will depend on the economic value of providing higher peaking power and more flexible operation of the baseload power plant to improve capacity factor and increased use of VRE. The mix of generation sources and pricing in the utility grid will impact this choice. The maximum DPR is limited by the mass flow rate of steam that can be diverted to the TES during charge. The maximum rate at which TES can be charged ($\dot{Q}_{TES,C}$) is set by the minimum mass flow rate through a turbine. In the present work, the minimum flow rate is set to 30% of the design point mass flow rate to avoid unstable turbine operation [97].

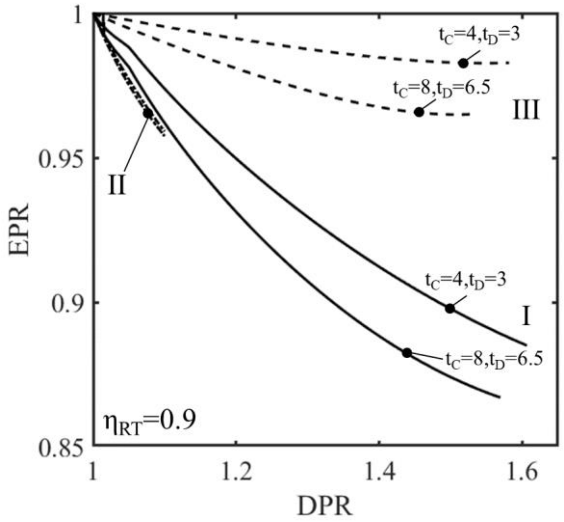

Fig. 37. Diurnal EPR vs DPR for $t_C = 4/t_D = 3$ and $t_C = 8/t_D = 6.5$ hours and $\eta_{RT} = 0.9$ for configuration I (solid lines), II (dashed lines) and III (dash-dot lines).

For configuration I, EPR versus DPR curves are identical for the single and multiple stage TES options because the inlet and outlet conditions of the TES are identical. The discussion focuses on DPR = 1.2, corresponding to the target peaking power for next generation nuclear reactors with storage set by Westinghouse [89]. At DPR = 1.2, EPR = 0.95 for $t_C = 4/t_D = 3$ hours, and EPR = 0.93 for $t_C = 8/t_D = 6.5$ hours. The EPR is higher for shorter charge/discharge durations because the HPT and LPT operate closer to the design point mass flow rate during charging. The upper limit of DPR for the two charge/discharge durations are comparable (1.61 for $t_C = 4/t_D = 3$ hours vs. 1.57 for $t_C = 8/t_D = 6.5$ hours). At the respective upper limits of DPR, EPR = 0.89 for $t_C = 4/t_D = 3$ hours, and EPR = 0.87 for $t_C = 8/t_D = 6.5$ hours. To illustrate the benefit of shorter charge/discharge cycles, Figs. 38 and 39 show the power during baseload ($\dot{W}_{BL}$) and charging ($\dot{W}_C$) relative to the baseload power of the AP1000 without TES ($\dot{W}_{X,BL}$). At DPR = 1.2, $\dot{W}_{BL}/\dot{W}_{X,BL} = 0.96$. During charging, $\dot{W}_C/\dot{W}_{X,BL} = 0.70$ for $t_C = 4/t_D = 3$ hours, and $\dot{W}_C/\dot{W}_{X,BL} = 0.67$ at $t_C = 8/t_D = 6.5$ hours. The value of $\dot{W}_C$ depends on η_{RT}, t_C and t_D because

these parameters determine the mass flow rate of steam diverted to the TES during charging.

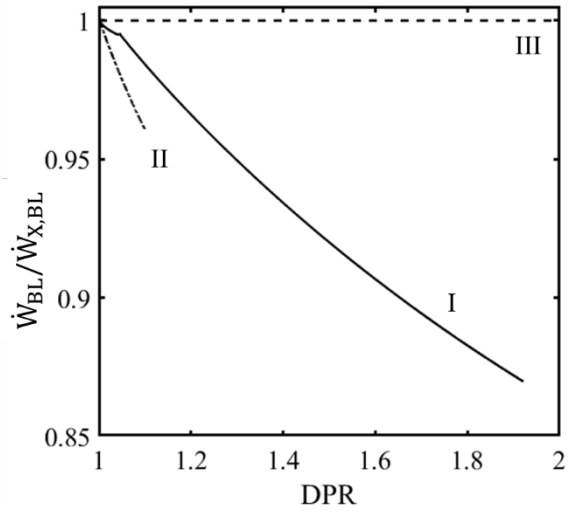

Fig. 38. Normalized baseload power ($\dot{W}_{BL}/\dot{W}_{X,BL}$) vs DPR for configuration I (solid lines), II (dashed lines) and III (dash-dot lines).

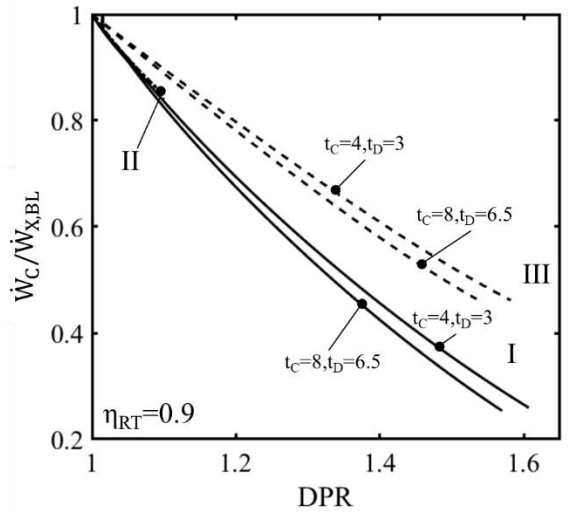

Fig. 39. Normalized charging power ($\dot{W}_C/\dot{W}_{X,BL}$) vs DPR for t_C = 4/t_D = 3 and t_C= 8/t_D = 6.5 hours and η_{RT} = 0.9 for configuration I (solid lines), II (dashed lines) and III (dash-dot lines).

Next consider configuration II. The outlet temperature of the TES is 230°C for sensible heat storage and 247°C for latent heat storage. This difference has a minor impact on EPR and thus the discussion focuses on lower cost sensible heat storage. At the upper limit of DPR = 1.1, EPR = 0.95 with latent heat storage and EPR = 0.96 with sensible heat

storage. Kluba and Field [45] report an upper limit of DPR = 1.08 for the APR1400. The mass flow rate of steam that can be added to the HPT and LPT during discharge is limited by the mass flow rate that would have been extracted to the feedwater heaters during baseload without TES. For the range of DPR over which configuration II can be operated, EPR is slightly lower than that of configuration I because of a larger penalty on baseload operation due to more significant changes to the design points of the turbines. At DPR = 1.1, $\dot{W}_{BL}/\dot{W}_{X,BL}$ = 0.96, compared to 0.98 for configuration I. During charge, $\dot{W}_{C}/\dot{W}_{X,BL}$= 0.85 for configuration II compared to 0.84 for configuration I.

Configuration III provides the highest EPR due to high efficiency during baseload and charging operation. There is no change to the design point, i.e. $\dot{W}_{BL}/\dot{W}_{X,BL}$= 1 for all DPR. At DPR = 1.2, EPR = 0.99 for $t_C = 4/t_D = 3$ hours, and EPR = 0.98 for $t_C = 8/t_D$ = 6.5 hours. The value of $\dot{W}_{C}/\dot{W}_{X,BL}$ is higher than for configurations I and II because only the LPT is bypassed during charging. At DPR = 1.2, $\dot{W}_{C}/\dot{W}_{X,BL}$=0.80. The upper limit of DPR is 1.56 for $t_C = 4/t_D = 3$ hours.

Figure 40(a) and (b) shows the impact of round-trip efficiency of the TES on EPR for (a) $t_C = 4/t_D = 3$ hours and (b) $t_C = 8/t_D = 6.5$ hours. With higher round-trip efficiency EPR increases and the storage capacity ($Q_{TES,C}$) decreases for a specified DPR. With higher round-trip efficiency less steam must be diverted during charging and thus the turbines operate closer to the design point. The upper limit on DPR increases with increasing η_{RT} because the rate of discharge ($\dot{Q}_{TES,D}$) is faster for the same t_D. First consider $t_C = 4/t_D = 3$ hours at DPR =1.1. For configuration I, EPR increases from 0.97 to 0.98 as η_{RT} is increased from 0.7 to 1. The EPR of configuration II increases from 0.95 to 0.96. The EPR of configuration III increases from 0.99 to near unity. At DPR=1.2, EPR of configuration I

increases from 0.94 to 0.96, and EPR of configuration III increases from 0.98 to 0.99. For the longer charge/discharge duration, shown in Fig. 40(b), the benefit of increasing the round trip efficiency on EPR is slightly greater in terms of percent increase but the EPR is lower.

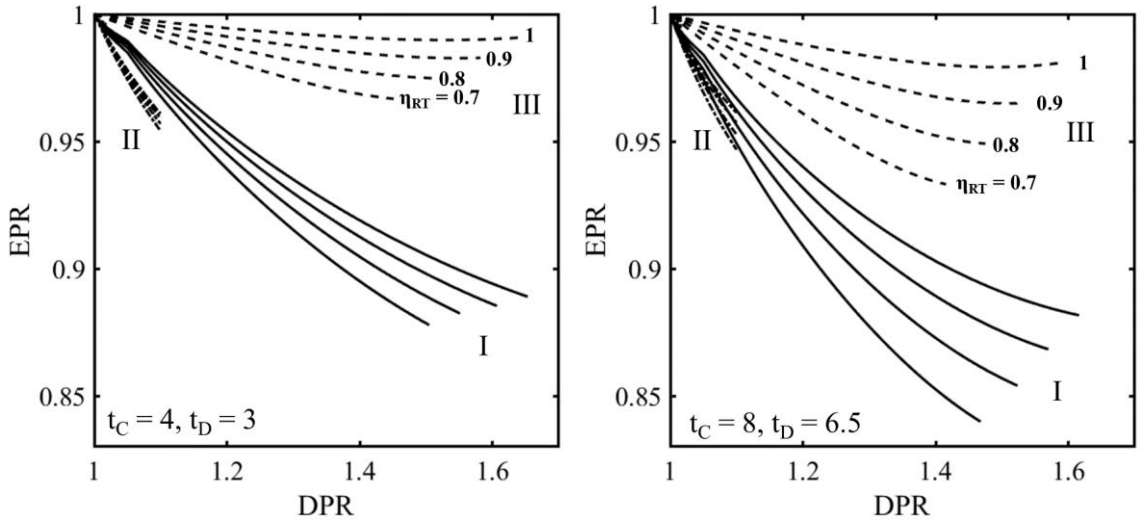

(a) (b)

Fig. 40. EPR vs. DPR for η_{RT}=0.7, 0.8, 0.9 and 1 for configuration I (solid lines), II (dashed lines) and III (dash-dot lines) for (a) t_C = 4/t_D = 3 hours and (b) t_C = 8/ t_D = 6.5 hours.

4.3.2 Effect of Charge and Discharge Durations

Figure 41(a)-(d) shows EPR versus DPR for t_C = 2, 4, 7 and 10 hours, t_D equal to (a) 2, (b) 4, (c) 7 and (d) 10 hours and η_{RT} = 0.9. Figure 8shows a subset of these data to better visualize the impact of discharge duration on EPR for (a) t_C = 4 and (b) 10 hours. Consistent with the results of the case study, EPR increases as charge and discharge durations are decreased for configurations I and III. The EPR for configuration II changes very little over the considered range of t_C and t_D. However, this configuration is distinct because the baseload operation is heavily penalized by off-design operation of the turbines. Thus, with exceptionally long charge/discharge durations, for example for t_C = 8/t_D = 15 hours as considered by Kluba and Field [45], the EPR of configuration II is slightly higher

than that of configuration I. However, long charge and discharge durations are unlikely to provide the best economic case for nuclear energy with storage. The only drawback of very short charge duration is a lower ceiling on DPR. A DPR of 1.2 can be reached for configurations I and III with charging durations as short as 2 hours.

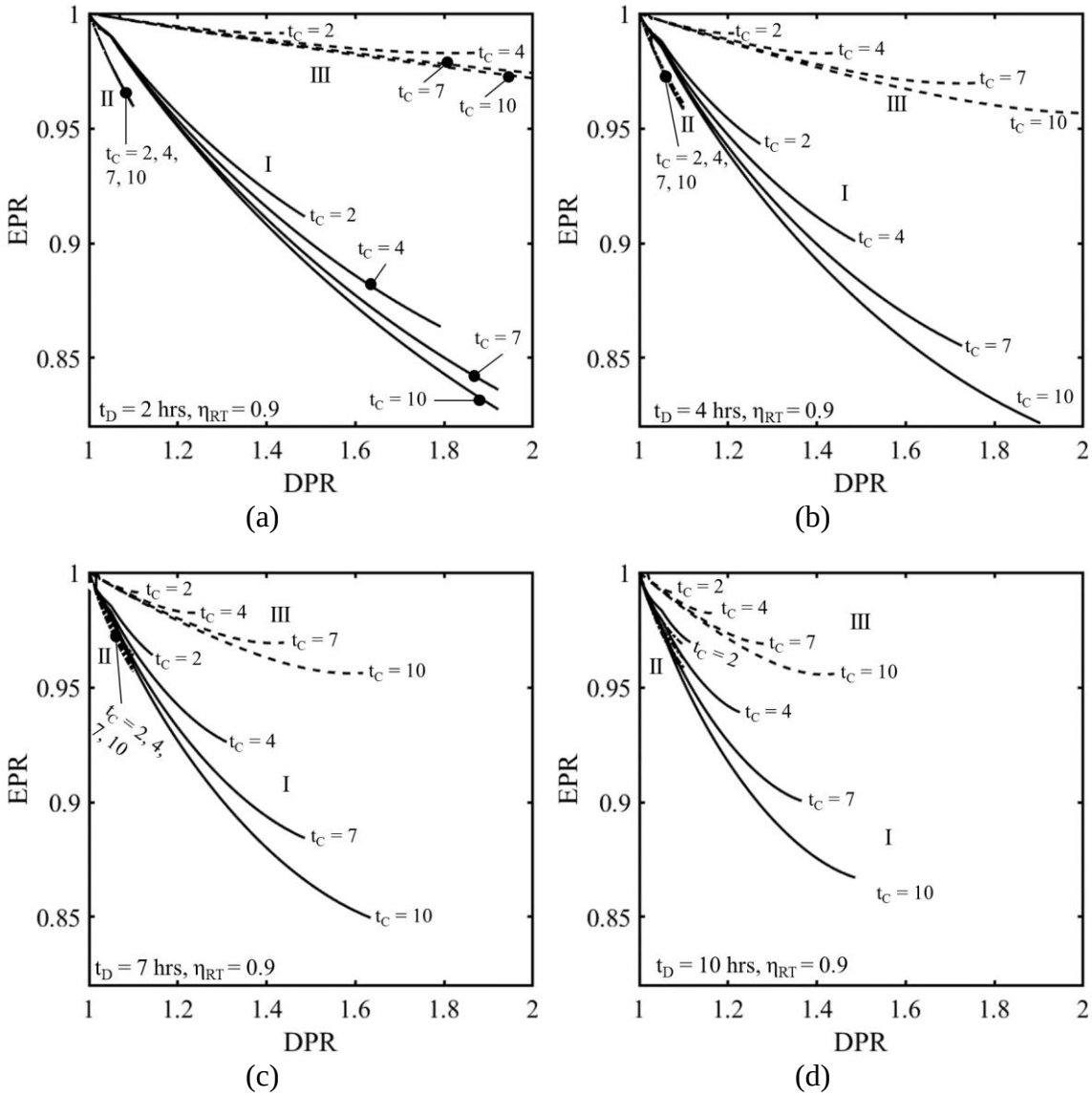

Fig. 41. Impact of charge/discharge duration: EPR vs. DPR for t_D equal to (a) 2, (b) 4, (c) 7 and (d) 10 hours at t_C = 2, 4, 7 and 10 hours.

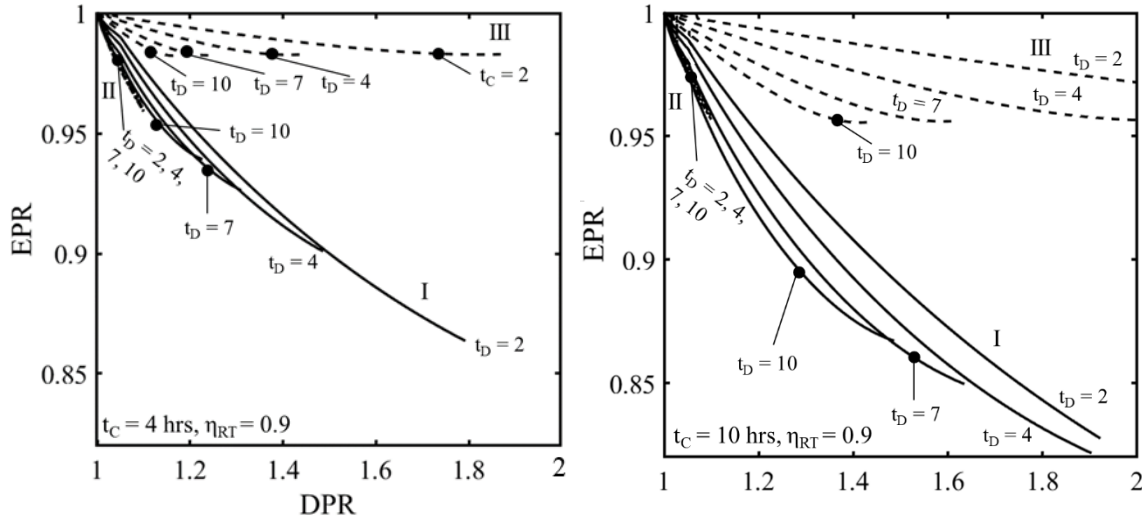

(a) (b)

Fig. 42. Data from Fig. 41 replotted to emphasize the impact of discharge duration. EPR versus DPR for t_D = 2,4,7 and 10 hours for t_C equal to (a) 4 and (b) 10 hours.

4.3.3 Thermal Energy Storage Material Volume and Cost

Figure 43 shows total (a) storage capacity, (b) volume, (c) mass and (d) cost of the storage material versus DPR for each configuration. The values are presented for scenarios that might be encountered in practice: t_D = 3 hours and η_{RT} = 0.9. The results are independent of the charge duration. Tables 12 (single stage) and 13 (multistage) list the data for DPR = 1.1 and DPR = 1.2. Configuration II requires the lowest storage capacity ($Q_{TES,C}$) at DPR = 1.1 because η_D = 0.3 compared to $\eta_D \approx 0.2$ for configurations I and III. For both sensible and latent heat storage, $Q_{TES,C}$ = 950 $MWh_{th.}$ But configuration II is restricted to DPR ≤ 1.1. At DPR = 1.2, $Q_{TES,C}$ is 3000 MWh_{th} for configuration I and 3160 MWh_{th} for configuration III. For the multistage options, stage A used for condensate preheating provides 38% of the total storage capacity for configuration I ($f_{I,A}$=0.38) and 20% for configuration III ($f_{III,A}$ = 0.20). These fractions equate to 1140 MWh_{th} and 640 MWh_{th} at DPR = 1.2. Stage B stores the largest fraction of heat with $f_{I,B}$=0.56 and $f_{III,B}$=0.73 corresponding to 1680 MWh_{th} and 2310 MWh_{th} at DPR = 1.2. Configuration III has a larger

fraction of heat storage in stage B because the steam used for charging is superheated. In configuration I stage C is charged using condensing steam. Stage C provides the lowest fraction of storage capacity: $f_{I,C}$=0.06 and $f_{III,C}$=0.07 corresponding to 180 MWh_{th} and 210 MWh_{th} at DPR = 1.2. Stage C is essential because superheating the steam at discharge allows for higher discharge pressures to maintain turbine outlet quality greater than 0.88.

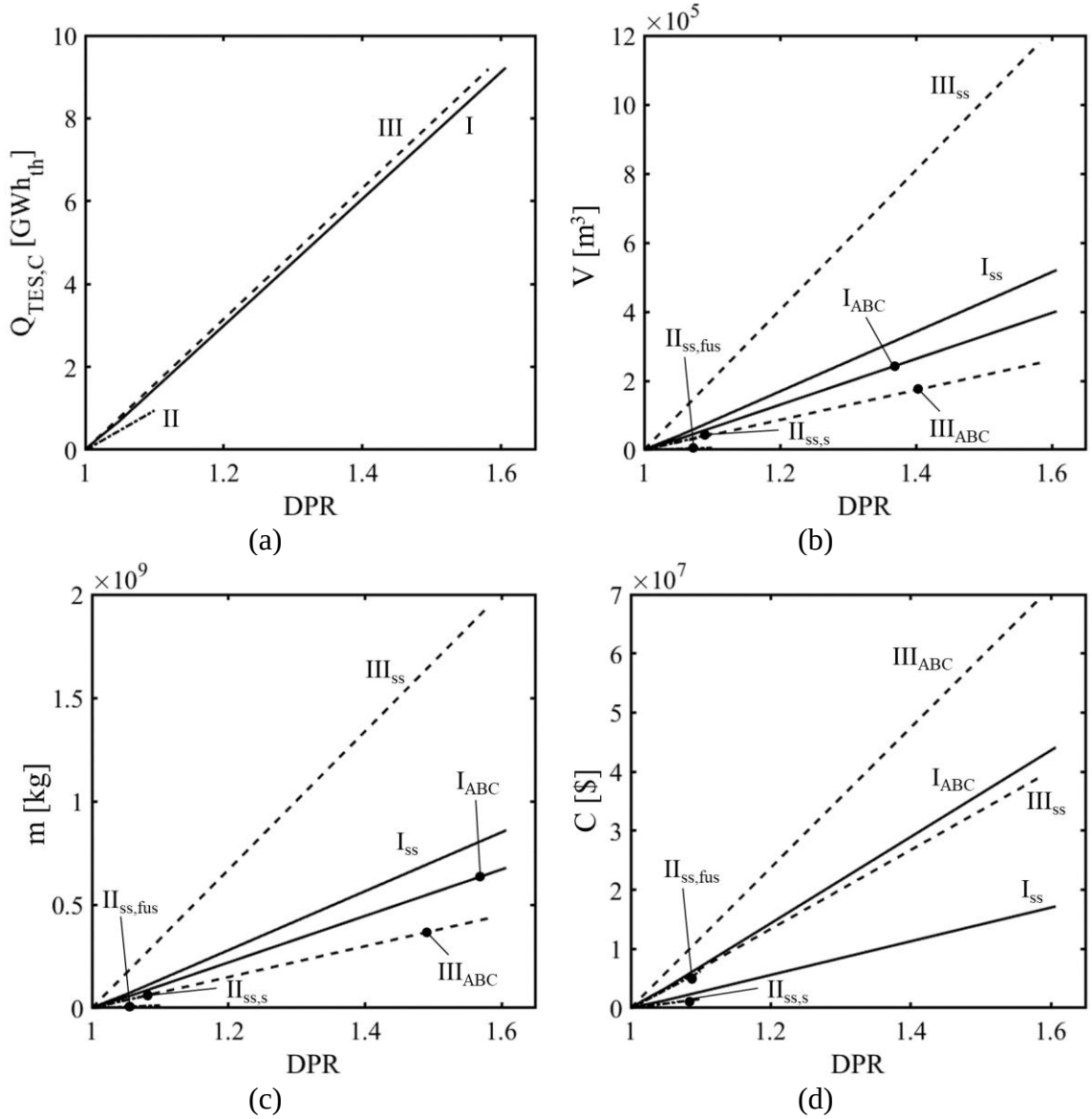

Fig. 43. The TES (a) volume, (b) mass and (c) cost of TES storage material for configurations I-III for cases of t_C = 4/t_D = 3 hours and η_{RT} =0.9 given TES concepts using sensible heat storage and latent heat storage.

Table 12. Single stage TES storage capacity, volume, mass and cost of storage materials for configurations I-III using sensible and latent heat storage.

	DPR = 1.1				DPR = 1.2	
	I_{ss}	II_s	II_{fus}	III_{ss}	I_{ss}	III_{ss}
EPR [-]	0.97	0.96	0.95	0.99	0.95	0.99
$Q_{TES,C}$ [MWh_{th}]	1470	950	950	1580	3000	3160
ΔT[°C]	63	53	-	20	63	20
V [m^3] (10^3)	82.8	46.3	5.8	202.7	169.3	405.4
m [kg] (10^6)	137	76	12	335	280	669
C [$] ($10^6$)	2.73	1.53	6.21	6.69	5.59	13.39
c [$ kWh_e^{-1}]	8.69	4.87	19.77	21.30	8.89	21.30

Table 13. Individual stage and total TES storage capacity, volume, mass and cost of storage materials for configurations I-III.

		DPR = 1.1		DPR = 1.2	
		I_{ABC}	III_{ABC}	I_{ABC}	III_{ABC}
Stage A	Q_A [MWh_{th}]	560	320	1140	640
	ΔT[°C]	26	20	26	20
	f_A [-]	0.38	0.20	0.38	0.20
	V_A [m^3] (10^6)	55.1	31.7	112.4	63.4
	m_A [kg] (10^6)	91	52	186	105
	C_A [$] ($10^6$)	1.82	1.05	3.71	2.09
Stage B	Q_B [MWh_{th}]	820	1150	1680	2310
	f_B [-]	0.56	0.73	0.56	0.73
	V_B [m^3] (10^6)	4.6	6.6	9.5	13.2
	m_B [kg] (10^6)	10	14	21	28
	C_B [$] ($10^6$)	5.07	10.67	10.35	21.33
Stage C	Q_C [MWh_{th}]	90	110	180	210
	ΔT [°C]	55	20	55	20
	f_B [-]	0.06	0.07	0.06	0.07
	V_B [m^3] (10^6)	4.1	5	8.5	10
	m_B [kg] (10^6)	7	8	14	16
	C_C [$] ($10^6$)	0.13	0.32	0.28	0.33
Total	EPR [-]	0.97	0.99	0.95	0.99
	$Q_{TES,C}$ [MWh_{th}]	1470	1580	3000	3160
	V [m^3] (10^6)	63.8	43.3	130.1	86.6
	m [kg] (10^6)	108	74	221	149
	C [$] ($10^6$)	7.02	12.04	14.34	23.75
	c [$ kWh_e^{-1}]	22.35	38.24	22.82	37.80

The volume of the storage material (including the void space in the rock bed) is plotted in Fig. 9(b). Single stage options are indicated by the subscript 'ss'. Multistage options are denoted with the subscript 'ABC'. At DPR = 1.1, V = 82.8 $(10)^3$ m^3, 46.3 $(10)^3$ $m^3$and 202.7 $(10)^3$ m^3 for configurations I-III using sensible heat storage (rock). Latent heat storage can only be used in a single stage for configuration II. In this case, the total volume is reduced to 5.8 (10^3) m^3. At DPR = 1.2, V = 169.3 $(10)^3$ $m^3$and 405.4 $(10)^3$ m^3 for sensible storage for configurations I and III. The volume of the multistage concept is 23% and 80% less for configurations I and III. The percent reduction in volume is more for configuration III due the greater fraction of heat stored in latent heat in stage B than in sensible heat in stages A and C.

Based on the cost of the storage material, configuration II with rock storage is the least expensive option for DPR = 1.1. The mass of rock for configurations I, II and III is 137(10^6), 76(10^6), and 335(10^6) kg, respectively, with corresponding material costs of \$2.73 (10^6), \$1.53 (10^7) and \$6.69(10^6). Use of NaOH:$NaNO_2$ (73:27) in a single stage TES for configuration II reduces the mass by 85% to 12 (10^6) kg, but triples cost to \$6.21 (10^6). Likewise, multistage TES modules, which combine rock and salt storage for configurations I and III, weigh less but cost more than use of rock in configuration II. At DPR = 1.2, configuration II cannot be used, but rock remains the low cost option for configurations I and III. The mass of rock in a single stage TES module is 280(10^6) kg for configuration I and 669 (10^6) kg for configuration III, double the mass at DPR = 1.1. Cost is likewise double for the higher DPR. Use of multistage TES modules at DPR = 1.2 are again more expensive due to the cost of the eutectic salt mixtures. Configuration I weighs

221 (10^6) kg and costs \$14.34 (10^6) whereas configuration III weighs 149 (10^6) kg and costs \$23.75 (10^6), due to the use of higher cost salts.

The storage cost per kilowatt hour electric (c) is a useful metric to compare TES with other storage technologies. As listed in Table 12, for DPR = 1.1, the single stage modules have material costs for rock of \$8.69, \$4.87 and \$21.30 per kWh_e with similar costs at higher DPR. For latent heat storage for configuration II in a single stage module, c = \$19.77 per kWh_e. For the multistage concepts, c = \$22.35 and \$38.24 per kWh_e. For comparison pumped hydro storage and lithium ion batteries have reported costs of \$5-100 and \$600-2500 per kWh_e, respectively[12].

4.4 Discussion

Configuration III provides the highest EPR and thus the greatest degree of flexibility for nuclear power and the expansion of renewable energy sources in the power grid. Discharge of the TES through a secondary cycle allows the primary Rankine cycle to operate at no loss of efficiency during baseload and charging operation. Configuration I and II both discharge the TES to the primary Rankine cycle and thus require enlarging the turbines, which then operate off-design and less efficiently in baseload and charging operation. At DPR = 1.2, which is the peaking power target of Westinghouse for thermal energy storage, configuration III has an EPR of 0.99 for charge duration of four hours, discharge over three hours, and ratio of discharged to charged energy of 0.9. This operating scenario has been projected to be a cost effective in economic studies of energy storage with nuclear energy in various power grids assuming an arbitrage market. In comparison, configuration I has an EPR of 0.95, which for a large power plant represents a meaningful reduction in capacity. Configuration II is restricted to DPR less than 1.1, or 10% peaking power. Like configuration I, it requires substantial changes to both the high- and low-

pressure turbines. Its primary benefit is the storage volume required is lower than the other configurations, albeit to the detriment of EPR and only for low DPR.

Sensible heat storage is less expensive than latent heat storage. The narrow range of phase transition temperatures for this application limits the latent heat storage materials to relatively expensive salt mixtures, which are double the cost of rock. The only benefit of latent heat storage is a reduction of volume by up to 80%. The volume of a rock bed to provide a DPR of 1.1 for a discharge duration of three hours and TES round trip efficiency of 0.9 would be about 82.8 (10^3) m^3, 46.3 (10^3) m^3 and 202.7 (10^3) m^3 for configuration I-III, respectively. To provide context, a 1000 MW_e nuclear power plant typically utilizes about 75 (10^3) m^3 of concrete for construction and the total volume of the power plant is approximately 340 (10^3) m^3 [118]. Based on these results, configuration III with sensible heat rock storage is a promising option for additional study.

The present study applies the simplifying assumption of a conceptual TES with constant rates of charge and discharge. The cost analysis is confined to the cost of storage material. The economic tradeoff on investment rate of return between high EPR and the capital costs of adding TES and a secondary cycle is a consideration for future work as storage is planned for specific power grids. Moreover, the TES designs presented in the present study are conceptual. Detailed designs supported by transient modeling of heat transfer, with consideration of the complexities on the steam side of the TES, are a next step toward consideration of the practical (for example ramping rates and round-trip efficiency) and economic benefits of TES versus other storage options.

4.5 Conclusion

To guide the path toward use of thermal energy storage for utility-scale storage coupled with baseload nuclear power plants, the present study presents the first parametric

study of the thermodynamic performance and cost of various approaches to integrated TES integrated with a 1050 MW_e nuclear power plant. The results demonstrate how TES can be used to provide peaking power and flexibility of baseload power and still maintain reasonably high capacity factor, as quantified by the diurnal energy production ratio (EPR). Higher values of EPR are expected to correlate closely to economic viability of the TES and nuclear power plant system. The analysis considers a broad range of operating parameters to characterize how the configurations would perform in utility grids for which load management and the use of VRE sources vary. The impacts of discharge power up to twice the rated power of a conventional plant, charge and discharge durations from 2 to 10 hours and round-trip efficiency of the TES from 0.7 to 1 on the diurnal Energy Production Ratio (EPR) are presented. A thermodynamic model of each TES configuration is applied to the Westinghouse AP1000 nuclear power plant. The comparative results are valid for other nuclear power plants operating at similar temperatures and pressures, including the APR1400 considered by Kluba and Field [45].

The design options are distinguished by the method of charging and discharging the TES. Configuration I charges the TES using high-pressure steam and discharges steam to the LPT to provide peaking power. Configuration II charges the TES in the same way but discharges preheated condensate to the steam generator. Configuration III charges the TES using low-pressure steam and discharges to a secondary Rankine cycle. Both configuration I and II require modification to the high- and low-pressure turbines in the primary cycle to handle higher flow rates during charging.

The thermodynamic performance is storage material agnostic, but size, volume and cost of are not. Configuration III provides the highest diurnal EPR of the options considered

and is the only configuration which has no detrimental impact on the efficiency of baseload operation. Configurations I and III can be operated over a wide range of discharge power. On the other hand, configuration II is limited to discharge power of 110% of baseload power. This limitation along with lower EPR is likely to restrict the economic value of this option in an arbitrage market especially for utilities with high penetration of renewable energy.

The cost of storage material is low relative to the cost of a nuclear plant but is a consideration when selecting materials and comparing TES to other storage options. The required storage capacity increases with increasing DPR, discharging duration and decreasing round-trip efficiency of the TES. A rock bed is the lowest cost material and is relatively simple compared to the multistage TES concepts that use a combination of rock and eutectic mixtures of salt. Latent heat storage materials reduce the volume and mass of the TES but at DPR = 1.2 double the material costs based on bulk pricing for eutectic salt mixtures with appropriate melt temperature. Both storage options are considerably less costly than lithium ion batteries on a per kWh_e basis.

The degree to which a TES with nuclear power is economically favorable and reduces the emission of greenhouse gases will depend on grid operation, including resource mix, consumer demand and regulatory structure. The EPR versus DPR data presented here can be included in utility scale optimization models to account for the impact of TES on operation of a nuclear plant. Such an approach would provide improved predictions of internal rate of return of storage over past work which has assumed that integration of thermal storage does not impact the efficiency of the nuclear Rankine power cycle.

5 Conclusion

Thermal energy storage (TES) can increase the flexibility of baseload nuclear power plants to provide load reduction during periods of over generation and peaking power during periods of under generation. In this manner, TES supports the integration of variable renewable energy sources in the power grid. The overall objective of the work reported in this dissertation is to propose and characterize the performance of approaches to integrate TES with nuclear power and to recommend options for further study. Characterization is accomplished with a component level thermodynamic model of a modern 1050 MW_e nuclear power plant with TES. The modeling study is the first reported in the scientific literature and provides a technical assessment of how TES impacts the performance of the plant for a variety of integration options and ranges of key operating parameters. The TES is treated as a black box and a round-trip efficiency is applied to capture inherent losses between charging and discharging. Sensible and latent heat storage materials in conceptual single and multistage TES modules are considered. Thermal energy storage in this application requires heat storage at temperatures from 46°C to 271°C. For latent heat storage materials, phase transition temperatures are needed in the range 160°C $\leq T_m \leq$ 270°C. Latent heat storage materials are used for the isothermal processes of condensation during charging and evaporation during discharging. The phase transition temperature must be less than the saturation temperature of the steam used for charging and greater than the saturation temperature of steam generated during discharge. This range of melt temperatures restricts the choices of available latent heat materials to sodium hydroxide-based salts. Solid phase sensible heat storage materials such as rock are capable of operating over the full range of temperatures and are significantly less expensive.

Proposed options for TES integration with a nuclear power plant are compared based on the diurnal energy production ratio (EPR) versus discharge power ratio (DPR). The EPR is the ratio of energy generated with TES and the energy that would have been generated by the plant without TES. The EPR reflects the impact of TES on the capacity factor and efficiency of the plant during charging, discharging and baseload operation. Without TES, EPR =1. With TES, EPR is less than unity with a higher fraction representing more efficient operation of the plant. The DPR is the ratio of power generated during TES discharge and the power generated in baseload without TES. It is a reflection of the degree of flexibility.

The placement of TES within the cycle is referred to as the configuration. A number of configurations were considered in the work reported in Chapters 2 and 3 [46], [48]. Based on capacity factor over a charge/discharge cycle at DPR = 1.1, three configurations were down selected for the parametric study reported in Chapter 4. The Westinghouse Electric Company has a goal of DPR = 1.2 for near term implementation of TES with nuclear power [25]. The present study considers DPR up to two to address the possibility of adding greater storage capacity in the future. Based on economic studies of generic energy storage devices operating in real electrical grids [42]–[44], charge and discharge durations ranges are considered from 2 to 10 hours. TES round-trip efficiencies range from an idealized value of unity, in order to place an upper bound on operation, down to 0.7, consistent with the range of heat cycle efficiencies [12]. Round-trip efficiencies of TES as high as 0.95 have been demonstrated for a 105 MWh_{th} pilot scale sensible heat molten salt storage with concentrating solar power [81].

Configuration I, proposed by the author, charges the TES with high-pressure steam from the conventional steam generator. During discharge of the TES, steam is generated using stored heat from an external water store and expanded in the low-pressure turbine for peaking power. Configuration II, proposed by Kluba and Field [45], is charged in the same manner. To discharge the TES, condensate is redirected from the high-pressure feedwater heater to the TES to preheat condensate for the steam generator. Steam typically used for condensate preheating is expanded in the high- and low-pressure turbines. Configuration III, proposed by the author, charges the TES with steam diverted upstream of the low-pressure turbine. Discharge of the TES is via a secondary cycle.

Configurations I and III provide peaking power requirements as high as approximately DPR = 1.6 for likely charge and discharge durations and thus provide the greatest degree of flexibility for expansion of renewable energy sources in the power grid. The limits on DPR increases with increasing charge duration, decreasing discharge duration and increasing TES round-trip efficiency. Configuration III has the highest EPR of all configurations at all operating conditions. The EPR increases with decreasing charge duration, DPR and increasing round-trip efficiency. Conversely, EPR decreases with increasing discharge duration and decreasing round-trip efficiency. These trends hold for all configurations to varying degrees. This advantage of high EPR for configuration III is due to more efficient operation of the plant with discharge through a secondary cycle because no changes to the primary cycle are needed. Configurations I and II both require modification of the primary cycle, specifically to the high- and low-pressure steam turbines. There could be an economic tradeoff of modification of the primary cycle turbines or addition of a secondary cycle. There is also an economic tradeoff between

achieving high EPR and the cost of storage material. For example, at DPR = 1.2, round trip efficiency equal to 0.9, and charge and discharge durations of 4 and 3 hours, configuration III yields EPR = 0.99 with a cost of storage material of \$21.30 per kWh_e for a rock bed storage unit. In comparison, configuration I yields EPR = 0.95 with a cost of storage of \$8.89 per kWh_e. These economic tradeoffs can be addressed in future work for specific power grids.

Configuration II is restricted to DPR less than 1.1 and has the most limited use. Unlike configuration I and III there is no change to DPR with changes in charge duration, discharge duration and round-trip efficiency. Configuration II, like configuration I, requires changes to both the high- and low-pressure turbines. Even at such low discharge power, configuration II provides a substantially lower EPR (0.96) compared to configuration III (>0.99). Configuration II requires a smaller storage capacity compared to configurations I and III at low discharge power. The required storage capacity of configuration II is 950 MWh_{th} versus 1470 MWh_{th} and 1580 MWh_{th} for configurations I and III, respectively for a discharge duration of 3 hours, DPR = 1.1 and $\eta_{RT} = 0.9$. The significantly lower storage capacity is because the discharge efficiency, defined as efficiency at which stored thermal energy is converted to electrical energy, is 0.3 versus 0.2. The cost of storage material for configuration II is \$4.87 per kWh_e compared to \$8.89 per kWh_e for configuration I and \$21.30 per kWh_e for configuration III for all discharge durations, DPR and a round-trip efficiency of 0.9. The difference in cost of storage materials between configurations I and III, which have similar discharge efficiencies, is due to the difference in temperature between charge and discharge. A larger temperature difference between charge and discharge increases energy density. The temperature and

pressure for discharge of configuration III was chosen as 231°C and 5.8 Bar to maximize the first and second law efficiency of the secondary cycle. As a result, the difference of temperature between charge and discharge is 33°C degrees less than that of configuration I.

Sensible heat storage is the least expensive option for the storage temperatures required for nuclear power plants. The use of latent heat storage materials either in single (II) or multistage configuration (I and III) is considered for mixtures of sodium nitrate and sodium hydroxide (I), sodium hydroxide and sodium nitrite (II) and sodium hydroxide and potassium hydroxide (III). These salts at least double the cost of the storage material compared to rock. For a TES round-trip efficiency of 0.9, the salt mixtures cost $22.82, $19.77 and $37.80 per kWh_e for configurations I-III, respectively. The narrow range of phase transition temperatures for this application restricts the viable latent heat storage materials to these expensive salts unless new materials such as melt-temperature tuned nanomaterials, such as those developed by the Stein group at the University of Minnesota [47], or other new materials become available. Even considering the costs of latent heat storage materials, costs of storage materials are less than $40 per kWh_e for all configurations. A full comparison of storage cost of TES and apples to apples comparison to other storage technologies is addressed in the future work section.

The volume of a rock bed to provide a DPR of 1.1 for a discharge duration of three hours would require 82.8 (10^3) m^3, 46.3 (10^3) m^3 and 202.7 (10^3) m^3 for configurations I-III, respectively, assuming a round-trip efficiency of 0.9. To provide context, a 1000 MW_e nuclear power plant typically utilizes about 75 (10^3) m^3 of concrete during construction and the total volume of the power plant is approximately 340 (10^3) m^3 [118]. The volume

of an Olympic size swimming pool (50m by 25m with 2m depth) is 2500 m^3. Although more expensive, (but still less than other storage methods) concerns with the large volumes could be eased by the use of latent heat storage materials could reduce the total volume up to 80%. Ultimately, the use of latent heat storage materials depends on the location of the power plant, the availability of local, low cost rock and useable area for the TES.

Future Work

In the present work a technical assessment of a nuclear power plant with storage is presented with the EPR as the key figure of merit. Results show that EPR decreases with DPR and increased durations of charge and discharge. Future work regarding TES with nuclear power will need to evaluate the economic value of using TES in the grid with accurate consideration of findings of the present work, specifically the requirement to modify the power cycle to accommodate TES and the effects of charge and discharge operation on the efficiency of the power cycle and capacity factor. The present work provides estimates of material cost, but additional costs of the storage module including the secondary cycle for configuration III and modifications to the primary cycle of configurations I and II are not provided. Future work must include these costs as well as the costs of the storage container, ancillary equipment for pressure and temperature regulation, heat exchangers, water storage and the cost of any safety measures.

The cost of the TES is design specific. In the present work, conceptual designs were presented and these concepts can serve as a starting point for consideration of approaches to incorporate heat exchange equipment and to size a rock storage bed or combined sensible and latent heat storage module. The present work also identifies temperatures and pressures of charge and discharge, along with target rates. The present

work assumes constant rates of charge and discharge and round-trip efficiency, each over a wide range. Complete design of the TES will require transient analysis of heat and mass transport to estimate the actual round-trip efficiency. Design must also consider structural integrity and safety along with durability.

The economic value of TES on a power grid could be assessed by the internal rate of return (IRR), which quantifies the annualized rate of return for a given investment.

$$\sum_{n=1}^{N} \frac{1}{(1+IRR)^n} = \frac{C}{r - c_{om}} \tag{91}$$

The IRR calculation accounts for the initial capital costs of the system (C) and revenue generated by the system which is the revenue (r) minus the costs of operation and maintenance (c_{om}) over the life (N years) of the investment. For a generic energy storage device, the yearly revenue generated is the revenue from discharge minus the cost of energy purchased to charge the TES. For TES with nuclear power, the revenue must account for the reduction in power of the primary cycle during charging and during baseload operation if the TES is discharged to the primary cycle. The annual revenue is expressed as

$$r = \sum_{t=1}^{8760} \pi(t)\dot{W}_{X,BL}\left[\underbrace{(DPR(t)-1)}_{\substack{Discharge-\\ Added\ Revenue}} - \underbrace{\left(1-\frac{\dot{W}_C(t)}{\dot{W}_{X,BL}}\right)}_{\substack{Charge-\\ Reduced\ Revenue}} \underbrace{-\left(1-\frac{\dot{W}_{BL}(t)}{\dot{W}_{X,BL}}\right)}_{\substack{Baseload-\\ Reduced\ Revenue}}\right] \tag{92}$$

in which the term $\pi(t)$ is the hourly price of electricity over the duration of the year. The current work provides the power during charge ($\dot{W}_C$) as a function of the DPR, t_C, t_D and η_{RT}. The baseload power of the system ($\dot{W}_{BL}$) is expressed as a function of the DPR. Results are summarized in section 4.3.1.

The next generation of nuclear power plants has higher operating temperatures enabled through the use of higher temperature reactor coolants such as liquid sodium and lead [33]. These new reactors present new opportunities for TES, including direct storage of the reactor coolant [20]. Integrating storage within the cooling loop would accommodate a high discharge temperature and pressure, equivalent to the high-pressure turbine inlet temperature and pressure, reducing storage capacity but requiring oversizing the turbines to accommodate higher steam mass flow rates during discharge. The method of analysis described in this work can be applied to these power cycles to assess TES options and the impacts on the operation of the power cycle and compare them to the configurations demonstrated in the present work for TES.

References

[1] U.S. Energy Information Administration (EIA), “Annual Energy Outlook 2018 with Projections to 2050,” 2018. doi: DOE/EIA-0383(2017).

[2] P. Denholm, R. Margolis, and J. Milford, “Production cost modeling for high levels of photovoltaics penetration (NREL/TP-581-42305),” 2009.

[3] National Renewable Energy Laboratory (NREL), “Exploration of High-Penetration Renewable Electricity Futures,” Golden, CO. doi: NREL/TP-6A20-52409-1.

[4] M. M. Hand *et al.*, “Renewable Electricity Futures Study: End-use Electricity Demand,” *Nrel Tp-6a20-52409*, vol. 3, 2012, doi: NREL/TP-6A20-52409-1.

[5] Xcel Energy, “Xcel Energy Low Carbon Scenario Analysis Decarbonizing the Generation Portfolio of Xcel Energy’s Upper Midwest System (Available: https://www.xcelenergy.com/staticfiles/xe-responsive/Company/Rates%20&%20Regulations/Resource%20Plans/Upper-Midwest-Energy-Pl,” 2020.

[6] S. Pacala and R. Socolow, “Stabilization Wedges : Solving the Climate Problem for the Next 50 Years with Current Technologies,” *Science (80-.).*, vol. 305, no. 5686, pp. 968–972, 2016.

[7] J. D. Jenkins and S. Thernstrom, “Deep Decarbonization of the Electric Power Sector (available: https://www.innovationreform.org/wp-content/uploads/2018/02/EIRP-Deep-Decarb-Lit-Review-Jenkins-Thernstrom-March-2017.pdf.),” no. March, 2017.

[8] J. D. Jenkins *et al.*, “The benefits of nuclear flexibility in power system operations with renewable energy,” *Appl. Energy*, vol. 222, no. October 2017, pp. 872–884, 2018, doi: 10.1016/j.apenergy.2018.03.002.

[9] T. T. Mai *et al.*, “Electrification Futures Study: Scenarios of Electric Technology Adoption and Power Consumption for the United States,” *Nrel/Tp-6a20-71500*, 2018, doi: 10.2172/1459351.

[10] J. Eyer and G. Corey, “Energy Storage for the Electricity Grid: Benefits and Market Potential Assessment Guide A Study for the DOE Energy Storage Systems Program,” Albuquerque, 2010. Accessed: Jun. 22, 2017. [Online]. Available: https://www.smartgrid.gov/files/energy_storage.pdf.

[11] X. Luo, J. Wang, M. Dooner, and J. Clarke, “Overview of current development in electrical energy storage technologies and the application potential in power system operation,” *Appl. Energy*, vol. 137, pp. 511–536, 2015, doi: 10.1016/j.apenergy.2014.09.081.

[12] H. Chen, T. N. Cong, W. Yang, C. Tan, Y. Li, and Y. Ding, “Progress in electrical energy storage system: A critical review,” *Prog. Nat. Sci.*, vol. 19, no. 3, pp. 291–312, 2009, doi: 10.1016/j.pnsc.2008.07.014.

[13] T. M. Gür, “Review of electrical energy storage technologies, materials and systems: challenges and prospects for large-scale grid storage,” *Energy Environ. Sci.*, vol. 11, no. 10, pp. 2696–2767, 2018, doi: 10.1039/C8EE01419A.

[14] National Renewable Energy Laboratory NREL, “Renewable Electricity Generation and Storage Technologies,” *Renew. Electr. Futur. Study Renew. Electr. Gener. Storage Technol. Vol. 2*, vol. 2, 2012, doi: NREL/TP-6A20-52409-2.

[15] C. J. Yang and R. B. Jackson, “Opportunities and barriers to pumped-hydro energy storage in the United States,” *Renew. Sustain. Energy Rev.*, vol. 15, no. 1, pp. 839–844, 2011, doi: 10.1016/j.rser.2010.09.020.
[16] B. Zakeri and S. Syri, “Electrical energy storage systems : A comparative life cycle cost analysis,” *Renew. Sustain. Energy Rev.*, vol. 42, pp. 569–596, 2015, doi: 10.1016/j.rser.2014.10.011.
[17] C. W. Forsberg, D. C. Stack, D. Curtis, and N. A. Sepulveda, “Converting excess low-price electricity into high-temperature stored heat for industry and high-value electricity production,” vol. 30, no. August, pp. 42–52, 2017, doi: 10.1016/j.tej.2017.06.009.
[18] C. W. Forsberg, “Heat in a Bottle,” *Mech. Eng.*, vol. 141, no. 01, pp. 36–41, Jan. 2019, doi: 10.1115/1.2019-JAN-2.
[19] C. W. Forsberg, “Variable and Assured Peak Electricity Production from Base-Load Light-Water Reactors with Heat Storage and Auxiliary Combustible Fuels,” *Nucl. Technol.*, vol. 205, no. 3, pp. 377–396, Mar. 2019, doi: 10.1080/00295450.2018.1518555.
[20] P. Denholm, J. C. King, C. F. Kutcher, and P. P. H. Wilson, “Decarbonizing the electric sector: Combining renewable and nuclear energy using thermal storage,” *Energy Policy*, vol. 44, pp. 301–311, 2012, doi: 10.1016/j.enpol.2012.01.055.
[21] R. Socolow, “Climate change and Destiny Studies: Creating our near and far futures,” *Bull. At. Sci.*, vol. 71, no. 6, pp. 18–28, 2015, doi: 10.1177/0096340215611080.
[22] R. Rosner and A. Hearn, “What role could nuclear power play in limiting climate change?,” *Bull. At. Sci.*, vol. 73, no. 1, pp. 2–6, 2017, doi: 10.1080/00963402.2016.1264203.
[23] C. W. Forsberg, “Nuclear + Renewables in a Deeply Decarbonized Grid (Available: http://energytransition.umn.edu/category/events/).” Minneapolis, 2018, [Online]. Available: http://energytransition.umn.edu/category/events/.
[24] C. Forsberg, “Thermal Energy Storage Systems for Peak Electricity from Nuclear Energy,” *ARPA-E Work. Therm. Energy Storage*, no. 617, 2011.
[25] C. Forsberg, S. Brick, and G. Haratyk, “Coupling heat storage to nuclear reactors for variable electricity output with baseload reactor operation,” *Electr. J.*, vol. 31, no. 3, pp. 23–31, 2018, doi: 10.1016/j.tej.2018.03.008.
[26] C. Forsberg, “Light Water Reactor Heat Storage for Peak Power and Increased Revenue (MIT-ANP-TR-170),” Cambridge, 2017. [Online]. Available: http://energy.mit.edu/wp-content/uploads/2017/12/Light-Water-Reactor-Heat-Storage-for-Peak-Power-and-Increased-Revenue.pdf.
[27] K. Van Den Bergh and E. Delarue, “Cycling of conventional power plants: Technical limits and actual costs,” *Energy Convers. Manag.*, vol. 97, pp. 70–77, 2015, doi: 10.1016/j.enconman.2015.03.026.
[28] M. A. Gonzalez-Salazar, T. Kirsten, and L. Prchlik, “Review of the operational flexibility and emissions of gas- and coal-fired power plants in a future with growing renewables,” *Renew. Sustain. Energy Rev.*, vol. 82, no. July 2017, pp. 1497–1513, 2018, doi: 10.1016/j.rser.2017.05.278.
[29] A. F. Wibisono and E. Shwageraus, “Thermodynamic performance of Pressurized Water Reactor power conversion cycle combined with fossil-fuel superheater,”

Energy, vol. 117, pp. 190–197, 2016, doi: 10.1016/j.energy.2016.10.060.
[30] A. Dragunov, E. Saltanov, I. Pioro, P. Kirillov, and R. Duffey, "Power cycles of generation III and III+ Nuclear Power Plants," *Int. Conf. Nucl. Eng. Proceedings, ICONE*, vol. 5, no. April 2015, pp. 1–10, 2014, doi: 10.1115/ICONE22-30151.
[31] T. Abram and S. Ion, "Generation-IV nuclear power: A review of the state of the science," *Energy Policy*, vol. 36, no. 12, pp. 4323–4330, 2008, doi: 10.1016/j.enpol.2008.09.059.
[32] C. W. Forsberg, "Market Basis for Salt-Cooled Reactors: Dispatchable Heat, Hydrogen, and Electricity with Assured Peak Power Capacity," *Nucl. Technol.*, vol. 206, no. 11, pp. 1659–1685, Nov. 2020, doi: 10.1080/00295450.2020.1743628.
[33] C. Forsberg, "The advanced high-temperature reactor: High-temperature fuel, liquid salt coolant, liquid-metal-reactor plant," *Prog. Nucl. Energy*, vol. 47, no. 1–4, pp. 32–43, Jan. 2005, doi: 10.1016/j.pnucene.2005.05.002.
[34] A. Kitada, "Public opinion changes after the Fukushima Daiichi Nuclear Power Plant accident to nuclear power generation as seen in continuous polls over the past 30 years," *J. Nucl. Sci. Technol.*, vol. 53, no. 11, pp. 1686–1700, 2016, doi: 10.1080/00223131.2016.1175391.
[35] M. V. V. Ramana, "Nuclear power and the public," *Bull. At. Sci.*, vol. 67, no. 4, pp. 43–51, Jul. 2011, doi: 10.1177/0096340211413358.
[36] G. Haratyk, "Early nuclear retirements in deregulated U.S. markets: Causes, implications and policy options," *Energy Policy*, vol. 110, no. July, pp. 150–166, Nov. 2017, doi: 10.1016/j.enpol.2017.08.023.
[37] P. V. Gilli and G. Beckman, "Steam storage adds peaking capacity to nuclear plants," *Energy Int.*, vol. 10, no. 8, pp. 16–18, 1973.
[38] P. V. Gilli and K. Fritz, "Nuclear power plants with integrated steam accumulators for load peaking," in *IAEA Symposium on Economic Integration of Nuclear Power Stations in Electrical Power Systems*, 1970, p. WB-KE-2015.
[39] C. Forsberg, "Hybrid systems to address seasonal mismatches between electricity production and demand in nuclear renewable electrical grids," *Energy Policy*, vol. 62, pp. 333–341, 2013, doi: 10.1016/j.enpol.2013.07.057.
[40] IPCC, "Summary for Policymakers," 2019. doi: 10.1017/CBO9781107415324.004.
[41] D. Curtis, N. Shifflet, and C. Forsberg, "Technology Options for Integrated Thermal Energy Storage in Nuclear Power Plants," *Trans. Am. Nucl. Soc.*, vol. 116, pp. 837–840, 2017, [Online]. Available: http://ansannual.org/wp-content/data/polopoly_fs/1.3584124.1494346909!/fileserver/file/768186/filename/270.pdf.
[42] K. Bradbury, L. Pratson, and D. Patiño-Echeverri, "Economic viability of energy storage systems based on price arbitrage potential in real-time U.S. electricity markets," *Appl. Energy*, vol. 114, pp. 512–519, 2014, doi: 10.1016/j.apenergy.2013.10.010.
[43] D. McConnell, T. Forcey, and M. Sandiford, "Estimating the value of electricity storage in an energy-only wholesale market," *Appl. Energy*, vol. 159, pp. 422–432, 2015, doi: 10.1016/j.apenergy.2015.09.006.
[44] R. Sioshansi, P. Denholm, T. Jenkin, and J. Weiss, "Estimating the value of

electricity storage in PJM: Arbitrage and some welfare effects," *Energy Econ.*, vol. 31, no. 2, pp. 269–277, 2009, doi: 10.1016/j.eneco.2008.10.005.
[45] A. Kluba and R. Field, "Optimization and Exergy Analysis of Nuclear Heat Storage and Recovery," *Energies*, vol. 12, no. 21, p. 4205, Nov. 2019, doi: 10.3390/en12214205.
[46] F. Carlson, J. H. Davidson, N. Tran, and A. Stein, "Model of the impact of use of thermal energy storage on operation of a nuclear power plant Rankine cycle," *Energy Convers. Manag.*, vol. 181, no. September 2018, pp. 36–47, Feb. 2019, doi: 10.1016/j.enconman.2018.11.058.
[47] N. Tran, W. Zhao, F. Carlson, J. H. Davidson, and A. Stein, "Metal Nanoparticle–Carbon Matrix Composites with Tunable Melting Temperature as Phase-Change Materials for Thermal Energy Storage," *ACS Appl. Nano Mater.*, vol. 1, no. 4, pp. 1894–1903, Apr. 2018, doi: 10.1021/acsanm.8b00290.
[48] F. Carlson and J. H. Davidson, "On the Use of Thermal Energy Storage for Flexible Baseload Power Plants: Thermodynamic Analysis of Options for a Nuclear Rankine Cycle," *J. Heat Transfer*, vol. 142, no. 5, May 2020, doi: 10.1115/1.4045230.
[49] California ISO, "CAISO's TOU period analysis to address 'High Renewable' grid needs," 2015. Accessed: Jul. 25, 2019. [Online]. Available: https://www.caiso.com/Documents/CaliforniaISO_Time_UsePeriodAnalysis.pdf.
[50] P. Denholm and M. Hand, "Grid flexibility and storage required to achieve very high penetration of variable renewable electricity," *Energy Policy*, vol. 39, no. 3, pp. 1817–1830, Mar. 2011, doi: 10.1016/j.enpol.2011.01.019.
[51] Cailfornia Independent System Operator, "Operating Procedure - Ancillary Service Procurement and Availability Validation," 2018. [Online]. Available: http://www.caiso.com/Documents/1340.pdf.
[52] S. Sharma, S. H. Huang, and N. D. R. Sarma, "System inertial frequency response estimation and impact of renewable resources in ERCOT interconnection," *IEEE Power Energy Soc. Gen. Meet.*, vol. 1, pp. 1–6, 2011, doi: 10.1109/PES.2011.6038993.
[53] P. Denholm and R. M. Margolis, "Evaluating the limits of solar photovoltaics (PV) in electric power systems utilizing energy storage and other enabling technologies," *Energy Policy*, vol. 35, no. 9, pp. 4424–4433, 2007, doi: 10.1016/j.enpol.2007.03.004.
[54] T. Traber and C. Kemfert, "Gone with the wind? - Electricity market prices and incentives to invest in thermal power plants under increasing wind energy supply," *Energy Econ.*, vol. 33, no. 2, pp. 249–256, 2011, doi: 10.1016/j.eneco.2010.07.002.
[55] EPRI, "Electric Energy Storage Technology Options: A White Paper Primer on Applications, Costs and Benefits," *Epri*, pp. 1–170, 2010, doi: EPRI 1020676.
[56] G. Beckman and P. V. Gilli, *Thermal Energy Storage*, 1st ed. Wien: Springer-Verlag, 1984.
[57] W. Hausz, B. J. Berkowitz, and R. C. Hare, "Conceptual Design of Thermal Energy Storage Systems for Near Term Electric Utility Applications Volume Two : Appendices-Screening of Concepts," Santa Barbara, 1978. [Online]. Available: https://ntrs.nasa.gov/archive/nasa/casi.ntrs.nasa.gov/19790005325.pdf.

[58] General Electric Power, “Steam Turbine Advanced Steam Path Upgrade,” 2017. https://www.ge.com/power/services/steam-turbines/upgrades/advanced-steam-path (accessed Jun. 12, 2018).
[59] Ontario Society of Professional Engineers, “Wind and the Electrical Grid: Mitigating the Rise in Electricity Rates and Greenhouse Gas Emissions,” p. 44, 2012, [Online]. Available: https://www.ospe.on.ca/public/documents/advocacy/2012-wind-electrical-grid.pdf.
[60] B. Y. C. Funk and B. Kennedy, “The Politics of Climate,” *PEW Res. Cent.*, pp. 1–114, 2016, Accessed: May 04, 2018. [Online]. Available: http://www.pewinternet.org/2016/10/04/the-politics-of-climate/.
[61] Westinghouse, “Westinghouse AP1000 Design Control Document Rev. 19,” 2011. https://www.nrc.gov/docs/ML1117/ML11171A500.html (accessed Jan. 01, 2017).
[62] Westinghouse Electric Company, “AP1000 PWR - Overview.” http://www.westinghousenuclear.com/New-Plants/AP1000-PWR/Overview (accessed May 01, 2017).
[63] M. A. Rosen, “Energy- and exergy-based comparison of coal-fired and nuclear steam power plants,” *Exergy, An Int. J.*, vol. 1, no. 3, pp. 180–192, 2001, doi: 10.1016/S1164-0235(01)00024-3.
[64] R. L. Bartlett, “Estimating Techniques,” in *Steam turbine performance and economics*, 1st ed., New York: McGraw-Hill Book Company, 1958, pp. 160–196.
[65] D. Laing, W.-D. Steinmann, M. Fiß, R. Tamme, T. Brand, and C. Bahl, “Solid Media Thermal Storage Development and Analysis of Modular Storage Operation Concepts for Parabolic Trough Power Plants,” *J. Sol. Energy Eng.*, vol. 130, no. 1, p. 011006, 2008, doi: 10.1115/1.2804625.
[66] U. Herrmann and D. W. Kearney, “Survey of Thermal Energy Storage for Parabolic Trough Power Plants,” *J. Sol. Energy Eng.*, vol. 124, no. 2, p. 145, 2002, doi: 10.1115/1.1467601.
[67] Therminol, “Therminol VP-1 Heat Transfer Fluid.” Kingsport, pp. 1–8, 2016, [Online]. Available: https://www.therminol.com/sites/therminol-prd.us-east-1.elasticbeanstalk.com/files/documents/TF09A_Therminol_VP1.pdf.
[68] Y. Takahashi, M. Kamimoto, Y. Abe, R. Sakamoto, K. Kanari, and T. Ozawa, “Investigation of latent heat thermal energy storage materials. V. thermoanalytical evaluation of binary eutectic mixtures and compounds of NAOH with NaNO3OR NaNO2,” *Thermochim. Acta*, vol. 123, no. C, pp. 233–245, 1988, doi: 10.1016/0040-6031(88)80027-3.
[69] Alibaba.com, “NaNO3:NaOH Cost,” 2018. https://www.alibaba.com/trade/search?fsb=y&IndexArea=product_en&CatId=&SearchText=NaNO3%3ANaOH+&viewtype= (accessed May 09, 2018).
[70] L. Kourkova, R. Svoboda, G. Sadovska, V. Podzemna, and A. Kohutova, “Heat capacity of NaNO2,” *Thermochim. Acta*, vol. 491, no. 1–2, pp. 80–83, 2009, doi: 10.1016/j.tca.2009.03.005.
[71] Alibaba.com, “NaNO2 Cost,” 2018. https://www.alibaba.com/trade/search?fsb=y&IndexArea=product_en&CatId=&SearchText=NaNO2&viewtype= (accessed Sep. 05, 2018).
[72] M. M. Kenisarin, “High-temperature phase change materials for thermal energy storage,” *Renew. Sustain. Energy Rev.*, vol. 14, no. 3, pp. 955–970, 2010, doi:

10.1016/j.rser.2009.11.011.
[73] Alibaba.com, “LiCl:LiOH Cost,” 2018. https://www.alibaba.com/trade/search?fsb=y&IndexArea=product_en&CatId=&SearchText=NaNO3&viewtype= (accessed May 09, 2018).
[74] H. Ge, H. Li, S. Mei, and J. Liu, “Low melting point liquid metal as a new class of phase change material: An emerging frontier in energy area,” *Renew. Sustain. Energy Rev.*, vol. 21, pp. 331–346, 2013, doi: 10.1016/j.rser.2013.01.008.
[75] Alibaba.com, “Bismuth Cost,” 2018. https://www.alibaba.com/trade/search?fsb=y&IndexArea=product_en&CatId=&SearchText=bismuth (accessed May 09, 2018).
[76] R. Tamme, T. Bauer, J. Buschle, D. Laing, H. Müller-Steinhagen, and W.-D. Steinmann, “Latent heat storage above 120°C for applications in the industrial process heat sector and solar power generation,” *Int. J. Energy Res.*, vol. 32, no. 3, pp. 264–271, Mar. 2008, doi: 10.1002/er.1346.
[77] M. Liu, Y. Ma, H. Wu, and R. Y. Wang, “Metal matrix-metal nanoparticle composites with tunable melting temperature and high thermal conductivity for phase-change thermal storage,” *ACS Nano*, vol. 9, no. 2, pp. 1341–1351, 2015, doi: 10.1021/nn505328j.
[78] M. Liu and R. Y. Wang, “Phase change nanocomposites with tunable melting temperature and thermal energy storage density,” *Nanoscale*, vol. 5, no. 16, pp. 7234–7237, 2013, doi: 10.1039/c3nr02842a.
[79] L. C. Stodola, A. and Loewenstein, “The Many Stage Reaction Turbine,” in *Steam and Gas Turbines*, 2nd ed., New York: D. Van Nostrand Company, 1905, pp. 104–118.
[80] S. L. Dixon and C. A. Hall, *Axial-Flow Turbines*. 2014.
[81] M. Medrano, A. Gil, I. Martorell, X. Potau, and L. F. Cabeza, “State of the art on high-temperature thermal energy storage for power generation. Part 2-Case studies,” *Renew. Sustain. Energy Rev.*, vol. 14, no. 1, pp. 56–72, 2010, doi: 10.1016/j.rser.2009.07.036.
[82] L. Bird, M. Milligan, and D. Lew, “Integrating Variable Renewable Energy: Challenges and Solutions,” Golden, CO (United States), Sep. 2013. doi: 10.2172/1097911.
[83] M. M. Hand *et al.*, “Renewable Electricity Futures Study (Entire Report) (NREL/TP-6A20-52409),” Golden, CO, 2012. [Online]. Available: http://www.nrel.gov/analysis/re_futures/.
[84] P. Moriarty and D. Honnery, “Can renewable energy power the future?,” *Energy Policy*, vol. 93, pp. 3–7, 2016, doi: 10.1016/j.enpol.2016.02.051.
[85] D. O. Akinyele and R. K. Rayudu, “Review of energy storage technologies for sustainable power networks,” *Sustain. Energy Technol. Assessments*, vol. 8, pp. 74–91, Dec. 2014, doi: 10.1016/j.seta.2014.07.004.
[86] A. Gil *et al.*, “State of the art on high temperature thermal energy storage for power generation. Part 1-Concepts, materials and modellization,” *Renew. Sustain. Energy Rev.*, vol. 14, no. 1, pp. 31–55, 2010, doi: 10.1016/j.rser.2009.07.035.
[87] A. Sharma, V. V. Tyagi, C. R. Chen, and D. Buddhi, “Review on thermal energy storage with phase change materials and applications,” *Renew. Sustain. Energy Rev.*, vol. 13, no. 2, pp. 318–345, 2009, doi: 10.1016/j.rser.2007.10.005.

[88] S. Kuravi, J. Trahan, D. Y. Goswami, M. M. Rahman, and E. K. Stefanakos, “Thermal energy storage technologies and systems for concentrating solar power plants,” *Prog. Energy Combust. Sci.*, vol. 39, no. 4, pp. 285–319, 2013, doi: 10.1016/j.pecs.2013.02.001.
[89] C. W. Forsberg, G. Haratyk, and J. D. Jenkins, *Light Water Reactor Heat Storage for Peak Power and Increased Revenue: Focused Workshop on Near Term Options, MIT-ANP-TR-170*. Cambridge, MA, MA, 2017.
[90] A. Black, F. Aydogan, and C. L. Koerner, “Economic viability of light water small modular nuclear reactors : General methodology and vendor data,” vol. 103, no. January, pp. 248–258, 2019, doi: 10.1016/j.rser.2018.12.041.
[91] D. Laing, C. Bahl, T. Bauer, D. Lehmann, and W. D. Steinmann, “Thermal energy storage for direct steam generation,” *Sol. Energy*, vol. 85, no. 4, pp. 627–633, 2011, doi: 10.1016/j.solener.2010.08.015.
[92] V. Ganapathy, “Heat Recovery Boilers,” in *Industrial Boilers and Heat Recovery Steam Generators*, First., New York: Marcel Dekker, Inc, 2003, pp. 41–88.
[93] T. Yamamoto, T. Furuhata, N. Arai, and K. Mori, “Design and testing of the Organic Rankine Cycle,” *Energy*, vol. 26, no. 3, pp. 239–251, Mar. 2001, doi: 10.1016/S0360-5442(00)00063-3.
[94] National Institute of Standards and Technology, “Water: Antoine Equation Parameters,” *NIST Chemistry WebBook, SRD 69*, 2018. https://webbook.nist.gov/cgi/cbook.cgi?ID=C7732185&Mask=4&Type=ANTOINE&Plot=on#ANTOINE (accessed Apr. 06, 2019).
[95] N. Khartchenko and V. Kharchenko, *Advanced Energy Systems*, 2nd ed. Boca Raton, FL: CRC Press, 2014.
[96] M. Holmgren, “XSteam - IAPWS IF-97.” 2007, [Online]. Available: https://www.mathworks.com/matlabcentral/fileexchange/9817-x-steam-thermodynamic-properties-of-water-and-steam.
[97] R. Sigg, C. Heinz, M. V. Casey, and N. Sürken, “Numerical and experimental investigation of a low-pressure steam turbine during windage,” *Proc. Inst. Mech. Eng. Part A J. Power Energy*, vol. 223, no. 6, pp. 697–708, 2009, doi: 10.1243/09576509JPE826.
[98] M. Richter, G. Oeljeklaus, and K. Görner, “Improving the load flexibility of coal-fired power plants by the integration of a thermal energy storage,” *Appl. Energy*, vol. 236, no. October 2018, pp. 607–621, Feb. 2019, doi: 10.1016/j.apenergy.2018.11.099.
[99] O. Garbrecht, M. Bieber, and R. Kneer, “Increasing fossil power plant flexibility by integrating molten-salt thermal storage,” *Energy*, vol. 118, pp. 876–883, 2017, doi: 10.1016/j.energy.2016.10.108.
[100] General Electric Power, “Gigatop 4-Pole Generator,” 2020. https://www.ge.com/power/gas/generators/water-cooled-gigatop-4-pole (accessed May 02, 2020).
[101] Siemens Energy, “SGen-3000W generator series,” 2020. https://www.siemens-energy.com/global/en/offerings/power-generation/generators/sgen-3000w.html (accessed Oct. 09, 2020).
[102] C. Stansbury, “Westinghouse Heat Storage Investigation (Available: https://energy.mit.edu/wp-content/uploads/2017/12/Light-Water-Reactor-Heat-

Storage-for-Peak-Power-and-Increased-Revenue.pdf).” 2017.
[103] J. E. Pacheco *et al.*, “Final Test and Evaluation Results from the Solar Two Project,” *Sandia Natl. Lab.*, no. January, p. 294, 2002, doi: 10.2172/793226.
[104] D. H. Cooke, “On prediction of off-design multistage turbine pressures by Stodola’s Ellipse,” in *1984 Joint Power Generation Conference: GT Papers*, 1984, pp. 1–12.
[105] H. S. Kirols, D. Kevorkov, A. Uihlein, and M. Medraj, “Water droplet erosion of stainless steel steam turbine blades,” *Mater. Res. Express*, vol. 4, no. 8, p. 086510, Aug. 2017, doi: 10.1088/2053-1591/aa7c70.
[106] J. Lehne and F. Preston, “Making Concrete Change Innovation in Low-carbon Cement and Concrete The Royal Institute of International Affairs, Chatham House Report Series, www.chathamhouse.org/sites/default/files/publications/research/2018-06-13-makingconcrete- c,” London, 2018. [Online]. Available: www.chathamhouse.org.
[107] H. Grirate *et al.*, “Characterization of several Moroccan rocks used as filler material for thermal energy storage in CSP power plants,” *Energy Procedia*, vol. 49, pp. 810–819, 2014, doi: 10.1016/j.egypro.2014.03.088.
[108] S. L. Aly and A. I. El-Sharkawy, “Effect of storage medium on thermal properties of packed beds,” *Heat Recover. Syst. CHP*, vol. 10, no. 5–6, pp. 509–517, 1990, doi: 10.1016/0890-4332(90)90201-T.
[109] K. G. Allen, T. W. Von Backström, and D. G. Kröger, “Packed rock bed thermal storage in power plants: Design considerations,” *Energy Procedia*, vol. 49, no. December, pp. 666–675, 2013, doi: 10.1016/j.egypro.2014.03.072.
[110] M. N. Strasser and R. P. Selvam, “A cost and performance comparison of packed bed and structured thermocline thermal energy storage systems,” *Sol. Energy*, vol. 108, pp. 390–402, 2014, doi: 10.1016/j.solener.2014.07.023.
[111] M. Hänchen, S. Brückner, and A. Steinfeld, “High-temperature thermal storage using a packed bed of rocks - Heat transfer analysis and experimental validation,” *Appl. Therm. Eng.*, vol. 31, no. 10, pp. 1798–1806, 2011, doi: 10.1016/j.applthermaleng.2010.10.034.
[112] M. S. Abdel-Salam, S. L. Aly, A. I. El-Sharkawy, and Z. Abdel-Rehim, “Thermal characteristics of packed bed storage system,” *Int. J. Energy Res.*, vol. 15, no. 1, pp. 19–29, 1991, doi: 10.1002/er.4440150104.
[113] K. Allen, T. Von Backström, E. Joubert, and P. Gauché, “Rock bed thermal storage: Concepts and costs,” *AIP Conf. Proc.*, vol. 1734, no. May 2016, 2016, doi: 10.1063/1.4949101.
[114] R. Raud, R. Jacob, F. Bruno, G. Will, and T. A. Steinberg, “A critical review of eutectic salt property prediction for latent heat energy storage systems,” *Renew. Sustain. Energy Rev.*, vol. 70, no. October 2016, pp. 936–944, 2017, doi: 10.1016/j.rser.2016.11.274.
[115] Alibaba.com, “NaOH Cost,” 2020. https://www.alibaba.com/trade/search?fsb=y&IndexArea=product_en&CatId=&SearchText=NaOH&viewtype=&tab= (accessed Oct. 14, 2020).
[116] Alibaba.com, “KOH Cost,” 2020. https://www.alibaba.com/trade/search?fsb=y&IndexArea=product_en&CatId=&SearchText=KOH (accessed Oct. 14, 2020).

[117] Á. G. Fernández and J. C. Gomez-Vidal, “Thermophysical properties of low cost lithium nitrate salts produced in northern Chile for thermal energy storage,” *Renew. Energy*, vol. 101, no. 3, pp. 120–125, 2017, doi: 10.1016/j.renene.2016.08.052.
[118] P. F. Peterson, H. Zhao, and R. Petroski, “Metal And Concrete Inputs For Several Nuclear Power Plants (UCBTH-05-001),” Berkeley, 2005.